High Performance of Organic Field-Effect Transistors Achieved by Active Layer Formation on Highly Hydrophobic Gate Dielectric Surfaces

Bulgarevich Kirill Dmitrievich

February 2020

High Performance of Organic Field-Effect Transistors Achieved by Active Layer Formation on Highly Hydrophobic Gate Dielectric Surfaces

Bulgarevich Kirill Dmitrievich
Doctoral Program in Engineering

Submitted to the Graduate School of
Pure and Applied Sciences
in Partial Fulfillment of the Requirements
for the degree of Doctor of Philosophy in
Engineering

at the
University of Tsukuba

Chapter 1   Introduction

Organic materials in the electronics industry are mostly used as insulator materials for power and communication cables. However, after the discovery of the conductive polymers[1.1] which led to the Nobel Prize in Chemistry in 2000, the research attention for the electrical properties of organic materials is increasing. This quickly led to the discoveries of organic semiconductor (OSC) materials, and to inventions of organic field-effect transistors (OFETs),[1.2] organic light-emitting diodes,[1.3] and organic photovoltaics[1.4] in the late 1980s. Until now, many conducting and semiconducting organic materials have been discovered, which recently led to commercial applications such as flexible organic electrophoretic displays and smart cards.[1.5] The unique mechanical properties of organic materials allow the fabrication of such flexible electronics. The organic electronic devices are still slower and less durable to functioning in air than Si-based ones, but many organic materials allow solution process fabrication which can be applied to large-areas at much lower cost (less material usage, less needed energy).

The goal of the organic electronic devices is not to reach the level of performance of the inorganic devices, but to rather use the advantages of the organic materials. For instance, certain parts of the electronic devices that do not require high speed integrated circuits can potentially be fabricated at lower cost through large area and low temperature fabrication. Also, new functionality can be added to the devices such as reduced weight, flexibility, and/or transparency. During the last few decades, the carrier mobility of the OFETs has been improved dramatically, reaching and exceeding the level of amorphous silicon.[1.6],[1.7] Although this is already enough for applications in displays and sensors, the improvement of mobility is still very important to expand the applications of OFETs because the low carrier mobility causes higher power consumption. Also, small device-to-device variation (DDV) of fabricated OFETs is needed for electronic circuits and operational stability of those OFETs has to be high.

Both small molecule and polymer-based OFETs are under active investigation for their potential applications in flexible displays, smart cards,[1.5] radio-frequency identification tags[1.8], and sensors.[1.9],[1.11] The working principles of OFETs, typical OSC materials and fabrication processes are explained in **Chapter 2**. Although small molecule OSCs typically show higher crystallinity and carrier mobility as opposed to polymer-based ones, the lower crystallinity is not always a disadvantage. This is because crystalline domains much smaller than typical length scale compared to dimensions of the OFETs results in higher uniformity of the OSC film and in lower DDV which is of great importance as mentioned above. Also, polymeric semiconductors are generally more durable against mechanical stresses and are more suitable for applications in flexible and stretchable electronics. The improvement of the charge carrier mobility has been achieved through design and synthesis of novel OSC materials[1.12] and by the development of the alignment methods for the π-conjugated molecular plane and the polymer backbone structures.[1.13],[1.14] The operational stability of OFETs is related to the properties of the OSC materials because the number of the trap states depends on the crystallinity.[1.15] Another important factor that affects the device properties is the insulator/OSC interface. The insulator surface is preferred to be as hydrophobic as possible because operational stability is also related to the residual water[1.16],[1.17] and because the edge-on orientation of the OSC molecules is induced by the hydrophobic surface.[1.18] The edge-on orientation is optimal for charge transport in planar OFETs since π-π stacking direction in such orientation is aligned parallel to the surface plane (current flow direction). However, there is a trade-off relationship between the hydrophobicity of the surface and the ease of coating due to the increase in dewetting of the common organic solvents with surface hydrophobicity.

In this thesis, the breakthrough for this problem is reported. By surrounding the hydrophobic areas with hydrophilic ones under appropriate design, the continuous OSC film formation was enabled on the entire substrate surface. The mechanism of film formation was understood by performing a simple surface energy

calculation (**Chapter 3**). The hydrophobic areas, which are important for achieving high device performance, were used as areas for OFET fabrication. As the result, the relatively high carrier mobility was achieved with very small DDV for the terrace-phase poly(2,5-bis(3-hexadecylthiophen-2-yl)thieno[3,2-b]thiophene) (pBTTT-C16) active layer by simple methods based on flow- and spin-coating (**Chapter 4**).[1.19] The carrier mobility was further enhanced by a factor of ~2 through molecular alignment of the pBTTT-C16 backbone structures, which was achieved by the introduction of the highly hydrophobic nano-grooves on the insulator (silicon oxide) surface (**Chapter 5**).[1.20] Also, the high operational stability comparable to amorphous silicon (*a*-Si) FETs was achieved due to high crystallinity of the pBTTT-C16 obtained by using its liquid crystalline (LC) nature and because of the high hydrophobicity of our octadecyltrichlorosilane (ODTS)-treated nano-grooved surfaces (**Chapter 6**). The operational stability of pBTTT-C16 OFETs was further improved by a factor of >1000 by the use of the perfluoropolymer coating layers, resulting in unprecedented operational stability of OFETs (**Chapter 7**).[1.21] These techniques enable the fabrication of high performance OFETs and are expected to aid the implementation of the OSC devices to the society.

References

[1.1]   H. Shirakawa, E. J. Louis, A. G. MacDiarmid, C. K. Chiang, and A. J. Heeger. "Synthesis of Electrically Conducting Organic Polymers: Halogen Derivatives of Polyacetylene, $(CH)_x$." *J. Chem. Soc. Chem. Commun.* **1977** 16, 578.

[1.2]   A. Tsumura, H. Koezuka, and T. Ando. "Macromolecular Electronic Device: Field-Effect Transistor with a Polythiophene Thin Film." *Appl. Phys. Lett.* **1986**, 49, 1210.

[1.3]   C. W. Tang and S. A. Vanslyke. "Organic Electroluminescent Diodes." *Appl. Phys. Lett.* **1987**, 51, 913.

[1.4]   C. W. Tang. "Two-Layer Organic Photovoltaic Cell." *Appl. Phys. Lett.* **1986**, 48, 183.

[1.5]   Available from Plastic Logic Ltd.

[1.6]   C. Dimitrakopoulos and P. R. L. Malenfant. "Organic Thin Film Transistors for Large Area Electronics." *Adv. Mater.* **2002**, 14, 99.

[1.7]   Ö. Abanoz and C. Dimitrakopoulos. "Recent Advances in Organic Field Effect Transistors." *Turk. J. Phys.* **2014**, 38. 497.

[1.8]   M. Uno, Y. Kanaoka, B.-S. Cha, N. Isahaya, M. Sakai, H. Matsui, C. Mitsui, T. Okamoto, J. Takeya, T. Kato, M. Katayama, Y. Usami, and T. Yamakami. "Short-Channel Solution-Processed Organic Semiconductor Transistors and their Application in High-Speed Organic Complementary Circuits and Organic Rectifiers." *Adv. Electron. Mater.* **2015**, 1, 1500178.

[1.9]   X. Wu, Y. Ma, G. Zhang, Y. Chu, J. Du, Y. Zhang, Z. Li, Y. Duan, Z. Fan, and J. Huang. "Thermally Stable, Biocompatible, and Flexible Organic Field-Effect Transistors and Their Application in Temperature Sensing Arrays for Artificial Skin." *Adv. Funct. Mater.* **2015**, 25, 2138.

[1.10] S. Wang, J. Xu, W. Wang, G.-J. N. Wang, R. Rastak, F. Molina-Lopez, J. W. Chung, S. Niu, V. R. Feig, J. Lopez, T. Lei, S.-K. Kwon, Y. Kim, A. M. Foudeh, A. Ehrlich, A. Gasperini, Y. Yun, B. Murmann, J. B.-H. Tok, and Z. Bao. "Skin Electronics from Scalable Fabrication of an Intrinsically Stretchable Transistor Array." *Nature* **2018**, 555, 83.

[1.11] N. Wang, A. Yang, Y. Fu, Y. Li, and F. Yan. "Functionalized Organic Thin Film Transistors for Biosensing." *Acc. Chem. Res.* **2019**, 52, 277.

[1.12] A. Facchetti. "π-Conjugated Polymers for Organic Electronics and Photovoltaic Cell Applications." *Chem. Mater.* **2011**, 23, 733.

[1.13] Y. Diao, L. Shaw, Z. Bao, and S. C. B. Mannsfeld. "Morphology Control Strategies for Solution-Processed Organic Semiconductor Thin Films." *Energy Environ. Sci.* **2014**, 7, 2145.

[1.14] M. Pandey, N. Kumari, S. Nagamatsu, and S. S. Pandey. "Recent Advances in The Orientation of Conjugated Polymers for Organic Field-Effect Transistors." *J. Mater. Chem. C* **2019**, 7, 13323.

[1.15] D. H. Kim, B.-L. Lee, H. Moon, H. M. Kang, E. J. Jeong, J.-I. Park, K.-M. Han, S. Lee, B. W. Yoo, N. W. Koo, J. Y. Kim, W. H. Lee, K. Cho, H. A. Becerril, and Z. Bao. "Liquid-Crystalline Semiconducting Copolymers with Intramolecular Donor-Acceptor Building Blocks for High-Stability Polymer Transistors." *J. Am. Chem. Soc.* **2009**, 131, 6124.

[1.16] S. G. J. Mathijssen, M. Cölle, H. Gomes, E. C. P. Smits, B. de Boer, I. McCulloch, P. A. Bobbert, and D. M. de Leeuw. "Dynamics of Threshold Voltage Shifts in Organic and Amorphous Silicon Field-Effect Transistor." *Adv. Mater.* **2007**, 19, 2785.

[1.17] A. Sharma, S. G. J. Mathijssen, E. C. P. Smits, M. Kemerink, D. M. de Leeuw, and P. A. Bobbert. "Proton Migration Mechanism for Operational Instabilities in Organic Field-Effect Transistors." *Phys. Rev. B* **2010**, 82, 075322.

[1.18] S. Obata and Y. Shimoi. "Control of Molecular Orientations of poly(3-hexylthiophene) on Self-Assembled Monolayers: Molecular Dynamics Simulations." *Phys. Chem. Chem. Phys.* **2013**, 15, 9265.

[1.19] K. Bulgarevich, K. Sakamoto, T. Minari, T. Yasuda, and K. Miki. "Spatially Uniform Thin-Film Formation of Polymeric Organic Semiconductors on Lyophobic Gate Insulator Surfaces by Self-Assisted Flow-Coating." *ACS Appl. Mater. Interfaces* **2017**, 9, 6237.

[1.20] K. Bulgarevich, K. Sakamoto, T. Minari, T. Yasuda, K. Miki, and M. Takeuchi. "Polymer-Based

Organic Field-Effect Transistors with Active Layers Aligned by Highly Hydrophobic Nanogrooved Surfaces." *Adv. Funct. Mater.* **2019**, 29, 1905365.

[1.21] K. Bulgarevich, K. Sakamoto, T. Yasuda, T. Minari, and M. Takeuchi. "Operational Stability Enhancement of Polymeric Organic Field-Effect Transistors by Amorphous Perfluoropolymers Chemically Anchored to Gate Dielectric Surfaces." Submitted to *Adv. Electron. Mater.*

Chapter 2　Organic Field-Effect Transistors (OFETs)

This chapter summarizes the basics about organic field-effect transistors: their structure and working principles, examples of active layer materials and their properties, methods for active layer formation, and importance and methods of controlling the properties of the gate dielectric / active layer interface.

2.1　OFET working principles

The main constituting elements of an OFET are: three electrodes (source, drain, and gate), an active layer of semiconducting material, and a gate insulator. The relative positioning of these components determines the device structure of OFETs. If the gate insulator and source/drain (S/D) electrodes are located on the substrate side relative to the active layer, the device structure is called 'bottom-gate (BG)', and the opposite positioning is 'top-gate (TG)'. Likewise, if S/D electrodes are located on the side of the substrate relative to the active layer, the structure is 'bottom-contact (BC)'. The opposite positioning of S/D electrodes is called 'top-contact (TC)'. The combination of these makes four device structures (BG/BC, TG/BC, BG/BC, TG/TC) possible, which are shown in **Figure 2.1**.
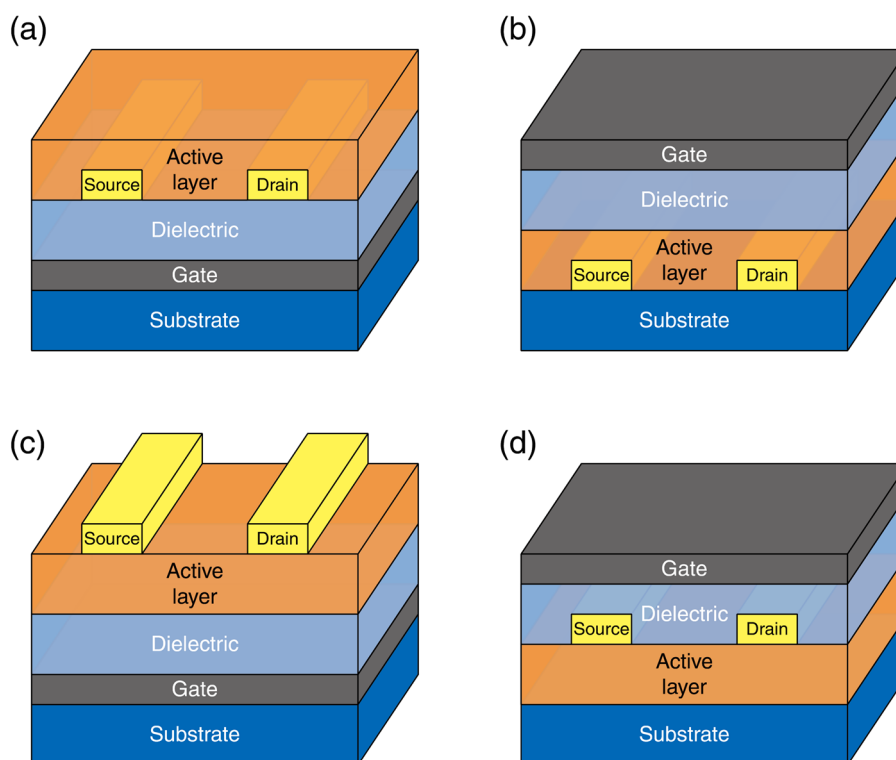
Figure 2.1　(a): Bottom-gate/bottom-contact, (b): top-gate/bottom-contact, (c): bottom-gate/bottom-contact and (d): top-gate/bottom-contact structures of OFETs.

The working principles of OFETs with different device structures are similar. It is understood similar to an inorganic FET. Carriers are inserted into the semiconductor layer of a metal-insulator-semiconductor (MIS) structure from the source electrode and are extracted from the drain electrode. In order to analyze this behavior, gradual channel approximation (GCA) is used.[2.1] This reduces the analysis to one dimensional current flow problem. A cross-sectional view of a BG/BC OFET is illustrated in **Figure 2.2a**. GCA is based on the assumption that the variation of the electric field in the channel in the direction parallel to the source-drain

direction (that along semiconductor-insulator interface) is much smaller than that in the direction perpendicular to the semiconductor insulator interface:

$$\frac{\partial E_x}{\partial x} \ll \frac{\partial E_y}{\partial y}. \tag{2.1}$$

Under this assumption, the charge density ρ is expressed as follows:

$$\frac{\rho}{\epsilon_r \epsilon_0} = \frac{\partial E_x}{\partial x} + \frac{\partial E_y}{\partial y} \approx \frac{\partial E_y}{\partial y}, \tag{2.2}$$

where ϵ_r is the dielectric constant of the insulator layer, and ϵ_0 is vacuum permittivity. Therefore, it is assumed that the channel potential $V(x)$ is a gradually changing function of position and is varying very little over the distance of the order of the insulator thickness. This assumption works well for actual devices as long as the channel length is much longer than the thickness of the gate insulator layer. The following calculation is performed for an OFET that uses a p-type semiconductor. The OFET using n-type semiconductor behaves similarly. Let the electric field that crosses the insulator layer at the position x as $E_y(x)$. If the charge accumulated in the channel at the position x (per unit area) is $Q(x)$, from Gauss's law we get:

$$E_y(x) = \frac{V(x) - V_{GS}}{d} = \frac{Q(x)}{\epsilon_r \epsilon_0}. \tag{2.3}$$

Here, V_{GS} is a voltage applied to the gate and d is the thickness of the insulator layer. $Q(x)$ can be expressed using the capacitance of the gate insulator per unit area ($C_i = \epsilon_r \epsilon_0 / d$):

$$Q(x) = C_i \{V(x) - V_{GS}\}. \tag{2.4}$$

Since the electric field in the source-drain direction $E_x(x)$ is expressed as:

$$E_x(x) = -\frac{dV(x)}{dx}, \tag{2.5}$$

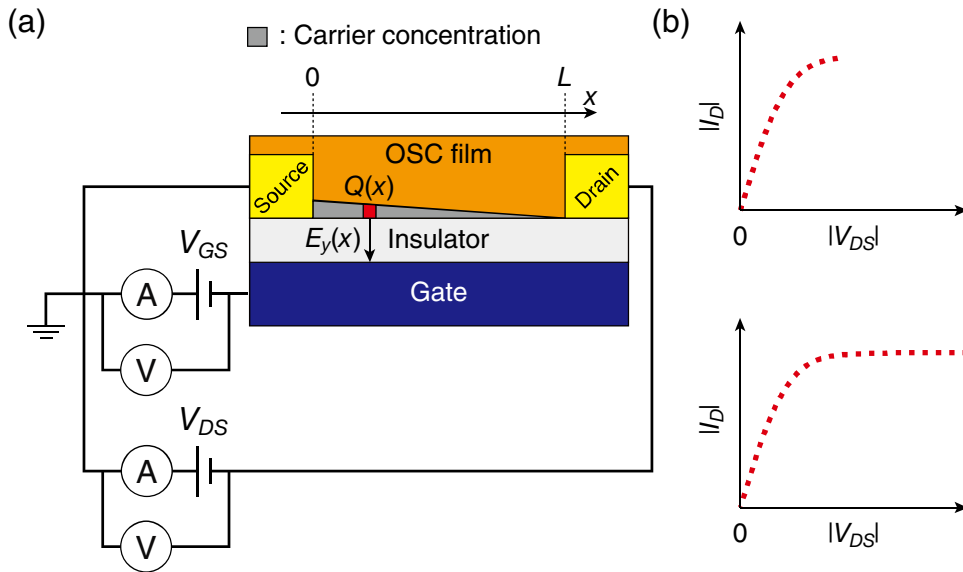Accumulated carriers $Q(x)$ drift and become a drain current I_D:

Figure 2.2 (a): Cross-sectional view of a bottom-gate/top-contact OFET, and (b): I_D as a function of V_{DS} in Equation 2.6.

$$I_D = W\mu Q(x)E_x(x) = -W\mu C_i\{V_{GS} - V(x)\}\frac{dV(x)}{dx}, \tag{2.6}$$

where W is the width of the channel and μ is the carrier mobility. The drain current I_D is independent of the position x. By integrating **Equation 2.6** over the channel length (from $x = 0$ to L), and by using boundary conditions $V(0) = 0$ and $V(L) = V_{DS}$, we obtain:

$$I_D = -\frac{W\mu C_i}{L}V_{DS}\left(V_G - \frac{V_{DS}}{2}\right). \tag{2.7}$$

In actual devices, a minimum threshold voltage (V_{th}) needs to be applied to obtain free carriers. This means that V_{GS} in **Equation 2.7** has to be replaced with $V_{GS} - V_{th}$:

$$I_D = -\frac{W\mu C_i}{L}V_{DS}\left(V_{GS} - V_{th} - \frac{V_{DS}}{2}\right). \tag{2.8}$$

This equation expresses I_D as a quadratic function of V_{DS} (**Figure 2.2**b). I_D increases to the negative side up to the point where $V_{DS} = V_{GS} - V_{th}$. After that, I_D does not decrease even though this is suggested by **Equation 2.8** but becomes saturated (constant). The saturated drain current I_D^{sat} can be expressed as:

$$I_D^{sat}(V_{GS}) = -\frac{W\mu C_i}{2L}(V_{GS} - V_{th})^2. \tag{2.9}$$

The carrier mobility can be extracted from **Equation 2.9** by taking square roots of both sides, and partial derivatives of both sides with respect to V_{GS}:

$$\mu^{sat} = \frac{2L}{WC_i}\left(\frac{\partial\sqrt{-I_D^{sat}}}{\partial V_{GS}}\right)^2, \tag{2.10}$$

which is more commonly written as:

$$\mu^{sat} = \frac{2L}{WC_i}\left(\frac{\partial\sqrt{|I_D^{sat}|}}{\partial V_{GS}}\right)^2. \tag{2.11}$$

This is the equation that is used to calculate the carrier mobility of OFETs in a saturated regime. In the linear regime ($V_{DS} \ll V_{GS}$), **Equation 2.8** becomes:

$$I_D^{lin}(V_{GS}) = -\frac{W\mu C_i}{L}V_{DS}(V_{GS} - V_{th}), \tag{2.12}$$

from which we can obtain the carrier mobility in a linear regime:

$$\mu^{lin} = -\frac{L}{WC_iV_{DS}}\frac{\partial I_D^{lin}}{\partial V_{GS}}, \tag{2.13}$$

2.2 Organic semiconductor (OSC) materials

Organic semiconductor materials contain π electron conjugated aromatic moiety, such as chalcogenophene (thiophene, selenophene) or benzene rings, in their backbone structure. A large variety of such materials were reported. The insoluble materials are suitable only for vapor deposition processes. However, since that is an expensive process, it is often beneficial to use soluble precursor compounds or to add solubilizing substituents such as terminal alkyl groups. Also, the vapor deposition process is not applicable to many organic semiconductor materials (such as organic polymers) and the solubility is required. Here, some examples of the organic semiconductor materials are given.

a) Small molecule organic semiconductors

Low-molecular-weight organic semiconductor materials can have various structures. For example, oligochalcogenophene derivatives, and oligophenylene derivatives. Oligothiophene is one of the most studied oligochalcogenophene semiconductor materials. Its structure is shown in **Figure 2.3**a. This organic semiconductor can be deposited using dry and solution processes and shows carrier mobility of 0.01 ~ 0.1 $cm^2 \cdot V^{-1} \cdot s^{-1}$, depending on the fabrication processes and the length of the alkyl chains.[2.2]-[2.5] DFCO-4T (**Figure 2.3**b) can also be used for both dry and solution-cast processes, showing relatively high mobility of 0.2 $cm^2 \cdot V^{-1} \cdot s^{-1}$.[2.6]
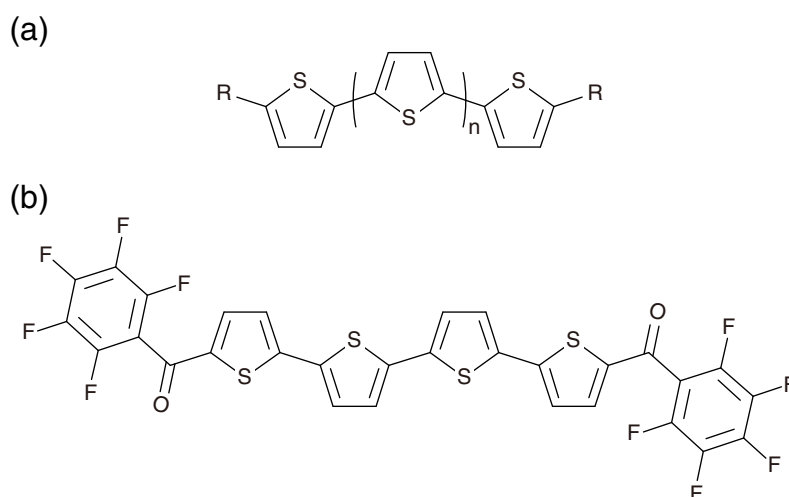

Figure 2.3   Molecular structures of (a): oligothiophene, and (b): DFCO-4T. **R**s in (a) are H or alkyl groups, and **n** can vary from 0 to 6.

Another type of the small molecule organic semiconductors includes polycyclic aromatic moiety in their structure. The π-π overlap for such structure is large and many materials that show very high carrier mobility have been synthesized: for instance, pentacene and its soluble derivative 6,13-bis(triisopropylsilylethynyl) pentacene (TIPS-PEN) shown in **Figure 2.4**a and **Figure 2.4**b, respectively. High carrier mobility of ~5 $cm^2 \cdot V^{-1} \cdot s^{-1}$ was reported for pentacene films, which were formed using vapor evaporation deposition.[2.7],[2.8] For TIPS-PEN, mobility of >1 $cm^2 \cdot V^{-1} \cdot s^{-1}$ was reported by solution processing.[2.9] In order to achieve high carrier mobility, high air stability and high solution processability simultaneously, OSCs with thiophene-thiophene (selenophene-selenophene) in their core such as BTBT and BSBS and their derivatives shown in **Figure 2.4**c were synthesized.[2.10] Very high carrier mobility (~6 $cm^2 \cdot V^{-1} \cdot s^{-1}$) was recently reported for single crystals of 2,7-dioctyl[1]benzothieno[3,2-b][1]benzothiophene (C_8-BTBT) grown on relatively large area by limited solvent vapor-assisted crystallization method.[2.11] The derivatives of C_n-BTBT such as 2,7-Diphenyl[1]benzothieno [3,2-b][1]benzothiophene (DPh-BTBT), 2,7-Diphenyl[1]benzoseleno[3,2-b][1]benzoselenophene (DPh-BSBS), and C_n-BSBS, whose molecular structures are shown in **Figure 2.4**c as well, are also investigated.[2.12],[2.13] Another type of actively investigated OSC of a is dinaphtho-[2,3-b:2',3'-*f*] chalcogenophene[3,2-b]chalcogenophene (DNTT) and its derivatives. The structure of this material is similar to BTBT, but the aromatic rings in the core are all fused. Carrier mobility of C_n-DNTT can reach values of ~7 $cm^2 \cdot V^{-1} \cdot s^{-1}$ for polycrystalline films[2.14] and ~12 $cm^2 \cdot V^{-1} \cdot s^{-1}$ for single crystals.[2.15]
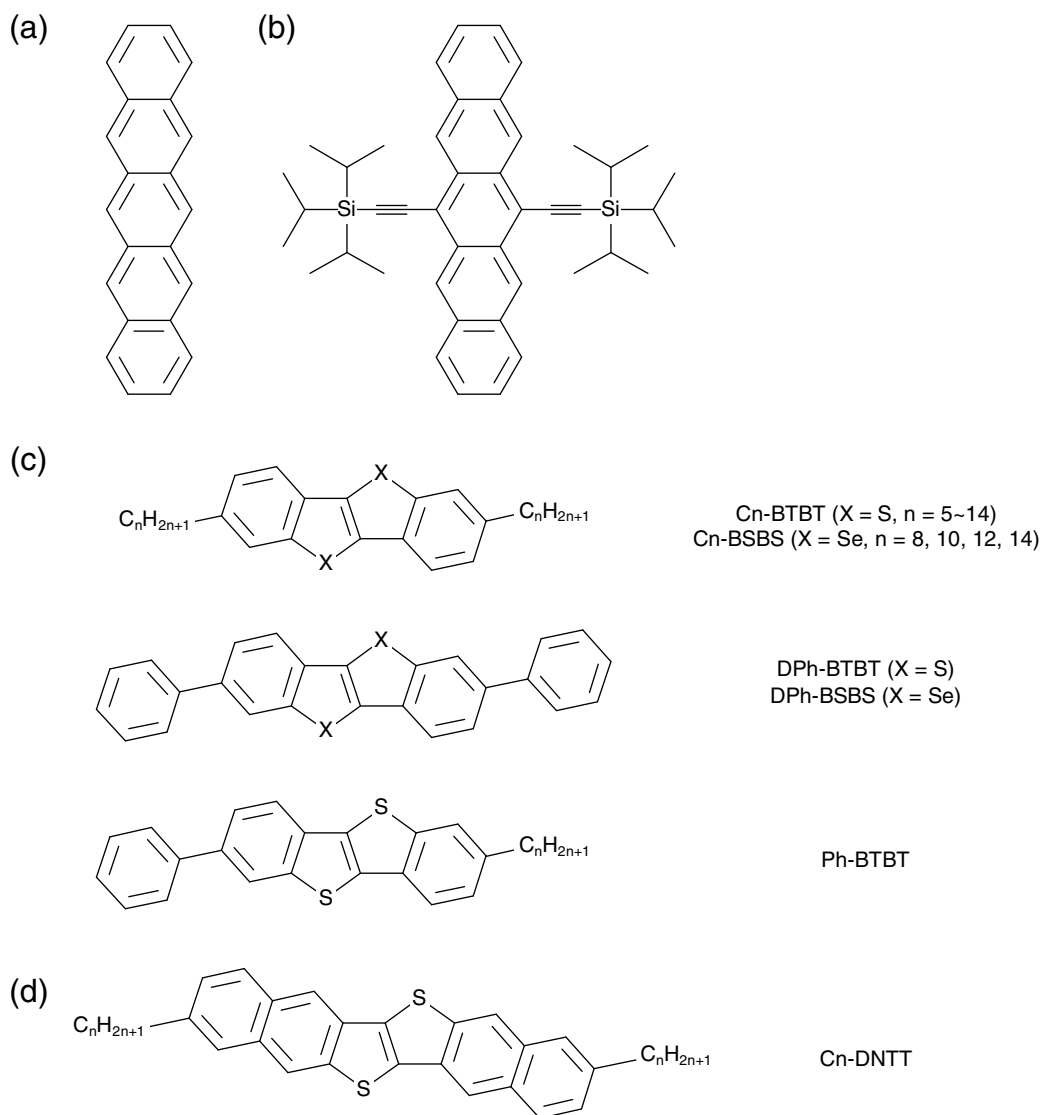
Figure 2.4 Molecular structures of (a): pentacene, (b): TIPS-PEN, (c): C_n-BTBT and its analogues: C_n-BSBS, DPh-BTBT, DPh-BSBS, and Ph-BTBT, and (d): C_n-DNTT.

Finally, there are donor-acceptor (D-A) type OSCs. In this type of OSC, the intermolecular interaction is enhanced through the attractive forces between the donor and acceptor moieties, shortening the π-π stacking distance. For instance, quinoidal benzo[1,2-b:4,5-b']dithiophene (DHB-QDTB) shown in **Figure 2.5**a (donor-acceptor-donor type) shows relatively high mobility of 0.88 cm^2·V^{-1}·s^{-1} under ambient conditions.[2.16] Although the mobility of D-A molecular OSCs still lags behind conventional materials despite expectations and impressive results obtained for D-A copolymer OSCs (see below), high carrier mobility of > 3 cm^2·V^{-1}·s^{-1} was reported recently for LGC-D118 shown in **Figure 2.5**b.[2.17]

(a)

(b)
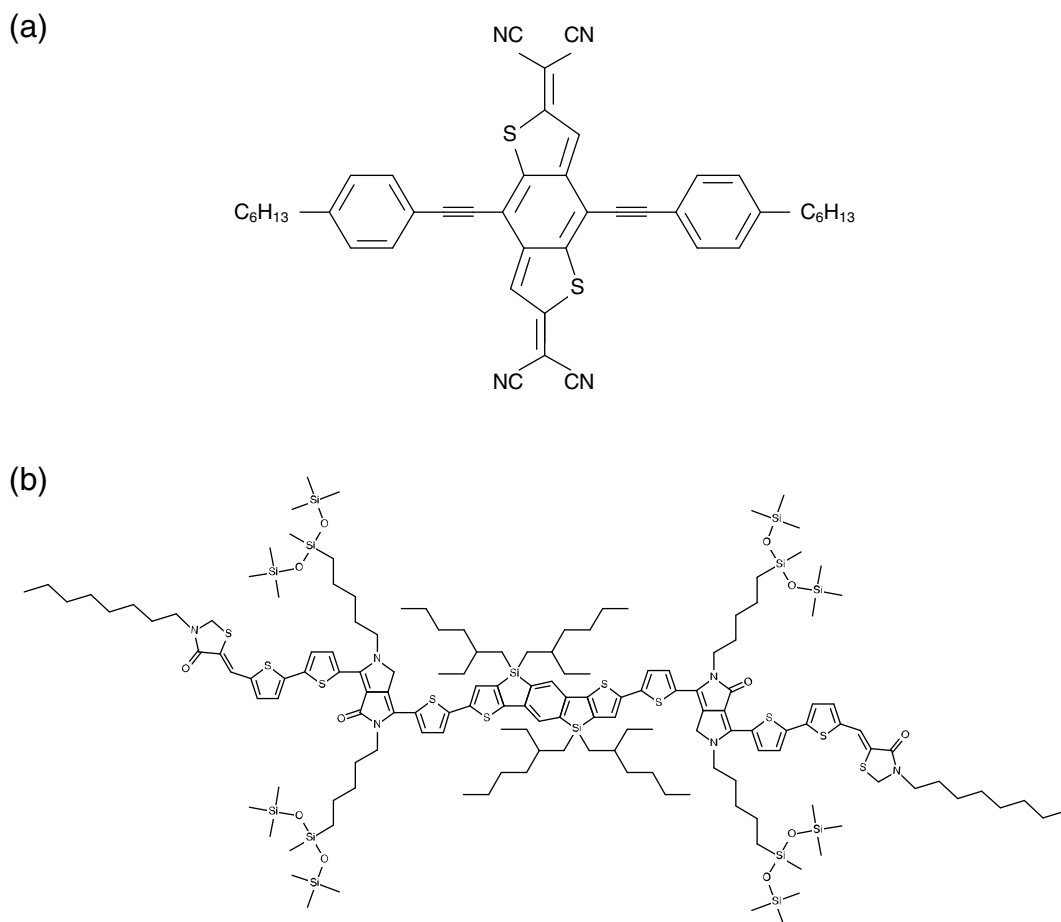
Figure 2.5   Molecular structures of (a): DHB-QDTB and (b): LGC-D118.

b) Polymeric organic semiconductors

Polymer organic semiconductor materials are commonly more thermally stable and mechanically durable than small molecule semiconductors but suffer from lower carrier mobility. However, recently mobility of > 1 $cm^2 \cdot V^{-1} \cdot s^{-1}$ which is approaching that of small molecule semiconductors have been reported for organic polymers. Like for small molecules, polymer OSCs containing oligochalcogenophene, oligophenylene structure, polycyclic aromatic moiety, and D-A type ones are reported.

An example of oligochalcogenophene structured polymers is regioregular poly(3-alkylthiophene) (rrP3AT) which is shown in **Figure 2.6**a. Provided the regioregularity is high, this polymer orients edge-on on the hexamethyldisilazane (HMDS)-treated SiO₂ surface aligning π-stacking direction parallel to the surface plane (source drain direction in OFETs) thus showing high mobility of up to 0.1 $cm^2 \cdot V^{-1} \cdot s^{-1}$.[2.18] The selenophene based rrP3AS (**Figure 2.6**b) was also synthesized, but it shows slightly lower carrier mobility of

(a)   (b)

Figure 2.6   Molecular structures of (a): rrP3AT, and (b): rrP3AS.

10

0.02 ~ 0.04 cm$^2 \cdot$V$^{-1} \cdot$s^{-1} probably due to the weaker intermolecular interaction for Se.[2.19]

Among the polycyclic aromatic structured polymers, one of the most promising materials is poly(2,5-bis(3-alkylthiophen-2-yl)thieno[3,2-b]thiophene) (pBTTT-Cn) shown in **Figure 2.7**a. It has served as a benchmark material for semicrystalline polymer OSCs. The planar moieties in the backbone of pBTTT facilitate its LC nature which results in high ordering of the π-π stacking. The mobility of 1 cm$^2 \cdot$V$^{-1} \cdot$s^{-1} is reported for pBTTT which is among the highest for organic polymers.[2.20] Stronger π-π interaction is achieved for pNDTBT (**Figure 2.7**b) due to a smaller π stacking distance (0.36 nm compared to 0.37 nm of pBTTT), and also high carrier mobility of > 0.5 cm$^2 \cdot$V$^{-1} \cdot$s^{-1} was reported.[2.21]

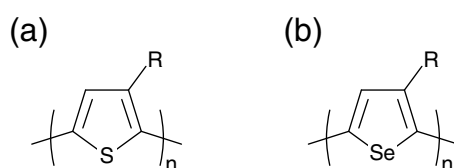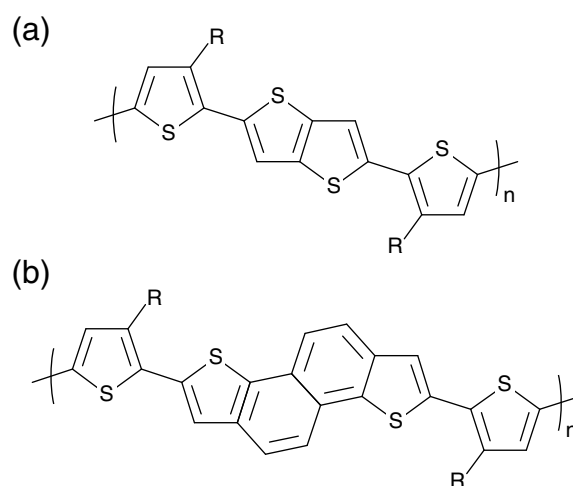**Figure 2.7**   Molecular structures of (a): pBTTT, and (b): pNDTBT.

As for the D-A type polymer organic semiconductor material, poly(2,5-bis(3-alkyl-5-(3-alkylthiophen-2-yl)thiophen-2-yl)thiazolo[5,4-d]thiazole) (pTzQT) was reported (**Figure 2.8**a).[2.21] This polymer exhibits very strong intermolecular interactions in the π stacking direction due to polarization and shows mobility of ~0.3 cm$^2 \cdot$V$^{-1} \cdot$s^{-1}. The mobility is reported to become higher for longer alkyl chains because highly ordered lamellar structures are formed in the polymers with longer side chains.[2.22] Recently, a well-designed D-A copolymer poly[4-(4,4-dihexadecyl-4H-cyclopenta[1,2-b:5,4-b']-dithiophen-2-yl)-alt-[1,2,5] thiadiazolo[3,4-c]pyridine] (PCDTPT) shown in **Figure 2.8**b was reported.[2.23] By aligning the polymer backbone structures with nanostructures formed on the substrate surface, very high carrier mobility of OFETs of > 10 cm$^2 \cdot$V$^{-1} \cdot$s^{-1} was achieved[2.24] which is comparable to highest values achieved for small molecule OSC. The downside of the D-A copolymers is their relatively low crystallinity which may result in low operational stability of OFETs. In an attempt to combine the benefits of semicrystalline and D-A OSCs, poly (didodecylquaterthiophene-alt-didodecylbithiazole) (PQTBTz-C12) was synthesized (**Figure 2.8**c).[2.25] This material is a D-A type copolymer exhibiting LC nature and it shows carrier mobility of ~0.3 cm$^2 \cdot$V$^{-1} \cdot$s^{-1}.[2.26]
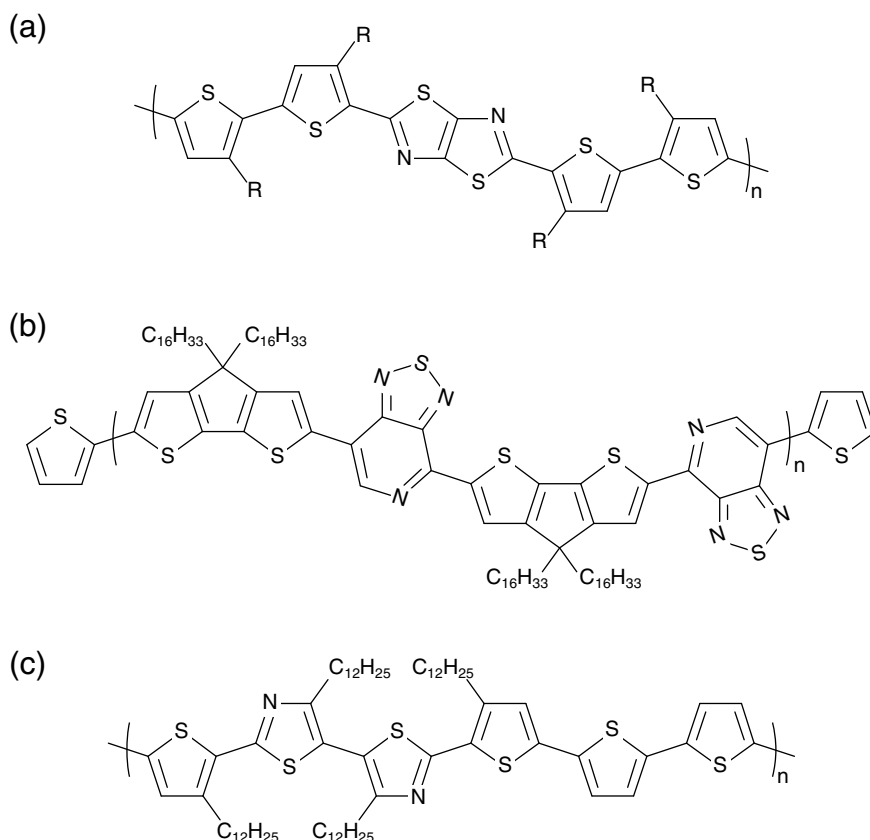
Figure 2.8　Molecular structure of (a): pTzQT, (b): PCDTPT, and (c): PQTBTz-C12.

2.3　pBTTT-C16

　　pBTTT-C16 was chosen as a semiconducting polymer for this study because of three main reasons. First, it is a promising LC semiconducting polymer for solution-processed OFETs showing a field-effect hole mobility comparable to that of *a*-Si FETs($\sim$0.5 cm$^2 \cdot$V$^{-1} \cdot$s^{-1}). Second, OFETs with pBTTT as an active layer are expected to show high operational stability due to high crystallinity of this material.[2.27] Finally, it is a typical polymeric semiconducting material that shows the trade-off relationship between the ease of coating on hydrophobic surfaces and the OFET device performance.[2.20] The structure of pBTTT-C16 is shown in **Figure 2.9**a. The molecular weight of pBTTT-C16 used in this study was 37600 g/mol.[2.28]

　　Figure 2.9b shows a differential scanning calorimetry (DSC) data of pBTTT-C16.[2.28] At room temperature, alkyl chains of crystalline pBTTT-C16 form a nested structure. At around 140°C, alkyl chains of pBTTT-C16 melt and it transits to a smectic phase.[2.29] In this phase, the backbone aligns into a laminar structure, and domains grow in the in-plane direction.[2.27],[2.29],[2.30] After a cycle of crystalline phase → smectic phase → crystalline phase, a terrace phase with clear molecular steps is formed. Such film shows high carrier mobility.[2.30] If pBTTT-C16 is further heated to 240°C, the backbone structures melt, and it overgoes a second phase transition. After cooling from this phase, ribbon shaped domains form on the film surface. OFETs using ribbon phase pBTTT-C16 as an active layer are also reported although the mobility is lower than that of terrace-phase pBTTT-C16 OFETs (0.1 $\sim$ 0.4 cm$^2 \cdot$V$^{-1} \cdot$s^{-1}).
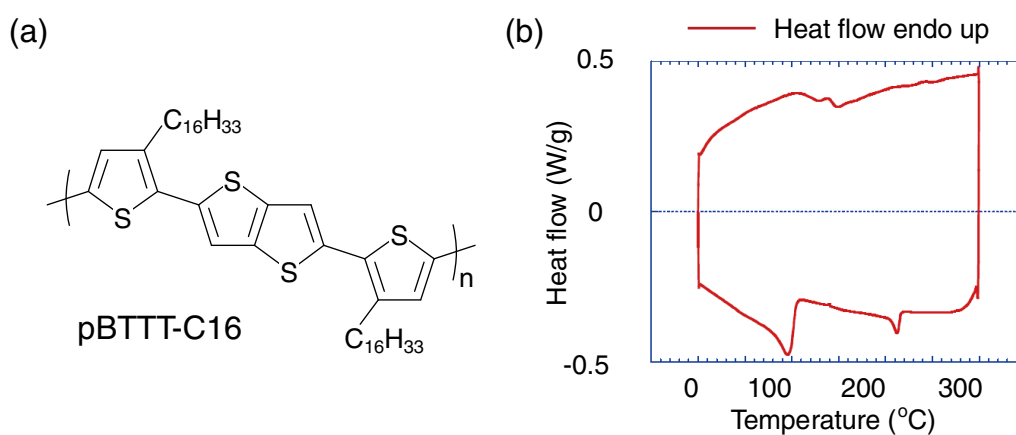
Figure 2.9 (a): Chemical structure of pBTTT-C16 and (b) its differential scanning calorimetry data (obtained from ref.[2.28]).

2.4 OSC film formation

a) Dry process

Dry process is a process in which the target material is vaporized and is deposited on the substrate by condensation. The deposition process is performed in vacuum and is illustrated in **Figure 2.10**. The advantages of the dry process are that it can be used for depositing insoluble materials, that very uniform films can be formed, and that the film can be easily patterned by the use of shadow masks. The disadvantages are the higher cost compared to wet processes, and limited size of the deposition area.
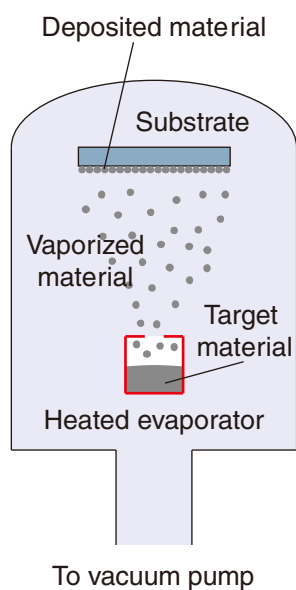
Figure 2.10 Schematic illustration of the vapor deposition process.

b) Solution processes

Organic semiconductor film formation from solution is possible only for soluble materials. Though the application is rather limited, solution processes are more cost effective than the dry process because the vacuum conditions are not required. Many solution processes have been reported each having its own advantages. In this section, some popular processes for OFET fabrication are explained.

i) Drop casting

Drop casting is a very simple process for film formation in which the droplet of organic semiconductor solution is cast on a substrate, and the film is formed by evaporation of solution (**Figure 2.11**). The substrate can be leveled[2.31] or inclined.[2.32] In the latter case, anisotropic films can be formed. The main advantage of this method is its simplicity, and the disadvantages are limitation in the coverage area, difficulty of thickness control, and poor film uniformity.
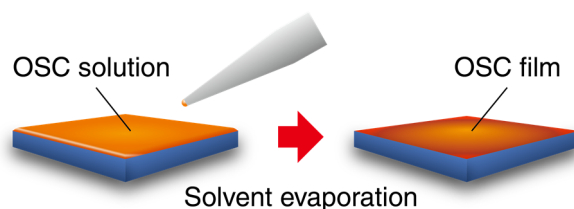
Figure 2.11   Schematic illustration of drop casting process.

ii) Spin-coating

Spin-coating is a very common method to form uniform films on a flat small-area surface.[2.33],[2.34] To form organic semiconductor film by spin-coating, the substrate is first fixed to a rotatable holder. Then, the solution of organic semiconductor material is dropped on the substrate, and the substrate is spun at a constant or varying speed. The process of the film formation during spin-coating is illustrated in **Figure 2.12**. The main disadvantages are the relatively large usage of solution and the non-scalability.
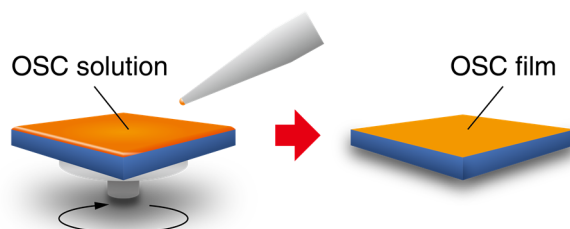
Figure 2.12   Schematic illustration of spin-coating process.

iii) Zone casting

In the zone casting method, the substrate is fixed to a movable stage and is located under the fixed flat nozzle. While the substrate is moved in a certain direction, the organic semiconductor solution is supplied to the evaporation zone through the nozzle, and the film is formed on the moving substrate. The schematic

illustration of this process is shown in **Figure 2.13**. This process is unidirectional and can produce aligned semiconductor thin films.[2.35] Also, the usage of the solution in this method is very low since only the needed amount is supplied.
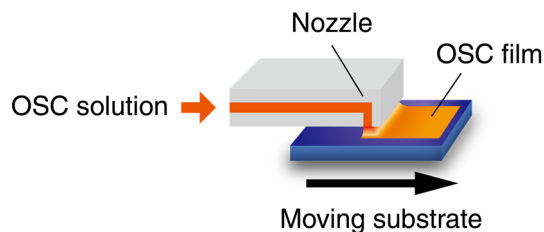
Figure 2.13   Schematic illustration of zone casting process.

iv) Inkjet printing

Inkjet printing is an accurate and reproducible method for organic semiconductor film formation in which the solution is dispersed as individual sub-nanoliter droplets on the substrate from a nozzle.[2.36] The droplet size, spacing, and printing area can be accurately controlled. This makes uniform film formation on desired area possible with minimum usage of solution. Patterning is possible without using masks or lithography which can decrease cost significantly. Surface modifications combined with lithography can be used to further increase the printing accuracy.[2.37]

v) Flow-coating

In the flow-coating method, the substrate is kept stationary, and the organic semiconductor solution is held between the substrate and the movable blade by a capillary force. The blade is slightly inclined against the substrate surface to hold the solution at the tip. As the blade is moved parallel to the substrate surface plane, the organic semiconductor solution evaporates and the thin film forms (**Figure 2.14**). Since the flow-coating is a unidirectional coating process, the films produced by flow-coating are anisotropic.[2.38]
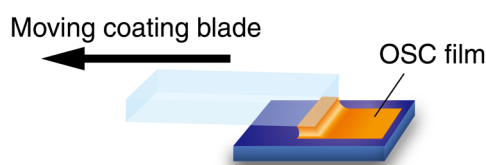
Figure 2.14   Schematic illustration of flow-coating process.

2.5   Gate dielectric surface modifications

Self-assembled monolayers (SAMs) are often used to improve device performance of OFETs. The charge transport of OFETs occurs within a very thin (2-3 nm-thick) area of the active layer from the interface with the gate dielectric. Thus, the defects and impurities of the insulator layer, its flatness and the surface energy have a great influence on the mobility of OFETs. Controlling these factors is important for improving device performance. The surface energy of the gate dielectric layer can be controlled by using SAMs. SAMs
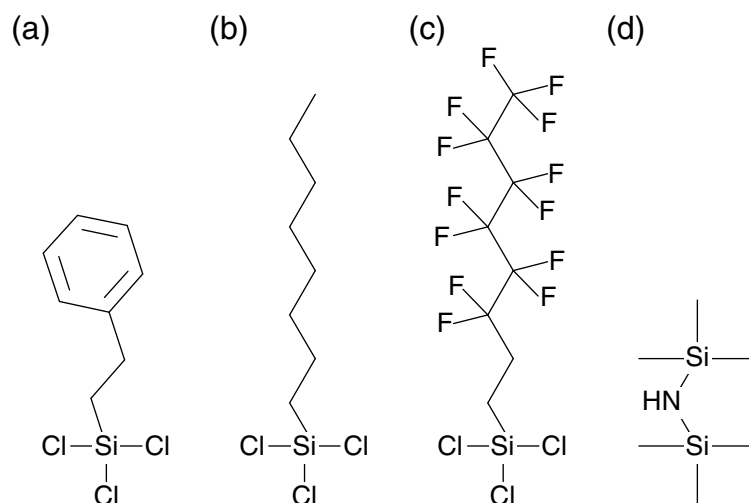
Figure 2.15   Molecular structures of a): PTS, b): OTS, c): FOTS, and d): HMDS.

are single molecule thick assemblies, spontaneously formed on the surfaces by adsorption (either weak physi-sorption or strong chemi-sorption). In most cases, the molecule that forms a monolayer consists of 'head', 'tail', and 'functional' groups. The head group anchors the molecule to the substrate and assemble together. The tail groups are used for organizing the molecules far from the substrate. The functional group determines the surface energy of the layer. Different functional groups can be selected to obtain desired surface energy, and the head groups can be varied to match the target substrate surface. For treating the SiO_2 surface, the trichlorosilane heads are often used. Most used examples of SAMs for treating SiO_2 are: phenyltrichlorosilane (PTS), alkyltrichlorosilanes such as octyltrichlorosilane (OTS) and octadecyltrichlorosilane (ODTS), fluoroalkyltrichlorosilanes such as fluorooctyltrichlorosilane (FOTS), and HMDS.[2.20] The molecular structures of these self-assembly materials are shown in **Figure 2.15**. Since the SAM formation happens spontaneously by adsorption and intermolecular interactions, various fabrication methods can be used. These include vapor deposition, immersion in solution, and spin-coating.

Surfaces with low surface energy induce edge-on orientation of the semiconductor molecules which is preferable for charge transport in the source-drain direction of OFETs. The hydrophobic surfaces are also important for the operational stability because it is related to the residual water. Such surfaces can be obtained, for instance, by the use of alkyl or fluoroalkyl SAMs. For pBTTT-C16, which is the material used in this research, the influence of surface energy on the mobility of OFETs was investigated[2.20], and very high carrier mobility was reported on hydrophobic surfaces. Although decrease of surface energy of the gate dielectric surface leads to increase of carrier mobility, solution-coating on low surface energy (hydrophobic and lyophobic) surfaces faces difficulties due to the dewetting on the OSC solution. This is because the lyophobicity of a solid surface against common organic solvents increases with its hydrophobicity. For instance, it is reported[2.22] that octyltrichlorosilane-treated SiO_2 surfaces on which the contact angle of a water droplet was 95° could not be spin-coated with a 0.2 wt.% warm solution of pBTTT-C16 in *o*-dichlorobenzene (*o*-DCB) due to dewetting of the solution. Thus, the ease of coating and the device performance improvement is in a trade-off relationship, which is a serious problem in fabricating OFETs by solution processing. Therefore, the development of a solution coating technique to form organic thin films on lyophobic (highly hydrophobic) surfaces was strongly desired.[2.39]

References

[2.1] J. Zaumseil and H. Sirringhaus. "Electron and Ambipolar Transport in Organic Field-Effect Transistors." *Chem. Rev.* **2007**, 107, 1296.

[2.2] F. Garnier, G.Horowitz, X. Z. Peng, and D. Fichou. "Structural Basis for High Carrier Mobility In Conjugated Oligomers." *Synth. Met.* **1991**, 45, 163.

[2.3] H. Kaiji, H. Okuya, A. Sakakibara, and Y. Ohmori. "Oligothiophene Organic Transistors Using Poly(3-hexylthiophene) Fabricated by Spin Coating." *Jpn. J. Appl. Phys.* **2005**, 44, L1568.

[2.4] A. Dodabalupar, L. Torsi, and H. E. Katz. "Organic Transistors: Two-Dimensional Transport and Improved Electrical Characteristics" *Science* **1995**, 286, 270.

[2.5] M. Halik, H. Klauk, U. Zschieschang, G. Schmid, S. Ponomarenko, S. Kirchmeyer, and W. Wiber. "Relationship Between Molecular Structure and Electrical Performance of Oligothiophene Organic Thin Film Transistors." *Adv. Mater.* **2003**, 15, 917.

[2.6] J. A. Letizia, A. Facchetti, C. L. Stern, M. A. Ratner, and T. J. Marks. "High Electron Mobility in Solution-Cast and Vapor-Deposited Phenacyl-Quaterthiophene-Based Field-Effect Transistors: Toward N-Type Polythiophenes." *J. Am. Chem. Soc.* **2005**, 127, 13476.

[2.7] S. F. Nelson, Y.-Y. Lin, D. J. Gundlach, and T. N. Jackson. "Temperature-Independent Transport in High-Mobility Pentacene Transistors." *Appl. Phys. Lett.* **1998**, 72, 1854.

[2.8] M. Mottaghi and G. Horowitz. "Field-Induced Mobility Degradation in Pentacene Thin-Film Transistors" *Organic Electronics* **2006**, 7, 528.

[2.9] S. K. Park, T. N. JacksonJohn, J. E. Anthony, and D. A. Mourey. "High Mobility Solution Processed 6,13-bis(triisopropyl-tilylethynyl) Pentacene Organic Thin Film Transistors." *Appl. Phys. Lett.* **2007**, 91, 063514.

[2.10] H. Ebata, T. Izawa, E. Miyazaki, K. Takimiya, M. Ikeda, H. Kuwabara, and T. Yui. "Highly Soluble [1]Benzothieno[3,2-b]benzothiophene (BTBT) Derivatives for High-Performance, Solution-Processed Organic Field-Effect Transistors." *J. Am. Chem. Soc.* **2007**, 129, 15732.

[2.11] L. Jiang, J. Liu, X. Lu, L. Fu, Y. Shi, J. Zhang, X. Zhang, H. Geng, Y. Hu, H. Dong, L. Jiang, J. Yu, and W. Hu. "Controllable Growth of C8-BTBT Single Crystalline Microribbon Arrays by a Limited Solvent Vapor-Assisted Crystallization (LSVC) Method." *J. Mater. Chem. C* **2018**, 6, 2419.

[2.12] T. Izawa, E. Miyazaki, and K. Takiyama. "Molecular Ordering of High-Performance Soluble Molecular Semiconductors and Re-evaluation of Their Field-Effect Transistor Characteristics." *Adv. Mater.* **2008**, 20, 3388.

[2.13] K. Takimiya, H. Ebata, K. Sakamoto, T. Izawa, T. Otsubo, and Y. Kunugi. "2,7-Diphenyl[1] benzothieno[3,2-b]benzothiophene, A New Organic Semiconductor for Air-Stable Organic Field-Effect Transistors with Mobilities up to 2.0 cm^2 V^{-1} s^{-1}" *J. Am. Chem. Soc.* **2006**, 128, 12604.

[2.14] T. Matsumoto, W. Ou-Yang, K. Miyake, T. Uemura, and J. Takeya. "Study of Contact Resistance of High-Mobility Organic Transistors Through Comparisons." *Org. Electron.* **2013**, 14, 2590.

[2.15] T. Uemura, K. Nakayama, Y. Hirose, J. Soeda, M. Uno, W. Li, M. Yamagishi, Y. Okada, J. Takeya. "Band-Like Transport in Solution-Crystallized Organic Transistors." *Curr. Appl. Phys.* **2012**, 12, S87.

[2.16] S. Wang, M. Wang, X. Zhang, X. Yang, Q. Huang, X. Qiao, H. Zhang, Q. Wu, Y. Xiong, J. Gaoc, and H. Li. "Donor–Acceptor–Donor Type Organic Semiconductor Containing Quinoidal Benzo-[1,2-B:4,5-B0]dithiophene for High Performance n-Channel Field-Effect Transistors." *Chem. Commun.* **2014**, 50, 985.

[2.17] B. Lim, H. Sun, J. Lee, and Y.-Y. Noh. "High Performance Solution Processed Organic Field Effect Transistors with Novel Diketopyrrolopyrrole-Containing Small Molecules." *Sci. Rep.* **2017**, 7, 164.

[2.18] H. Sirringhaus, P. J. Brown, R. H. Friend, M. M. Nielsen, K. Bechgaard, B. M. W. Langeveld-Voss, A. J. H. Spiering, R. A. J. Janssen, E. W. Meijer, P. Herwig, and D. M. de Leeuw. "Two-Dimensional Charge Transport in Self-Organized, High-Mobility Conjugated Polymers." *Nature* **1999**, 401, 685.

[2.19] M. Heeney, W. Zhang, D. J. Crouch, M. L. Chabinyc, S. Gordeyev, R. Hamilton, S. J. Higgins, I. McCulloch, P. J. Skabara, D. Sparrowe, and S. Tierney. "Regioregular poly(3-hexyl)selenophene: a

Low Band Gap Organic Hole Transporting Polymer." *Chem. Commun.* **2007**, 47, 5061.

[2.20] T. Umeda, D. Kumaki, and S. Tokito. "Surface-Energy-Dependent Field-Effect Mobilities up to 1 cm^2 /V s for Polymer Thin-Film Transistor." *J. Appl. Phys.* **2009**, 105, 024516.

[2.21] I. Osaka, T. Abe, S. Shimamura, E. Miyazaki, and K. Takimiya. "High-Mobility Semiconducting Naphthodithiophene Copolymers" *J. Am. Chem. Soc*. **2010**, 132, 5000.

[2.22] T. Umeda, S. Tokito, and D. Kumaki. "High-Mobility and Air-Stable Organic Thin-Film Transistors with Highly Ordered Semiconducting Polymer Films." *J. Appl. Phys.* **2007**, 101, 054517.

[2.23] L. Ying, B. B. Y. Hsu, H. Zhan, G. C. Welch, P. Zalar, L. A. Perez, E. J. Kramer, T.-Q. Nguyen, A. J. Heeger, W.-Y. Wong, and G. C. Bazan. "Regioregular Pyridal[2,1,3]thiadiazole π-Conjugated Copolymers." *J. Am. Chem. Soc.* **2011**, 133, 18538.

[2.24] C. Luo, A. K. K. Kyaw, L. A. Perez, S. Patel, M. Wang, B. Grimm, G. C. Bazan, E. J. Kramer, and A. J. Heeger. "General Strategy for Self-Assembly of Highly Oriented Nanocrystalline Semiconducting Polymers with High Mobility." *Nano Lett.* **2014**, 14, 2764.

[2.25] D. H. Kim, B.-L. Lee, H. Moon, H. M. Kang, E. J. Jeong, J.-I. Park, K.-M. Han, S. Lee, B. W. Yoo, B. W. Koo, J. Y. Kim, W. H. Lee, K. Cho, H. A. Becerril, and Z. Bao. "Liquid-Crystalline Semiconducting Copolymers with Intramolecular Donor−Acceptor Building Blocks for High-Stability Polymer Transistors." *J. Am. Chem. Soc.* **2009**, 131, 6124.

[2.26] D. H. Kim, J. Lee, J.-I. Park, J. W. Chung, W. H. Lee, G. Giri, B. Yoo, B. Koo, J. Y. Kim, Y. W. Jin, K. Cho, B.-L. Lee, and S. Lee. "Molecular Weight-Induced Structural Transition of Liquid-Crystalline Polymer Semiconductor for High-Stability Organic Transistor." Adv. Funct. Mater. **2011**, 21, 4442.

[2.27] I. McCulloch, M, Heeney, C. Bailey, K. Genevicus, I. MacDonald, M. Shkunov, D. Sparrowe, S. Tierney, R. Wagner, W. Zhang, M. L. Chabinyc, R. J. Kline, M. D. Mcgehee, and M. F. Toney. "Liquid-Crystalline Semiconducting Polymers with High Charge-Carrier Mobility." *Nature Mater.* **2006**, 5, 328.

[2.28] Provided by Merck Chemicals Ltd.

[2.29] D. M. DeLongchamp, R. J. Kline, E. K. Lin, D. A. Fischer, L. J. Richter, L. A. Lucas, M. Heeney, I. McCulloch, and J. E. Northrup. "High Carrier Mobility Polythiophene Thin Films: Structure Determination by Experiment and Theory." *Adv. Mater.* **2007**, 19, 833.

[2.30] M. L. Chabinyc, M. F. Toney, R. J. Kline, I. McCulloch, and M. Heeney. "X-Ray Scattering Study of Thin Films of poly(2,5-bis(3-alkylthiophen-2-yl)thieno[3,2-b]thiophene)." *J. Am. Chem. Soc.* **2007**, 129, 3226.

[2.31] T. Minari, Y. Kanehara, C. Liu, K. Sakamoto, T. Yasuda, A. Yaguchi, S. Tsukada, K. Kashizaki, and M. Kanehara. "Room-Temperature Printing of Organic Thin-Film Transistors with π-Junction Gold Nanoparticles." *Adv. Funct. Mater.* **2014**, 24, 4886.

[2.32] W. H. Lee, D. H. Kim, Y. Jang, J. H. Cho, M. Hwang, Y. D. Park, Y. H. Kim, J. I. Han, and K. Cho. "Solution-Processable Pentacene Microcrystal Arrays for High Performance Organic Field-Effect Transistors." *Appl. Phys. Lett.* **2007**, 90, 132106.

[2.33] F. Zhang, C. Di, N. Berdunov, Yuanyuan Hu, Yunbin Hu, X. Gao, Q. Meng, H. Sirringhaus, and D. Zhu. "Ultrathin Film Organic Transistors: Precise Control of Semiconductor Thickness via Spin-Coating." *Adv. Mater.* **2013**, 25, 1401.

[2.34] Z. Bao, A. Dodabalapur, and A. J. Lovinger. "Soluble and Processable Regioregular poly(3-hexylthiophene) for Thin Film Field-Effect Transistor Applications with High Mobility." *Appl. Phys. Lett.* **1996**, 69, 26.

[2.35] M. J. Lee, D. Gupta, N. Zhao, M. Heeney, I. McCulloch, and H. Sirringhaus. "Anisotropy of Charge Transport in a Uniaxially Aligned and Chain-Extended, High-Mobility, Conjugated Polymer Semiconductor." *Adv. Funct. Mater.*, **2011**, 21 932.

[2.36] A. Teichler, J. Perelaerabc, and U. S. Schubert. "Inkjet Printing of Organic Electronics – Comparison of Deposition Techniques and State-of-the-Art Developments." *J. Mater. Chem. C* **2013**, 1, 1910.

[2.37] L. Teng, M. Plötner, A. Türke, B. Adolphi, A. Finn, R. Kirchner, W.-J. Fischer. "Nanoimprint Assisted Inkjet Printing to Fabricate Sub-Micron Channel Organic Field Effect Transistors."

Microelectron. Eng. **2013**, 110, 292.

[2.38] D. M. DeLongchamp, R. J. Kline, Y. Jung, D. S. Germack, E. K. Lin, A. J. Moad, L. J. Richter, M. F. Toney, M. Heeney, I. McCulloch, *ACS Nano* **2009**, 3, 780.

[2.39] M. Ikawa, T. Yamada, H. Matsui, H. Minemawari, J. Tsutsumi, Y. Horii, M. Chikamatsu, R. Azumi, R. Kumai, and T. Hasegawa. "Simple Push Coating of Polymer Thin-Film Transistors." *Nat. Commun.* **2012**, 3, 1176.

Chapter 3   Solution coating on highly hydrophobic surfaces

The hydrophobization (lyophobization) of the gate dielectric surface is a powerful technique to improve the performance of the OFETs. The hydrophobicity is preferred to be as high as possible.[3.1] However, the ease of coating of the OSC film and the hydrophobicity of the gate dielectric surfaces are typically in trade-off relationship due to the repellent property of such surfaces against common organic solvents. In this chapter, simple techniques that can solve this problem are reported. Producing specially designed lyophobic/lyophilic pattern on the surface enables continuous and uniform OSC film formation on both lyophilic and lyophobic areas.[3.2] This novel technique was used in combination with flow- and spin-coating methods and the properties of the resulting OSC films are discussed.

3.1   Preparation of hydrophobic/hydrophilic patterned surfaces

In this thesis, the focus was on the establishment of the OSC film formation process. For this purpose, heavily doped n-type Si(100) wafers (20 × 20 mm^2) with thermally grown SiO$_2$ layers (SiO$_2$/n$^+$-Si) (SiO$_2$ thickness: ~100 or ~300 nm) were used as substrates. The n$^+$-Si was used as a common gate electrode in OFETs and the SiO$_2$ layer is a reliable pin-hole-free insulator. Fabrication of the OFETs is explained in detail in the next chapter. The substrates were cleaned by immersion for 10 min three times in a piranha solution, which is a mixture of sulfuric acid and hydrogen peroxide and rinsed several times with deionized water. The clean substrates were kept in deionized water and dried with nitrogen gas blow immediately prior to the usage or further treatment.

The surface hydrophobization (lyophobization) was performed by formation of ODTS SAM. Just before the surface treatment, the cleaned substrate was removed from distilled water, dried with nitrogen gas blow, and put in a nitrogen purred glove box. The process of ODTS vapor treatment is shown in **Figure 3.1**a. The substrate and 3 drops of ODTS were put in a petri dish. The petri dish was covered and enclosed in a hermetical container. The container was put on a hot plate set to 120°C. The temperature was held for 3 hours which allowed ODTS to evaporate and form a monolayer on the substrate through self-assembly.[3.3]
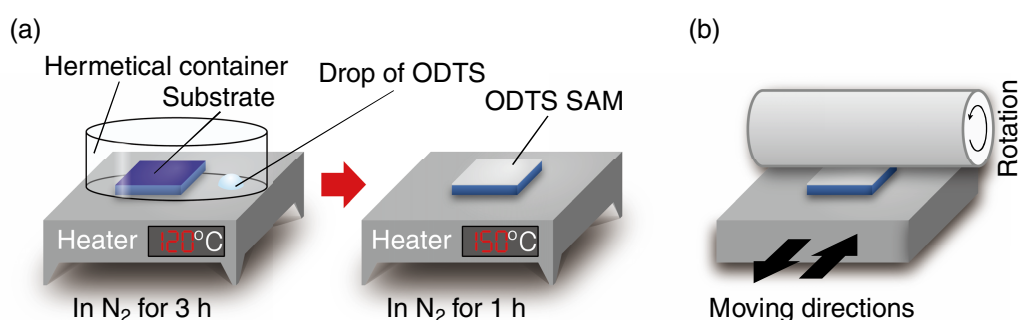
Figure 3.1   (a): Vapor treatment process for ODTS SAM formation. (b): Rubbing process.

After the vapor treatment, the substrate was removed from the container and was washed with anhydrous toluene several times inside of the glove box. After washing, the substrate was removed from the glove box and was subjected to sonication in anhydrous toluene for 10 minutes, in isopropyl alcohol (IPA) for 10 minutes twice and was dried with nitrogen gas blow. After the vapor treatment, the substrate was kept in air for more than 16 hours, and then annealed at 150°C for 1h in nitrogen.

In order to check the uniformity of the ODTS SAM fabricated by vapor treatment, the contact angle measurement was performed for 20 points on each substrate using a contact angle meter (Kyowa DM 500). The image of the water droplet (1.2 μl) on the ODTS vapor treated SiO$_2$ substrate is shown in **Figure 3.2**a. Within one substrate, the variation of contact angles was extremely small (111.6 ± 0.2° for the substrate used for fabrication of the pBTTT-C16 OFET array). The sample-to-sample variation was slightly larger but still very small (110.8 ± 0.9° for 18 ODTS vapor treated substrates). These results show that the ODTS vapor treatment procedure routinely produces highly hydrophobic surfaces with a water contact angle of ~111°.

Figure 3.2   The images of (a, b): water and (c, d, e): *o*-DCB droplets on (a, c): ODTS vapor treated SiO$_2$ substrate surface, (b, d): fluorine-coated glass blade, and (e): dry pBTTT-C16 film. The contact angles of water and *o*-DCB on each surface are shown in the images.

The water contact angle on the fluorine-coated glass plate that was used as a coating blade in SAF-coating was also measured (**Figure 3.2**b) and was found to be ~106°. For the use in the surface en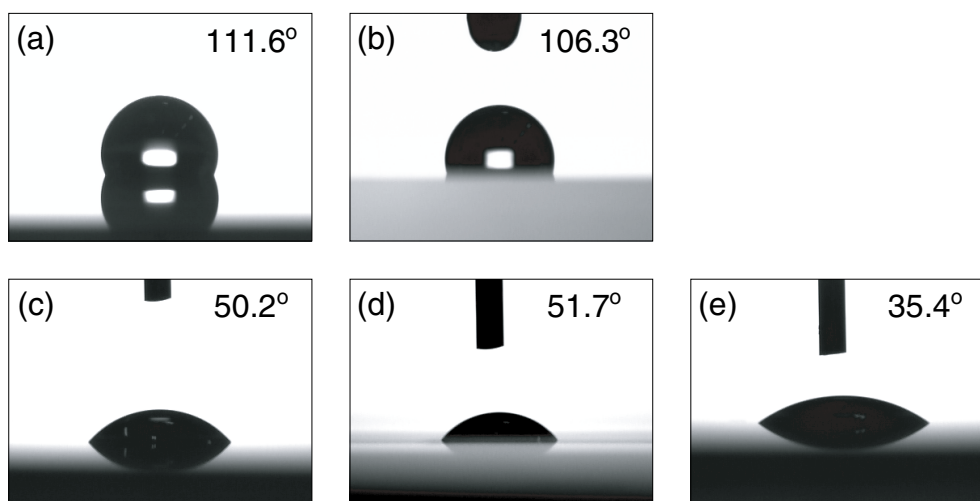ergy calculation which was performed to understand the mechanism of SAF-coating (see **Section 3.3**), the *o*-DCB contact angles on ODTS vapor treated SiO$_2$ substrate, fluorine-coated glass plate, and pBTTT-C16 film **Figure 3.2**c, **Figure 3.2**d, and **Figure 3.2**e, respectively), were measured. The pBTTT-C16 film was dry at the moment of the measurement, and the contact angle was evaluated ~1 s after the *o*-DCB droplet was dropped on the film. The contact angle of *o*-DCB on pBTTT-C16 decreased with time (from 35° to 28° over 3 minutes), which indicated that the contact angle on the wetter film is smaller. The value of 35° was used for the calculation as it is the upper bound for the contact angle on pBTTT-C16 during film formation.

Before proceeding to the patterning process, the ODTS-treated substrate was rubbed with a rayon cloth (Yoshikawa Chemical Co., Ya-18-R) using a home-made rubbing machine.[3.4] The rubbing process is illustrated in **Figure 3.1**b. This treatment can effectively remove polymerized ODTS particles if such exist.

The surface energy patterning is commonly used for area selective coating of OSCs and conductive inks.[3.5] Due to the dewetting of solution in the lyophobic areas, the film is usually formed only in the lyophilic regions. On the other hand, in this thesis, the surface patterning was used to enable the OSC film formation on both lyophilic and lyophobic surface areas.[3.2] The patterning of surfaces covered with alkyl SAMs such as ODTS can be performed by exposing the SAM to VUV light through a photomask. The process is schematically shown in **Figure 3.3**.

The surface patterning was performed by exposing ODTS SAM to VUV light of 172 nm wavelength through a specially designed photomask.[3.6]-[3.9] The excimer light irradiation unit (Ushio SUS06) was used in this research. The process was schematically shown in **Figure 3.3**. The mask was placed 20 μm above the substrate to produce an air layer which enables efficient removal of ODTS by light irradiation. The substrate was exposed to VUV light for 60 seconds. After the treatment, the substrate was washed by sonication in toluene and 2-propanol for 5 minutes each and dried with nitrogen gas blow. It was confirmed that the exposed area become lyophilic showing *o*-DCB contact angle of less than 8°.
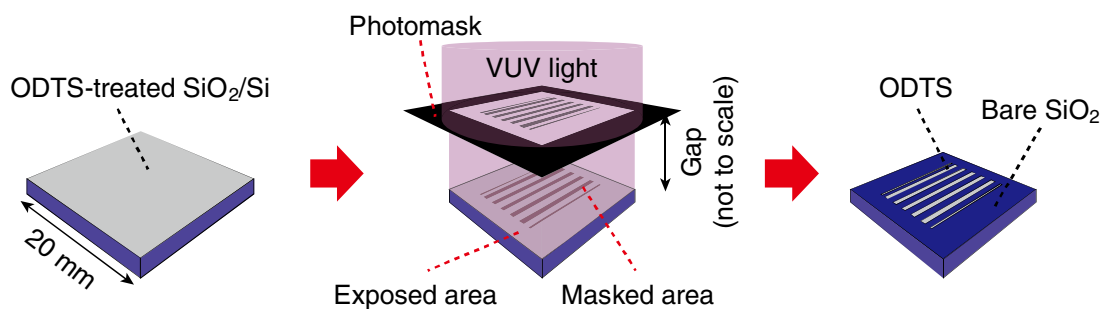
Figure 3.3   Photo-patterning process for ODTS.

3.2   OSC film formation by Self-assisted flow (SAF)-coating

The *Self-assisted flow-coating* (SAF-coating) method[3.2] is based on flow-coating, which is a scalable unidirectional solution coating technique comparable with roll-to-roll processing.[3.10] The flow-coating method was already described in **Chapter 2** and is illustrated again in **Figure 3.4**a. As expected, the flow-
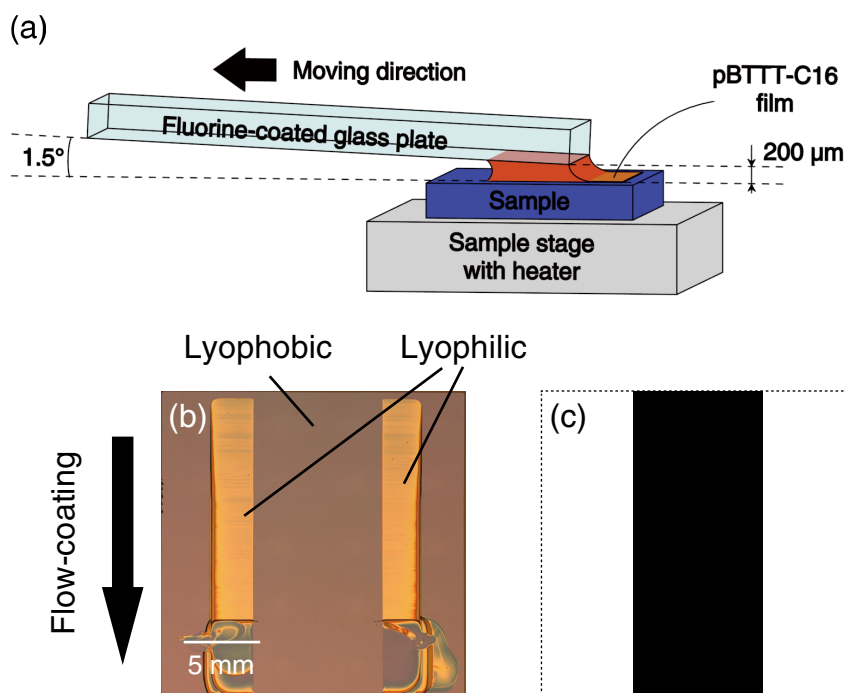
Figure 3.4   (a): Flow-coating method. (b) Dewetting of pBTTT-C16 solution on a lyophobic surface and film formation on lyophilic surfaces by flow-coating method. (c): Photomask pattern used to produce the surface in (b).

coating method fails to produce continuous and uniform OSC films on lyophobic ODTS-treated SiO$_2$ surfaces as shown in **Figure 3.4**b. A lyophobic/lyophilic pattern produced by VUV-light exposure through a photomask pattern shown in **Figure 3.4**c was used to demonstrate both film formation by flow-coating and dewetting on a lyophobic surface, simultaneously.

However, the breakthrough for this problem was found in this study. The OSC film formation on both lyophilic and lyophobic areas was enabled by producing a specially designed lyophobic/lyophilic pattern shown in **Figure 3.5**a on a gate insulator surface. A useful pattern of lyophilic areas is a rectangle followed by stripe lines aligned parallel to the coating direction. During flow-coating, the top rectangular region acts as the initial nucleation area, and the stripe lines contribute to the stabilization of the contact line pinning in the lyophobic areas. By starting the flow-coating from the top lyophilic rectangular region, the organic semiconductor thin film continuously grows on both lyophilic and lyophobic surfaces in the stripe pattern region because the flow-coated organic semiconductor film itself acts as the lyophilic surface for the semiconductor solution as will be explained below.
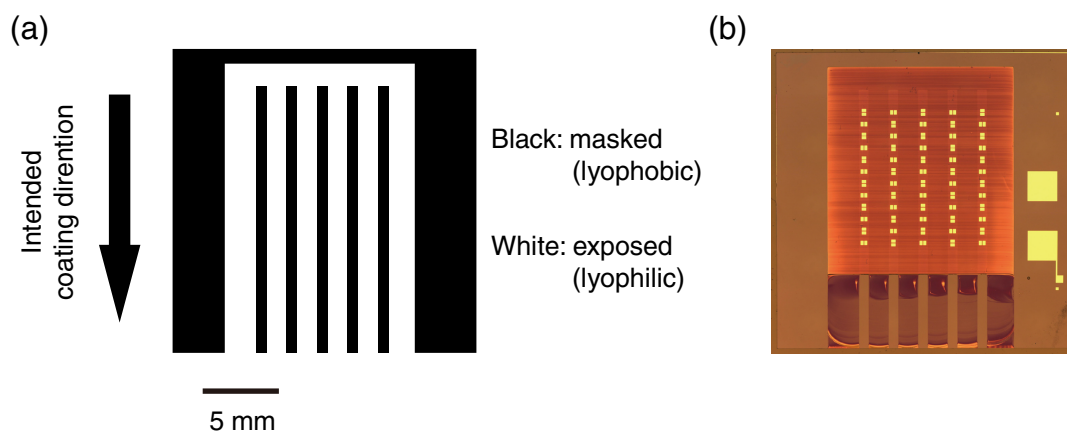

Figure 3.5   (a): Effective photomask pattern for pBTTT-C16 film formation by flow-coating. (b): pBTTT-C16 film formed by SAF-coating (after formation of S/D electrodes) using the lyophobic/lyophilic pattern fabricated with (a).

SAF-coating was conducted with a home-made flow-coater illustrated in **Figure 3.4**a (see the computer-generated images of the whole process in **Figure 3.11** below). The lyophobic/lyophilic pattern shown in **Figure 3.5**a (the 1.5 mm-long fully lyophilic area at the beginning of the coating) was effective for enabling the film formation on both lyophilic and lyophobic surface areas as will be explained in **Section 3.3**. The whole coating process was performed in a nitrogen purged glove box. After the coating, the substrate was annealed at 150°C for 15 minutes in nitrogen atmosphere to obtain terrace phase pBTTT-C16.[3.11] The resulting pBTTT-C16 film is shown in **Figure 3.5**b.

The contact line shape during flow-coating of pBTTT-C16 was examined with an optical microscope in order to understand the film formation mechanism. The images of the contact line were taken from above. To show the importance of the top lyophilic rectangular area, the contact line shape was examined for two different starting positions of flow-coating. The starting positions are indicated in **Figure 3.6**a. The images of the resulting contact lines taken at the same position (indicated by a rectangular box in **Figure 3.6**a) are shown in **Figure 3.6**b and **Figure 3.6**c. When the coating was started from the top lyophilic region, the contact line was straight and was located at ~0.14 mm from the leading edge of the movable blade as shown in **Figure 3.6**b. The adequate spread of solution toward the starting line was kept in both lyophobic and lyophilic surface areas

during flow-coating, resulting in continuous film formation on both lyophilic and lyophobic surface areas. However, when the coating was started from the middle of the line-and-space pattern, the contact line could be seen only in the lyophilic surface areas (**Figure 3.6**c). Thus, the contact line on the lyophobic surface areas was located beneath the movable blade. In this case, the film formation occurred only on the lyophilic surface areas but did not occur on the lyophobic surface areas. These results showed that the thin film formation originating in the top lyophilic region helps keeping the adequate spread of organic solution and enables the film formation on lyophobic surface areas.

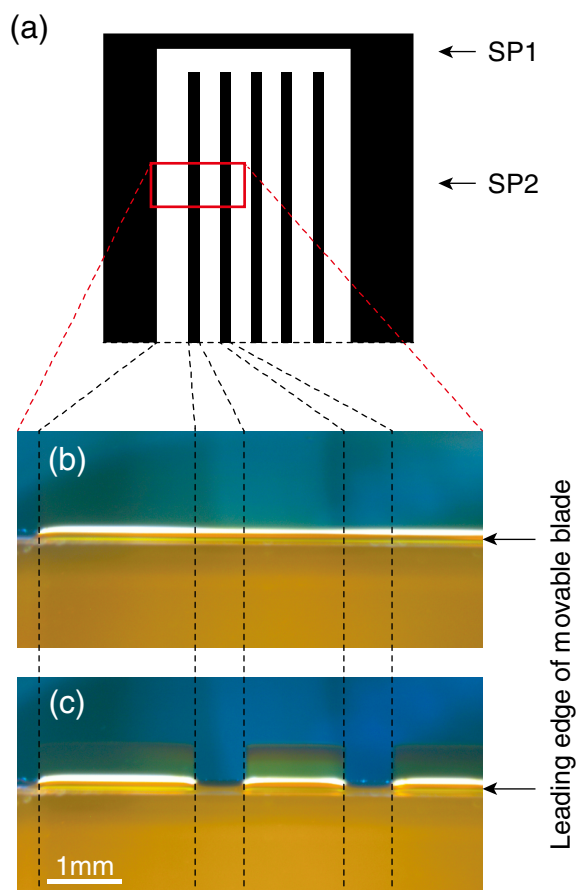**Figure 3.6**   (a): Lyophobic (black) / lyophilic (white) surface pattern used for flow-coating and (b, c): contact lines of pBTTT-C16 solution on the lyophobic/lyophilic surface pattern, when the flow-coating was started from (b): Starting position (SP) 1, and (c): SP2. The two SPs are indicated by arrows in (a). The pictures were taken when the movable blade went through the region indicated by the rectangular box in (a).

3.3 Mechanism of SAF-coating

To understand the mechanism of SAF-coating, the surface energy calculation was performed assuming a simplified solution profile shown in **Figure 3.7**a. For simplicity, the solution surfaces exposed to air are assumed to be flat. Since the contact angles of *o*-DCB droplets on the fluorine-coated glass blade (51°) and the ODTS-treated substrate (50°) were almost the same, the flat solution surface in the substrate-blade gap was assumed to make the same angle (= 90° - α / 2) against both blade and substrate surfaces. The substrate is divided into two: lyophobic and lyophilic areas, and the boundary line is located at ΔL^{pho} from the leading edge of the coating blade. The lyophilic area during the continuous film growth corresponds to the area covered with the pBTTT-C16 film as shown in **Figure 3.7**b.

When the contact line is located at x (> 0) from the leading edge of the coating blade, as shown in **Figure 3.7**a, the total surface energy per unit width (E/w) in the lyophobic line pattern is given by:
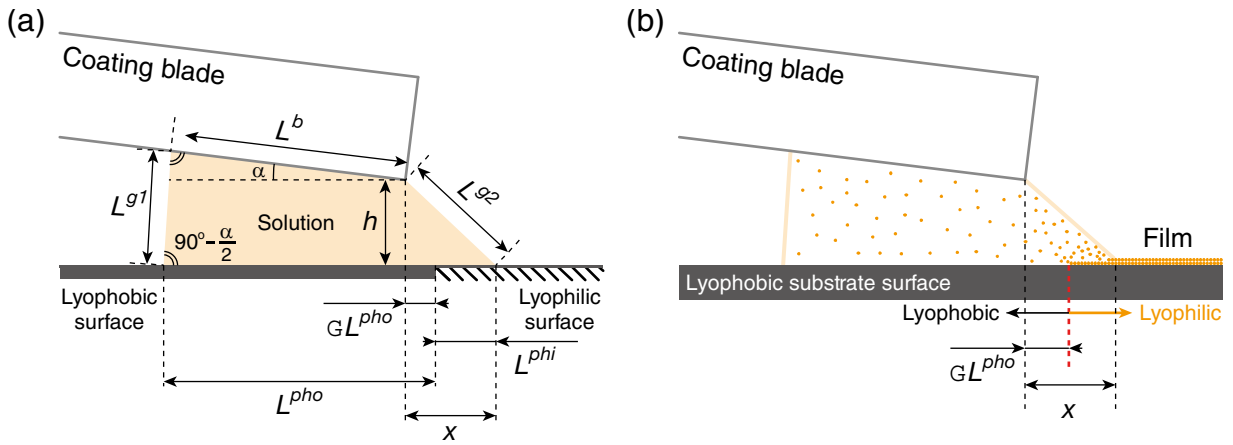
Figure 3.7 (a): Simplified *self-assisted flow-coating* geometry used for the surface energy calculations, and (b): illustration of covering of lyophobic substrate surface with organic semiconductor film during *self-assisted flow-coating*.

$$\frac{E - E_0}{w} = \gamma_{lg}L^g + \left(\gamma_{sl}^b - \gamma_{sg}^b\right)L^b + \left(\gamma_{sl}^{pho} - \gamma_{sg}^{pho}\right)L^{pho} + \left(\gamma_{sl}^{phi} - \gamma_{sg}^{phi}\right)L^{phi}, \tag{3.1}$$

where w is the width of the lyophobic line pattern area; E_0/w is the total energy per unit width of the system without solution; γ_{lg}, γ_{sg}^i, and γ_{sl}^i are the surface energy of liquid, the solid-air interface energy, and the solid-liquid interface energy, respectively, and $i = b, pho, phi$, represent the movable blade, the "lyophobic", and the "lyophilic" surfaces, respectively; and L^b, L^{pho}, L^{phi}, and L^g ($= L^{g1} + L^{g2}$) are the interface lengths between the solution and the blade, between the solution and the lyophobic surface, between the solution and the lyophilic surface, and between the solution and air, respectively. Using the Young's equations ($\gamma_{sl}^i = \gamma_{sg}^i - \gamma_{lg} \cos\theta^i$) we can remove all the interface energies in **Equation 3.1**:

$$\frac{\Delta E}{w\gamma_{lg}} = \left(L^g - L^b \cos\theta^b - L^{pho}\cos\theta^{pho} - L^{phi}\cos\theta^{phi}\right), \tag{3.2}$$

where $\Delta E = E - E_0$, and θ^i are the contact angles. The relationship shown in Young's equations can be understood by considering forces acting on a liquid drop (**Figure 3.8**).

Figure 3.8   Schematic of a liquid drop showing the quantities in Young's equation. Forces per unit length (surface tensions γ_j) that act on the contour of volume element containing the contact line are in equilibrium state.

L^b, L^{pho}, L^{phi}, and L^g can be geometrically calculated from the experimental conditions for given values of x and ΔL^{pho}. The area of the solution profile (S) in Figure 3.12a ca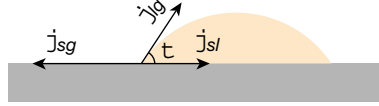n be obtained by dividing the volume of poured solution by the width (w) of the coating blade. S can be expressed as:

$$S = \frac{1}{2}\left\{(h + L_b \sin \alpha) \tan \frac{\alpha}{2}\right\}(h + L_b \sin \alpha) + \frac{1}{2}(2h + L_b \sin \alpha)L_b \cos \alpha + \frac{1}{2}hx. \tag{3.3}$$

By simplifying **Equation 3.3**, we get:

$$\sin \alpha\, L_b^2 + 2hL_b + hx + h^2 \tan \frac{\alpha}{2} - 2S = 0. \tag{3.4}$$

From **Equation 3.4**, we can obtain L^b as a function of x:

$$L_b = \frac{\sqrt{h^2 \cos \alpha + (2S - hx) \sin \alpha} - h}{\sin \alpha}. \tag{3.5}$$

L^{pho} and L^g are expressed using L_b:

$$L^{pho} = \begin{cases} L^b + h \tan \dfrac{\alpha}{2} + x \cdots\cdots\cdots\cdots\cdots (x < \Delta L^{pho}) \\ L^b + h \tan \dfrac{\alpha}{2} + \Delta L^{pho} \cdots\cdots\cdots (x \geq \Delta L^{pho}) \end{cases}, \tag{3.6}$$

$$L^g = L^{g1} + L^{g2} = \frac{h + L^b \sin \alpha}{\cos \dfrac{\alpha}{2}} + \sqrt{x^2 + h^2}. \tag{3.7}$$

L^{phi} varies depending on the relation between x and ΔL^{pho}:

$$L^{phi} = \begin{cases} 0 \cdots\cdots\cdots\cdots\cdots\cdots\cdots (x < \Delta L^{pho}) \\ x - \Delta L^{pho} \cdots\cdots\cdots (x \geq \Delta L^{pho}) \end{cases}. \tag{3.8}$$

From **Equation 3.2** and **Equations 3.5-3.8**, the total surface energy difference per unit width of the system ($\Delta E/w$) is obtained by:

$$\frac{\Delta E}{w\gamma_{lg}} = \frac{\sqrt{h^2 \cos \alpha + (2S - hx) \sin \alpha} - h}{\sin \alpha}\left(2 \sin \frac{\alpha}{2} - \cos \theta^b - \cos \theta^{pho}\right)$$

$$+\sqrt{x^2 + h^2} + \frac{h}{\cos \dfrac{\alpha}{2}} - h \tan \frac{\alpha}{2} \cos \theta^{pho} \tag{3.9}$$

$$-\begin{cases} x \cos \theta^{pho} \cdots\cdots\cdots\cdots\cdots\cdots\cdots\cdots\cdots\cdots\cdots\cdots\cdots (x < \Delta L^{pho}) \\ x \cos \theta^{phi} + \Delta L^{pho}\left(\cos \theta^{pho} - \cos \theta^{phi}\right) \cdots\cdots\cdots (x \geq \Delta L^{pho}) \end{cases}.$$

In **Equation 3.9**, $\Delta E / w$ is divided by the surface energy of the liquid which is a constant. For calculation, the contact angles of pure o-DCB were used ($\theta^b = 51°$, $\theta^{pho} = 50°$, and $\theta^{phi} \leq 35°$ depending on the degree of dryness). The **Figure 3.9** shows the calculated plot of $\Delta E / w\gamma_{lg}$ as a function of x for different values of ΔL^{pho}. Here, θ^{phi} was assumed to be equal to the contact angle of o-DCB on the dry pBTTT-C16 film (35°). From **Figure 3.9**, it can be seen that $\Delta E / w\gamma_{lg}$ has up to two minimums at x^{pho} (≈ 0.057 mm), and x^{phi} (≈ 0.101 mm), depending on the value of ΔL^{pho}, which means that the contact line can potentially be stable or metastable at two different positions depending on the distance to the formed (forming) pBTTT-C16 film.
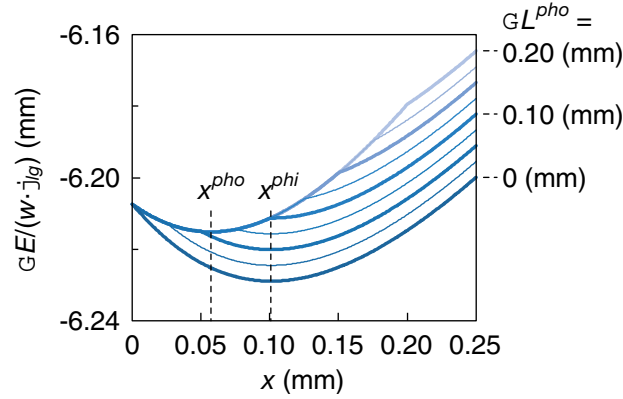
Figure 3.9   Calculated plot of $\Delta E / w\gamma_{lg}$ as a function of x for different values of ΔL^{pho}.

The values of x^{pho} and x^{phi} are obtained by solving

$$0 = \frac{d(\Delta E)}{dx}. \tag{3.10}$$

In order to simplify the calculations, the L_b in the **Equation 3.5** is approximated as

$$L_b(x) \approx -\frac{h}{2\sqrt{h^2 \cos\alpha + 2S \sin\alpha}}x + \frac{\sqrt{h^2 \cos\alpha + 2S \sin\alpha} - h}{\sin\alpha}. \tag{3.11}$$

This approximation holds for

$$x \ll \frac{2(h^2 \cos\alpha + 2S \sin\alpha)}{h \sin\alpha}. \tag{3.12}$$

For the experimental conditions used in this study ($h = 0.2$ mm, $S = 1.43$ mm^2, and $\alpha = 1.5°$), **Equation 3.12** becomes $x \ll 43.8$ mm. Thus, the approximation is acceptable for our conditions. By using **Equation 3.11**, **Equation 3.10** becomes:

$$0 = -\frac{h\left(\cos\theta^b + \cos\theta^{pho} - 2\sin\frac{\alpha}{2}\right)}{2\sqrt{h^2 \cos\alpha + 2S \sin\alpha}} + \frac{x}{\sqrt{x^2 + h^2}}$$
$$+ \begin{cases} \cos\theta^{pho} \cdots\cdots\cdots (x < \Delta L^{pho}) \\ \cos\theta^{phi} \cdots\cdots\cdots (x \geq \Delta L^{pho}) \end{cases}, \tag{3.13}$$

which can be solved for x to give two minimums for ΔE at:

$$x^i = h\sqrt{\frac{K_i^2}{1 - K_i^2}}, \tag{3.14}$$

where

27

$$K_i \equiv \cos \theta^i - \frac{h\left(\cos \theta^b + \cos \theta^{pho} - 2 \sin \frac{\alpha}{2}\right)}{2\sqrt{h^2 \cos \alpha + 2S \sin \alpha}}, \tag{3.15}$$

and $i = pho, phi$.

When ΔL^{pho} is larger than a critical value x^{phi}, a single minimum appears at x^{pho}, which corresponds to the contact line position on the fully lyophobic surface. In this case, solvent evaporation does not induce sufficient concentration gradient near the contact line for film growth, and thus no film formation occurs (**Figure 3.10**a). For the case of $\Delta L^{pho} < x^{phi}$, there is at least a minimum at x^{phi} that corresponds to the contact line position during coating on lyophilic surface. If this condition is satisfied, the adequate spread of organic solution toward the air side is realized as a stable ($\Delta L^{pho} \leq x^{pho}$) or metastable ($x^{pho} < \Delta L^{pho} < x^{phi}$) state, and the thin-film formation occurs. The condition of $\Delta L^{pho} < x^{phi}$ may be satisfied by the covering of the part of the lyophobic substrate surface which is in contact with the solution and near the contact line with a very thin wet pBTTT-C16 layer, as is schematically shown in **Figure 3.10**b.[3.12] Thus, ΔL^{pho} would be nearly equal but slightly smaller than x^{phi}, which is plausible because pBTTT-C16 solution near the contact line becomes supersaturated. Thus, once the film formation occurs (for example in the fully lyophilic area), the contact line on the lyophobic (lyophilic) surface would be pinned to the film growth front in the metastable (stable) state, and the film formation would continue even on the lyophobic surface area. This is the mechanism of SAF-coating.

As was shown in **Figure 3.6**, the contact line was observed at positions $x_o^{pho} \approx 0$ mm, and $x_o^{phi} \approx 0.14$ mm. The values for x^{pho} (≈ 0.057 mm) and x^{phi} (≈ 0.101 mm) obtained by approximate calculations were not in a very good match with observed contact line position probably because this model strongly simplifies the actual shape of the solution profile. However, these calculations may help determine the optimal coating conditions (h, S, and α) for more stable film formation (larger x^{pho} and x^{phi}).
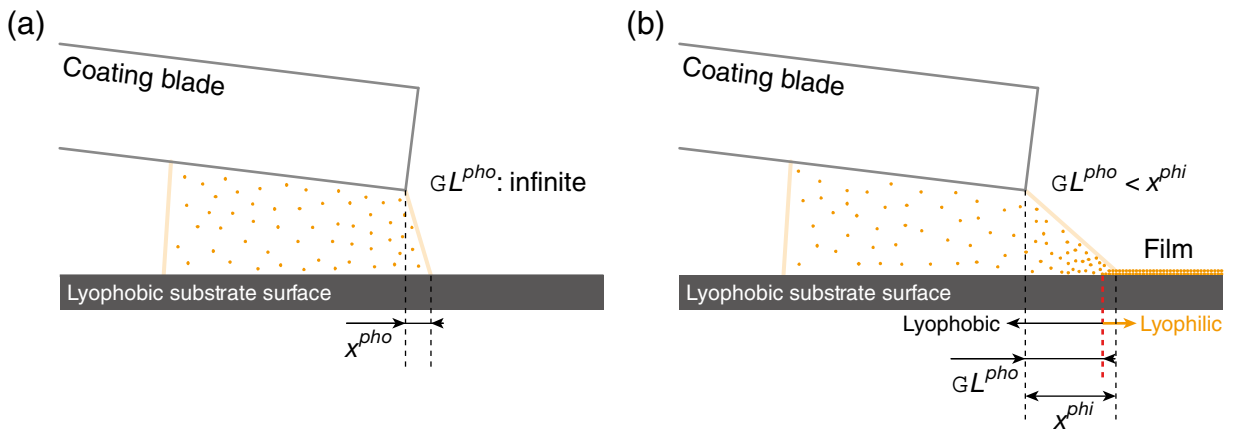

Figure 3.10 (a): Solution profile for fully lyophobic surface ($\Delta L^{pho} = \infty$) in which case no film formation occurs. (b): Solution profile during *self-assisted flow-coating* ($\Delta L^{pho} < x^{phi}$).

3.4   Characterization of SAF-coated OSC film

The flow-coating process adopted for this study is as follows: the substrate was kept stationary on the sample stage, which was heated to 80°C, so that the rubbing direction was parallel to the coating direction; the movable glass blade position was set to the ending line of the coating (15 mm from the top edge of the substrate; see **Figure 3.11**a) to perform the round-trip coating; 20 µl of 0.7 wt.% solution of pBTTT-C16 in *o*-DCB, which was heated on a hot plate set to 120°C, was inserted in the gap space (200 µm gap height) between the substrate and the slightly inclined movable glass blade (1.5° inclination against the substrate surface plane); after waiting for 1 minute in order to stabilize the temperature of both the solution and the substrate, the glass blade was moved at a coating speed of 1000 µm/s to the starting line of the coating (0.5 mm from the top edge of the substrate) as shown in **Figure 3.11**b, and then immediately moved toward the ending line at a coating speed of 100 µm/s (**Figure 3.11**c). During the 'backward' movement toward the starting position the OSC film is formed only on the lyophobic areas. This is due to pattern design (described below). The round-trip motion effectively removes the pBTTT-C16 particles which might be generated in the solution bottle and/or pipette from the film formation area.

Since the target application of this study is OFETs, the characterization was performed after the fabrication of the OFET array, which will be discussed in **Chapter 4**. The pBTTT-C16 film was annealed at 150°C for 15 min in a nitrogen atmosphere.
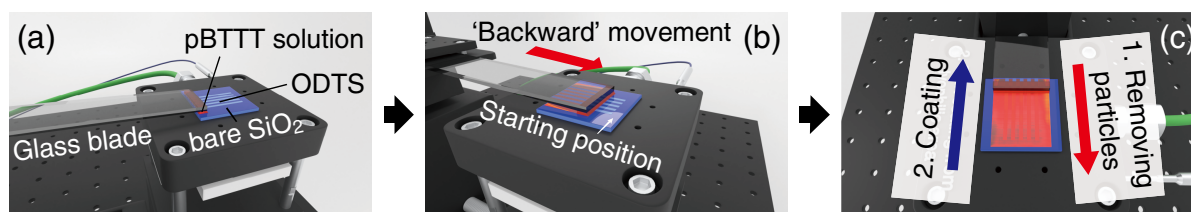
Figure 3.11   Computer-generated images of the *self-assisted flow-coating* process (a): before coating is started, (b): during the backward movement towards the starting position, and (c): after the coating is completed. During the backward motion in (b), the film is not formed on the lyophobic areas.

a) AFM images

The morphology of the pBTTT-C16 film was observed by atomic force microscope (AFM: HITACHI AFM 5100N and AFM5000II). **Figure 3.12**a and **Figure 3.12**b are AFM images (2×2 µm^2 and 5×5 µm^2, respectively) of the pBTTT-C16 active layer of the OFET array fabricated by SAF-coating. The active layer means the pBTTT-C16 film formed in the lyophobic (highly hydrophobic) surface area. The terrace structure with clear steps was observed as expected because the film was annealed at above the smectic phase transition temperature (**Figure 2.9**b, see p.13) during the fabrication process of OFETs. The line profile along the broken line in **Figure 3.12**a is shown in **Figure 3.12**c. The terrace step height was found to be 2.2 nm. This step height is coincident with the interlayer distance (2.2 nm) of the terrace-phase pBTTT-C16 film along the surface normal, which was reported by Umeda et al.[3.11] From this observation, the formation of terrace-phase pBTTT-C16 thin film on the lyophobic surfaces after annealing at 150°C for 15 min was confirmed.
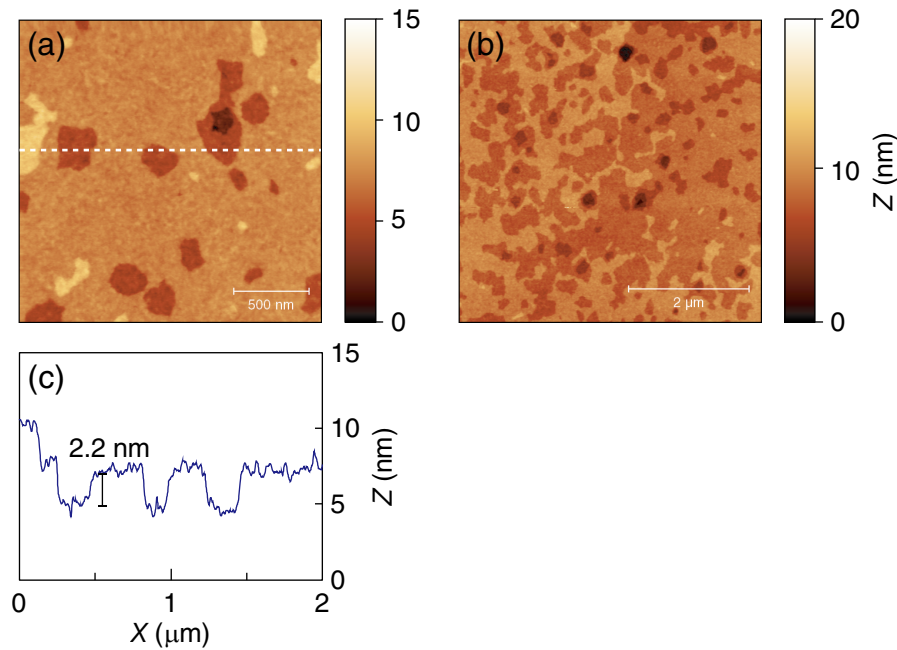
Figure 3.12 (a, b): AFM images (2 × 2 μm^2 and 5 × 5 μm^2, respectively) of the pBTTT-C16 active layer of the OFET array fabricated by *self-assisted flow-coating*. The active layer was annealed at 150°C for 15 min in a nitrogen atmosphere. (c): Line profile along the broken line in (a).

b) Film thickness

The thickness of the self-assisted flow-coated pBTTT-C16 film was measured using a stylus type step profiler (Kosaka ET200). The measurements were performed along 10 lines which are indicated by white broken lines in **Figure 3.13**a. **Figure 3.13**b shows the line profile along the blue segment in **Figure 3.13**a. The dents are the lines on which pBTTT-C16 was removed by a probe (W needle) for OFET isolation (explained in **Chapter 4**). The film thickness of the whole OFET array area (~1 cm^2) was evaluated and was found to be
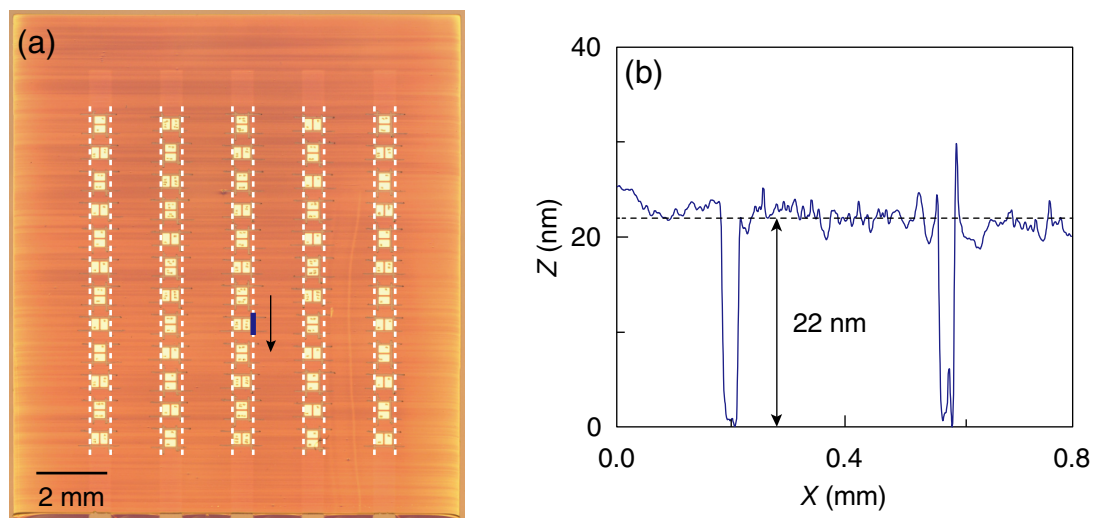
Figure 3.13 (a): Optical microscope image of the pBTTT-C16 film (with array of source/drain electrodes), and (b): profile along the blue segment in the direction of the black arrow in (a). The broken lines in (a) indicate the lines along which the profiles were measured.

30

22.6 ± 1.8 nm. This result indicates that the thickness was very uniform considering the molecular step height of pBTTT-C16 (~2.2 nm).[3.11]

c) Polarized optical microscope images

The birefringence of the pBTTT-C16 film was examined by polarizing optical microscope (POM) observation (OLYMPUS BX51). In POM observation in the reflection geometry of crossed Nicols, the oscillations between bright and extinct images were observed four times in 90° increments during rotation over a range of 360°, which indicated that the film was anisotropic. The extinct images appeared when the flow-coating direction was parallel to the polarization axis of the polarizer (P) or analyzer (A) as shown in **Figure 3.14**a. The bright image appeared when the substrate was rotated by 45° from the extinction angle (**Figure 3.14**b). These results show that the pBTTT-C16 backbones in the flow-coated film align on average parallel or perpendicular to the flow-coating direction. The composite POM images (**Figure 3.14**c and **Figure 3.14**d) of the whole OFET array show that the average alignment direction of pBTTT backbone stays nearly constant for the whole film. Since the average alignment direction cannot be determined from the POM observation alone, it was determined from the polarization dependence of the Raman spectra of the pBTTT-C16 film.
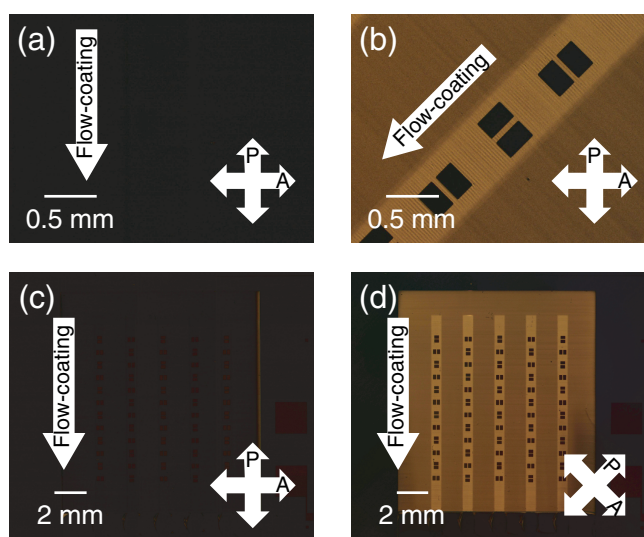
Figure 3.14   (a, c): Extinct and (b, d): bright POM images of the pBTTT-C16 film fabricated by *self-assisted flow-coating* that were observed in the reflection geometry of crossed Nicols, where (c) and (d) are composite images of the whole coated film. The electrodes are already formed on the film. The flow-coating direction as well as the polarization axes of the polarizer (P) and analyzer (A) are indicated by the arrows.

d) Polarized Raman spectra

In order to determine the in-plane molecular orientation of the pBTTT-C16 film fabricated by SAF-coating, the polarized Raman spectra of the pBTTT-C16 active layer of the OFET array was measured. The measurements were performed using a micro Raman spectrometer system (Lambda Vision MicroRAM-300). The focal length of the spectrometer was 300 mm and the Raman scattered light was dispersed with 1800 grooves/mm grating. The Raman spectra were recorded with an accumulation time of 25 seconds in a back-scattering geometry. An objective lens of a magnification of 20 with a numerical aperture of 0.4 was used for focusing the excitation laser light of 532 nm wavelength, and for collecting Raman scattered light. The power

of the laser light at the sample surface was 12 μW. In this measurement, the Raman scattered light polarized parallel to the polarization direction of the excitation light was analyzed. The Raman measurement was performed for parallel (//) and perpendicular (⊥) orientations of the flow-coating direction against the polarization direction of excitation light. The measurement was performed for several points on the pBTTT-C16 film in the lyophobic areas. **Figure 3.15** shows the polarized Raman spectra obtained from one of the measurements. Three strong bands were observed at 1389, 1413, and 1487 cm^{-1}. The 1389 and 1487 cm^{-1} bands are assigned to the C-C and C=C stretching vibrations of the thiophene ring, and the 1413 cm^{-1} band is assigned to the stretching vibration of the thienothiophene ring.[3.13] These three bands showed the same polarization dependence ($I_{//}$ / $I_{\perp}$ = 1.08 ± 0.02) which indicates that the pBTTT-C16 backbone structures were aligned on average in the flow-coating direction.
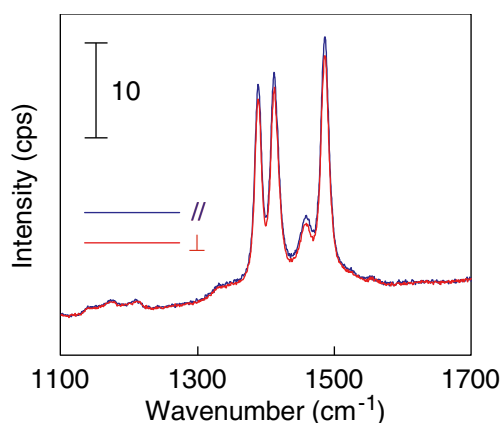
Figure 3.15   Polarized Raman spectra of the flow-coated pBTTT-C16 film on the lyophobic substrate surface region.

3.5   Spin-coating on highly lyophobic surfaces

It was found that the surface patterning technique is also useful for uniform OSC film formation on hydrophobic surfaces by spin-coating. Although the pBTTT-C16 film could not be formed on large lyophobic areas by spin-coating as shown in **Figure 3.16**a, the existence of lyophilic areas regularly scattered over the lyophobic substrate was effective for thin-film formation.[3.2] This is because the presence of hydrophilic areas in the hydrophobic surface helps to form a stable thin layer of organic solution during spin-coating. The ~38 nm-thick pBTTT-C16 films were formed by spin-coating from 0.7 wt.% solution of pBTTT-C16 in o-DCB. Prior to spin-coating, the substrate and a glass pipet were heated on hot plates to 110°C and 120°C, respectively, and the pBTTT-C16 solution was heated on a hot plate set to 110°C. The heated substrate was fixed on a Teflon sample holder of a spin-coater (Mikasa), immediately covered with hot pBTTT-C16 solution using the heated pipet, and then it was spun-coated at 1000 rpm for 180 s. Next, the spin-coated film was dried on a hot plate at 90°C for 10 min. This spin-coating process was carried out in air. Finally, the film was annealed at 150°C for 15 min in a nitrogen atmosphere to obtain a terrace-phase pBTTT-C16 film. The resulting pBTTT-C16 film is shown in **Figure 3.16**b together with an effective surface pattern.

Figure 3.16 Optical microscope images (upper) of the pBTTT-C16 films formed on SiO$_2$ surfaces with different lyophobic-lyophilic patterns (lower) by spin-coating. (a): Large solid lyophobic pattern and (b): 0.7 mm width lyophobic line and 1.3 mm width lyophilic space pattern. The black and white areas correspond to lyophobic (ODTS-covered) and lyophilic (bare) surfaces, respectively.

3.6   Summary

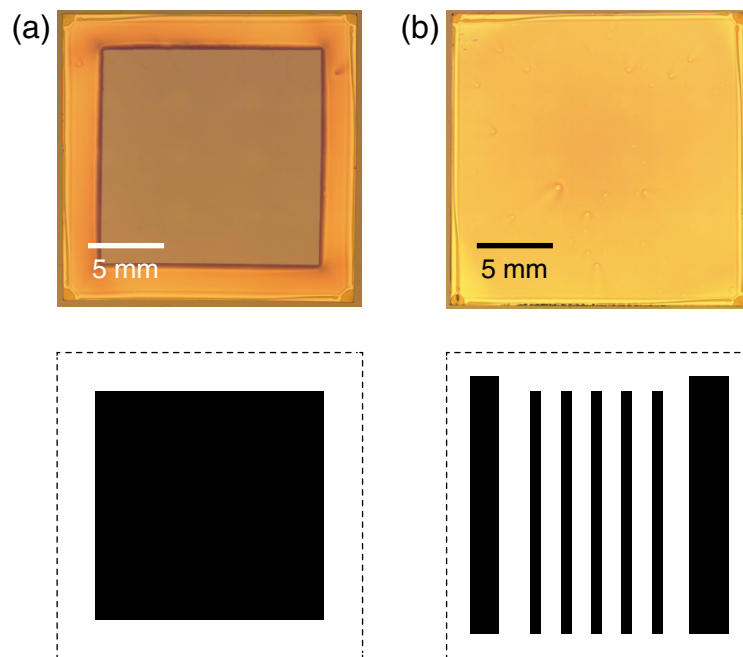The pBTTT-C16 thin film formation on a highly hydrophobic (lyophobic) substrate surface was achieved by the *self-assisted flow-coating* (SAF-coating) method developed in this study. In this method, specially designed lyophobic/lyophilic patterns play an important role in the pBTTT-C16 thin film formation. The useful pattern was a lyophobic/lyophilic line-and-space pattern connected to the top lyophilic rectangular region. The pattern was prepared by exposing ODTS SAM-modified gate dielectric surface to VUV light of 172 nm wavelength through a photomask. The pBTTT-C16 film was formed on both lyophilic and lyophobic areas by starting the flow-coating from the top rectangular region. The film formation mechanism was understood by conducting a simple surface energy calculation. The film formation on the lyophobic surface areas was possible by pinning the contact line to the film growth front with the help of the own formed (forming) film. It was also found that the proposed surface patterning technique was effective for film formation on highly hydrophobic surfaces by spin-coating although the film formation mechanism might be different. In the case of spin-coating, the regularly scattered placement of lyophilic areas over the lyophobic substrate was beneficial.

The SAF-coated pBTTT-C16 film was characterized using AFM, POM, and polarized Raman spectroscopy after the film was annealed at 150°C for 15 minutes in nitrogen. The AFM images confirmed the formation of terrace phase pBTTT-C16 with 2.2 nm molecular steps. The POM images showed the anisotropy of flow-coated pBTTT-C16 film and suggested that pBTTT-C16 backbone was aligned parallel or perpendicular to the flow-coating direction. From the polarization dependence of the Raman spectra, the pBTTT-C16 backbone was found to be aligned on average parallel to the flow-coating direction. The thickness of the flow-coated film was measured on the area of 1 cm^2 scale and was confirmed to be very uniform (22.6 ± 1.8 nm). The electrical properties of the film evaluated by fabricating OFET arrays and measuring their device properties are discussed in **Chapter 4**.

References

[3.1] T. Umeda, D. Kumaki, and S. Tokito. "Surface-Energy-Dependent Field-Effect Mobilities up to 1 cm^2 /V s for Polymer Thin-Film Transistor." *J. Appl. Phys.* **2009**, 105, 024516.

[3.2] K. Bulgarevich, K. Sakamoto, T. Minari, T. Yasuda, and K. Miki. "Spatially Uniform Thin-Film Formation of Polymeric Organic Semiconductors on Lyophobic Gate Insulator Surfaces by Self-Assisted Flow-Coating." *ACS Appl. Mater. Interfaces* **2017**, 9, 6237.

[3.3] J. Li, Y. Zhao, H. S. Tan, Y. Guo, C.-A. Di. G. Yu, Y. Liu. M. Lin. S. H. Lim, Y. Zhou, H. Su, and B. S. Ong. "A Stable Solution-Processed Polymer Semiconductor with Record High-Mobility for Printed Transistors." *Sci. Rep.* **2012**, 2, 754.

[3.4] K. Sakamoto, R. Arafune, N. Ito, S. Ushioda, Y. Suzuki, S. and Morokawa. "Molecular Orientation of Rubbed and Unrubbed Polyimide Films Determined by Polarized Infrared Absorption." *Jpn. J. Appl. Phys.* **1994**, 33, L1323.

[3.5] T. Minari, C. Liu, M. Kano, and K. Tsukagoshi. "Controlled Self-Assembly of Organic Semiconductors for Solution-Based Fabrication of Organic Field-Effect Transistors." *Adv. Mater*. **2012**, 24, 299.

[3.6] H. Sugimura and N. Nakagiri. "Force Microscopy Imaging of Photopatterned Organosilane Monolayers: Application to Probe Alignment in AFM Patterning Following Photolithography." *Appl. Phys. A* **1998**, 66, S427.

[3.7] H. Sugimura, K. Ushiyama, A. Hozumi and O. Takai. "Micropatterning of Alkyl- and Fluoroalkylsilane Self-Assembled Monolayers Using Vacuum Ultraviolet Light." *Langmuir* **2000**, 16, 885.

[3.8] X. Liu, M. Kanehara, C. Liu, K. Sakamoto, T. Yasuda, J. Takeya, and T. Minari. "Spontaneous Patterning of High-Resolution Electronics via Parallel Vacuum Ultraviolet." *Adv. Mater.* **2016**, 28, 6568.

[3.9] T. Minari, Y. Kanehara, C. Liu, K. Sakamoto, T. Yasuda, A. Yaguchi, S. Tsukada, K. Kashizaki, and M. Kanehara. "Room-Temperature Printing of Organic Thin-Film Transistors with π-Junction Gold Nanoparticles." *Adv. Funct. Mater.* **2014**, 24, 4886.

[3.10] K. Sakamoto, J. Ueno, K. Bulgarevich, and K. Miki. "Anisotropic Charge Transport and Contact Resistance of 6,13-bis(triisopropylsilylethynyl) Pentacene Field-Effect Transistors Fabricated by a Modified Flow-Coating Method." *Appl. Phys. Lett*. **2012**, 100, 123301.

[3.11] T. Umeda, S. Tokito, and D. Kumaki. "High-Mobility and Air-Stable Organic Thin-Film Transistors with Highly Ordered Semiconducting Polymer Films." *J. Appl. Phys.* **2007**, 101, 054517.

[3.12] X. GU, L. Shaw, K. Gu, M. F. Toney and Z. Bao. "The Meniscus-Guided Deposition of Semiconducting Polymers." *Nature Commun.* **2018**, 9, 534.

[3.13] J. Gao, A. K. Thomas, R. Johnson, H. Guo, and J. K. Grey. "Spatially Resolving Ordered and Disordered Conformers and Photocurrent Generation in Intercalated Conjugated Polymer/Fullerene Blend Solar Cells." *Chem. Mater.* **2014**, 26, 4395.

Chapter 4　OFET array fabricated by SAF-coating

Since the target application of the present study is OFETs, the spatial uniformity of the pBTTT-C16 film formed in **Chapter 3** was examined from the aspect of OFET properties. The DDV of OFET properties is closely related to the spatial uniformity of the active layer. The higher spatial uniformity of the active layer leads to the smaller DDV. It was shown in the previous chapter that for the SAF-coated film, the pBTTT-C16 backbone structures align on average along the flow-coating direction. Thus, to evaluate the spatial uniformity and charge transport anisotropy, a BG/TC type OFET array was designed to produce two types of OFETs the channel current directions of which were aligned parallel or perpendicular to the coating direction. OFETs were fabricated on the lyophobic (highly hydrophobic) gate insulator surface over an area of ~1 cm^2.

4.1　Fabrication of OFET arrays

The active layer was obtained by forming the pBTTT-C16 film (~23 nm-thick) on patterned ODTS SAM-treated substrate (SiO_2/n$^+$-Si) surface by SAF-coating method, and annealing the film at LC phase temperature, as explained in **Chapter 3**. For comparison, the pBTTT-C16 active layer was also formed by spin-coating. The surface area on which the high performance OFETs can be fabricated is limited to the lyophobic areas (five 0.7×17.5 mm^2 stripes in this experiment). Considering the practical applications of the patterning method, the rest of the area potentially can be used for circuit wiring and fabrication of passive components.

The source and drain electrodes for BG/TC type OFETs were formed using resistive heating vapor deposition through a shadow nickel mask in vacuum (< 10^{-3} Pa), as illustrated in **Figure 4.1**a. The shadow mask pattern used to form the S/D electrode array is also shown in **Figure 4.1**b. Since the SAF-coating is a unidirectional process,[4.1],[4.2] the array was designed to produce 30 OFETs whose channel current is parallel to the coating direction (*parallel* OFETs) and 30 *perpendicular* ones. The channel length and width were 50 and 300 μm, respectively. First, 25 nm-thick layer of MoO$_x$ was deposited at deposition rates of 0.1 Å/s (0 nm ~ 2.5 nm) and 0.2 Å/s (2.5 nm ~ 25 nm), and then sequentially 63 nm-thick layer of Au was formed at 0.1 Å/s (0 nm ~ 1.5 nm), 0.2 Å/s (1.5 nm ~ 7.5 nm), and 0.3 Å/s (7.5 nm ~ 63 nm). The thickness of the formed electrodes was evaluated with a stylus type step profiler (Kosaka ET200).
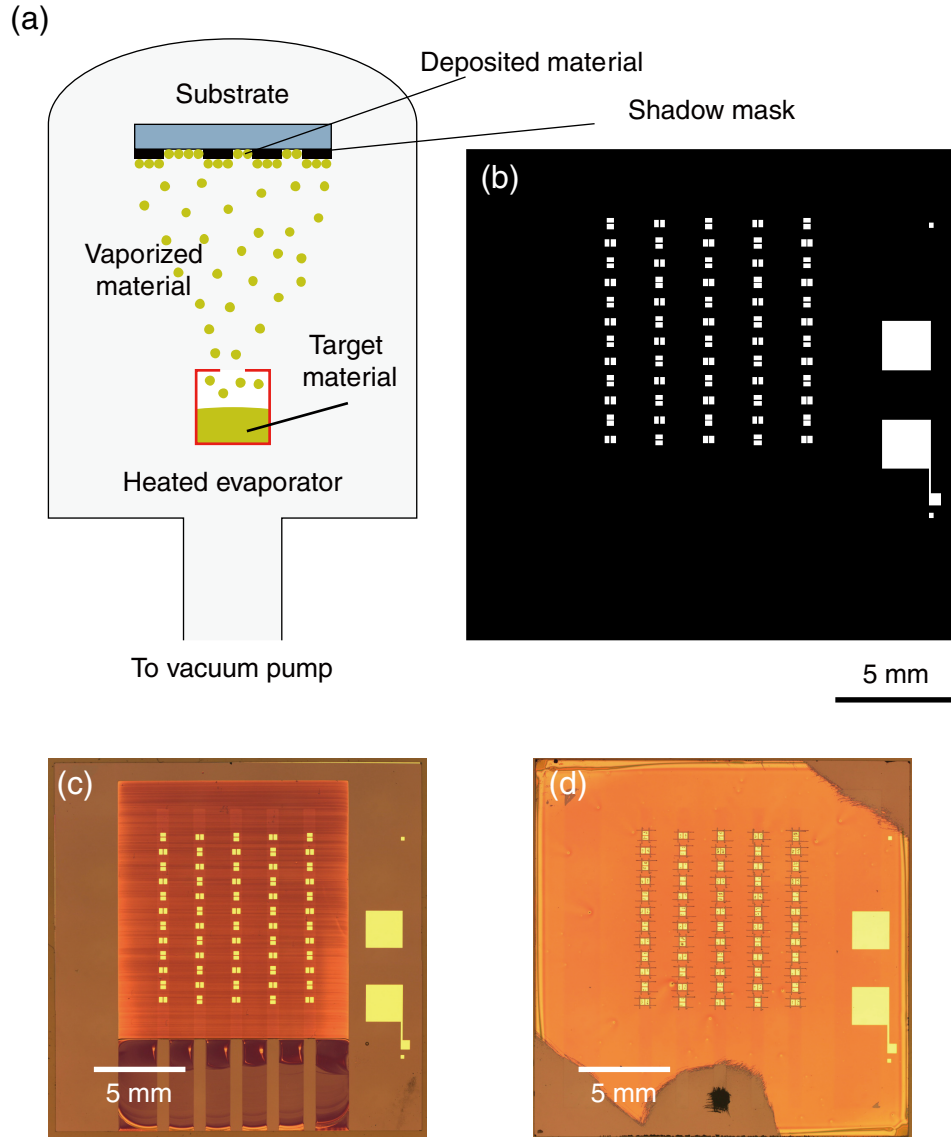
Figure 4.1 (a): Schematic illustration of the resistive heating vapor deposition, and (b): the shadow mask pattern used for OFET array formation. The resulting OFET array with pBTTT-C16 active layers fabricated by (c): SAF-coating and (d): spin-coating. (d) was taken after all the electrical measurements.

4.2 Evaluation of OFETs

The DDV of the OFET array and the charge transport anisotropy of pBTTT-C16 film were evaluated by measuring device properties of all the OFETs in the array by using a vacuum probe station (VIC International, Inc. VMP-100) and a semiconductor parameter analyzer (Keithley 4200-SCS). These measurements were performed in vacuum ($< 10^{-4}$ Pa) at room temperature in the dark after isolating each OFET from the others by removing the surrounding pBTTT-C16 film with a probe (W needle). The circuit diagram for measuring the *I-V* characteristics of the OFETs is shown in **Figure 4.2**.
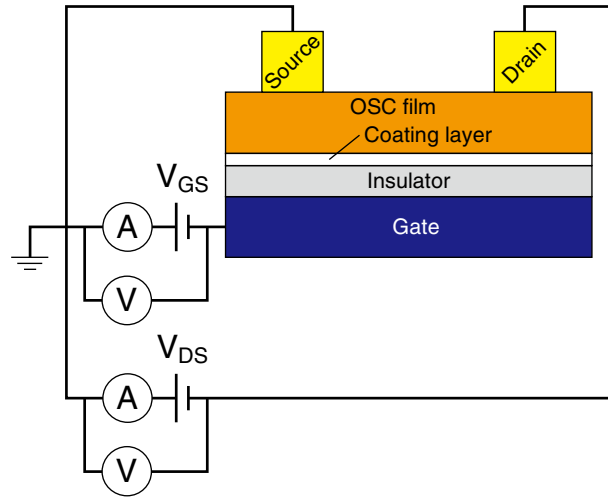
Figure 4.2   Electrical scheme for measurements of OFET device characteristics.
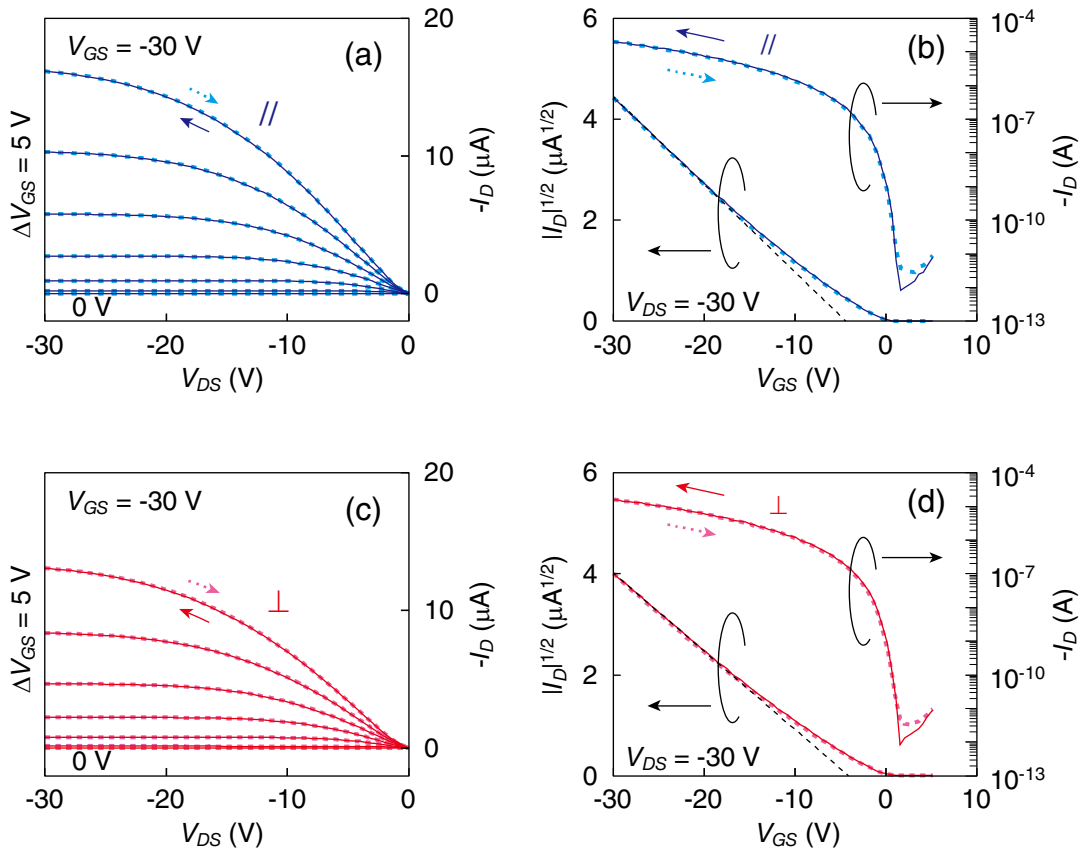
Figure 4.3   (a, c): Output, and (b, d): transfer characteristics of (a, b): *parallel*, and (c, d): *perpendicular* OFETs. The "*parallel*" and "*perpendicular*" specify the channel current directions with respect to the flow-coating direction. The data in forward and reverse sweeps are shown by the solid and broken curves, respectively. The relationship between $\sqrt{I_d}$ and V_{GS} is also shown in (b) and (d). The broken straight lines in (b) and (d) were used for calculating the carrier mobility and threshold voltage.

Figure 4.3a and **Figure 4.3**b show the output and transfer curves, respectively, of one of the *parallel* OFETs. The output curve shows drain current (I_D) as a function of drain voltage (V_{DS}) keeping gate voltage (V_{GS}) fixed for each curve. For the output curve, V_{GS} was varied from 0 to -30 V at 5 V steps, and for each V_{GS}, V_{DS} was varied from +1 to -30 V and back to +1 V at 1 V steps. The transfer curve shows I_D, and $\sqrt{I_D}$ as a function of I_{GS}. Here, V_{GS} was varied from +5 to -30 V and back to +5 V at 0.5 V steps. The threshold voltage (V_{th}) and carrier mobility (μ) were calculated from the slope of the transfer curve using **Equation 2.9** and **Equation 2.11**, respectively (see p.7). The typical output and transfer characteristics of one of the *perpendicular* OFETs are shown in **Figure 4.3**c and **Figure 4.3**d, respectively. For all the OFETs in the array, the transfer curve was measured at least six times sequentially (the transfer curve of the 6th measurement is shown in **Figure 4.3**b and **Figure 4.3**d), and the output curve was measured for 12 OFETs in the middle row of the array. Although the device properties of OFETs fabricated in the hydrophilic areas were not evaluated in this experiment, the characteristics of such OFETs are presented in **Chapter 5** (see p.53). Such OFETs show much lower carrier mobility compared to those fabricated in the hydrophobic areas.

Figure 4.4 shows the histograms of μ, on-state current (I_D^{on}), V_{th}, and subthreshold swing (SS) of the OFET array. The subthreshold swing is defined as the change of V_{GS} in a subthreshold region needed to increase I_D by a factor of 10. The filled and open bars show the results for *parallel* and *perpendicular* OFETs, respectively. The average values (A_v), standard deviations (σ), and relative standard deviations (σ / A_v) are summarized in **Table 4.1**. The field-effect hole mobilities were $\mu_{//} = 0.273 \pm 0.007$ cm^2·V^{-1}·s^{-1} and $\mu_{\perp} = 0.221 \pm 0.006$ cm^2·V^{-1}·s^{-1} for *parallel* and *perpendicular* OFETs, respectively. The in-plane anisotropy ($\mu_{//} / \mu_{\perp}$) was

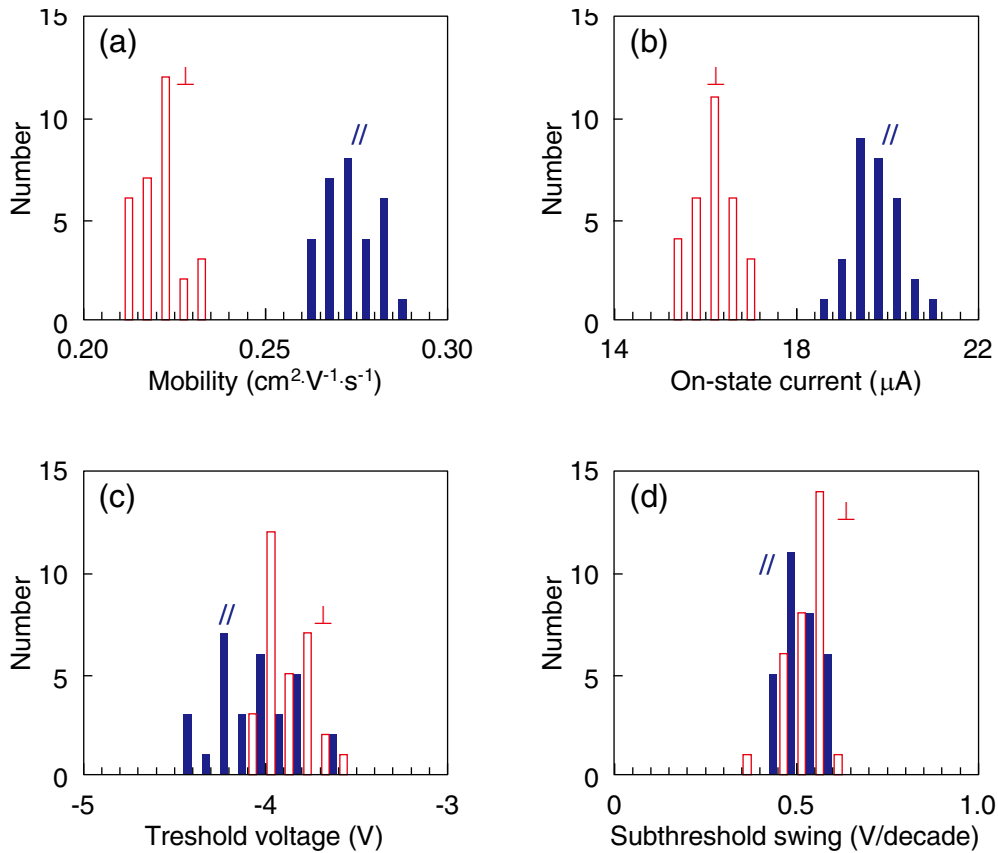**Figure 4.4**   Histograms of (a): field-effect hole mobility, (b): on-state current, (c): threshold voltage, and (d): subthreshold swing of the OFET array fabricated by *self-assisted flow-coating*. The filled and open bars show the results for the *parallel* and *perpendicular* OFETs, respectively. The bin width of each histogram is: a) 0.005 cm^2·V^{-1}·s^{-1}, b) 0.4 µA, c) 0.1 V, and d) 0.05 V/decade.

1.24. Even though the difference between $\mu_{//}$ and $\mu_{\perp}$ was relatively small ($\mu_{//}$ - $\mu_{\perp}$= 0.052 cm^2·V^{-1}·s^{-1}), the distribution of $\mu_{//}$ was completely separated from $\mu_{\perp}$ as shown in **Figure 4.4**a. This is because the DDV of both OFET sets was very small (< 3%). The complete separation clearly showed that the charge transport in the flow-coated pBTTT-C16 film was anisotropic.

As shown in Figure 4.8b, the DDV of I_D^{on} was also very small and less than 3% for both *parallel* and *perpendicular* OFET sets. This is attributed to the narrow distribution of V_{th} (**Figure 4.4**c). Moreover, the variation of *SS* was also small as shown in **Figure 4.4**d. Since the narrow distribution was achieved for these four quantities, the transfer curves of the OFETs should be nearly identical. To clearly demonstrate that, the overlaid transfer curves (6th measurement) of all the *parallel* and *perpendicular* OFETs of the array are shown in **Figure 4.5**a and **Figure 4.5**b, respectively. In these figures the forward (V_{GS}: from +5 V to -30 V) and the backward (V_{GS}: from -30 V to +5 V) sweeps are both plotted. It can be clearly seen that the transfer curves showed no hysteresis and were almost identical within both *parallel* and *perpendicular* OFET sets. From these results, it was confirmed that spatial uniformity of the flow-coated pBTTT-C16 film was very high.[4.3]

Table 4.1 Electrical properties (μ, I_D^{on}, V_{th} and *SS*) of the *parallel*, *perpendicular*, and *isotropic* (see below) pBTTT-C16 OFETs measured in the saturation regime.

	Parallel OFETs			*Perpendicular* OFETs			*Isotropic* OFETs		
	A_v	σ	σ/A_v	A_v	σ	σ/A_v	A_v	σ	σ/A_v
μ [cm^2·V^{-1}·s^{-1}]	0.273	0.007	2.4%	0.221	0.006	2.6%	0.262	0.006	2.4%
I_D^{on} [μA]	19.7	0.5	2.7%	16.2	0.4	2.7%	22.0	0.6	2.9%
V_{th} [V]	-4.1	0.2		-3.9	0.1		-4.7	0.3	
SS [V per decade]	0.50	0.05		0.53	0.06		0.44	0.07	
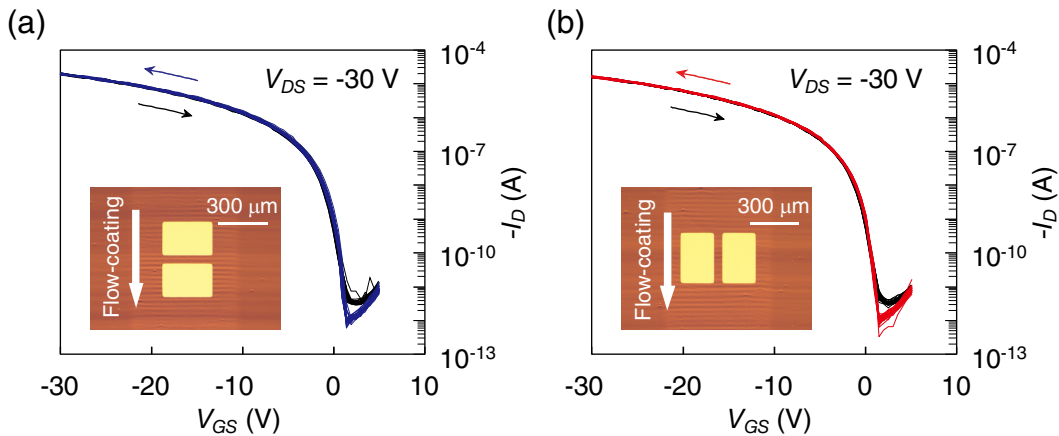
Figure 4.5 Overlaid transfer curves of (a): 30 *parallel* and (b): 30 *perpendicular* OFETs. Both transfer curves in the forward (colored) and reverse (black) sweeps are plotted. The inset in each figure shows an optical microscope image of one of the *parallel* or *perpendicular* OFETs.

The observed mobility of SAF-coated OFETs was slightly lower than that reported by Umeda et al.,[4.4] even though the OFET structures were similar. To check the causes, the device properties of 30 spin-coated OFETs fabricated on the lyophobic gate dielectric surface were evaluated. The spin-coated BTTT-C16 film

was formed using a different lyophobic/lyophilic pattern shown in **Figure 3.16**b. The typical output and transfer characteristics of the spin-coated OFETs are shown in **Figure 4.6**. The result of the whole OFET array evaluation is also listed in **Table 4.1** as "*isotropic*" OFETs. The mobility of the spin-coated OFETs was 0.262 $\pm$ 0.006 cm^2·V^{-1}·s^{-1}, which was almost the same as, but a little bit smaller than, that of the *parallel* flow-coated OFETs. This result shows that the quality of flow-coated films is comparable to that of the spin-coated films. Therefore, the relatively smaller mobility is probably related to the quality variation of commercially available polymer reagents and/or due to the inevitable air exposure in the OFET fabrication process conducted in this study.
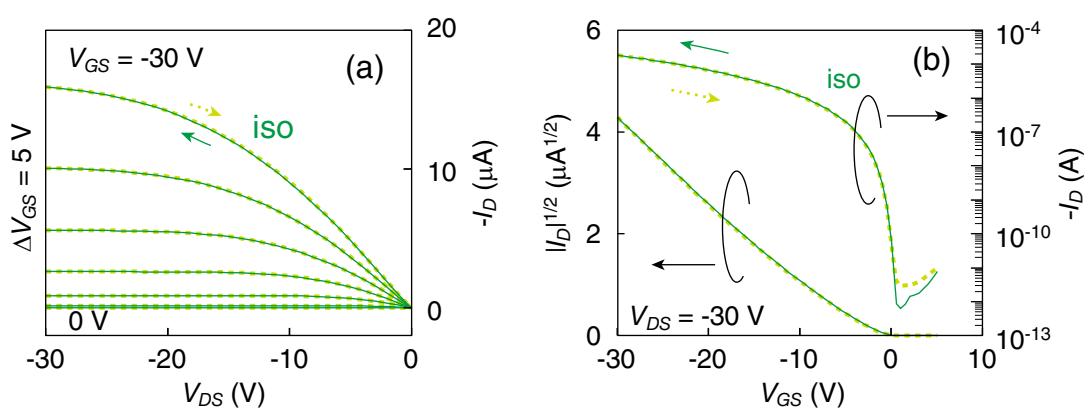
Figure 4.6   Typical (a): output and (b): transfer characteristics of one of the "*isotropic*" spin-coated OFETs.

4.3   Summary

The BG/TC type OFET array consisting of 30 *parallel* and 30 *perpendicular* OFETs (direction of channel current against the coating direction) was fabricated using a pBTTT-C16 film as the active layer. The pBTTT-C16 film was formed on the lyophobic surface by using a newly developed *self-assisted flow-coating* (SAF-coating) method which was shown in the previous chapter. The device properties of all the OFETs in the array were measured, and the DDV was evaluated for each of the *parallel* and *perpendicular* OFET sets. The average field-effect hole mobilities ($\pm$ standard deviation) were 0.273 $\pm$ 0.007 cm^2·V^{-1}·s^{-1} and 0.221 $\pm$ 0.006 cm^2·V^{-1}·s^{-1} for *parallel* and *perpendicular* OFETs, respectively. The DDV of the mobility and on-state current were both less than 3% for each OFET set. Moreover, the very narrow distribution was obtained for the threshold voltage and subthreshold swing. As the result, the transfer curves of all the OFETs were almost identical within each *parallel* and *perpendicular* OFET set. These results clearly showed that the DDV of the whole electrical properties was extremely small confirming the very high spatial uniformity of SAF-coated pBTTT-C16 film. The device properties of the OFETs fabricated by SAF-coating were compared with *isotropic* spin-coated ones. The negligible difference in carrier mobility between *parallel* and *isotropic* (0.262 $\pm$ 0.006 cm^2·V^{-1}·s^{-1}) OFETs indicated that the quality of the SAF-coated pBTTT film was comparable to the spin-coated one. Therefore, it is concluded that SAF-coating is a promising scalable method for fabricating OFET arrays with high performance and small DDV.

References

[4.1] K. Sakamoto, J. Ueno, K. Bulgarevich, and K. Miki. "Anisotropic Charge Transport and Contact Resistance of 6,13-bis(triisopropylsilylethynyl) Pentacene Field-Effect Transistors Fabricated by a Modified Flow-Coating Method." *Appl. Phys. Lett*. **2012**, 100, 123301.

[4.2] K. Sakamoto, K. Bulgarevich, and K. Miki. "Small Device-to-Device Variation of 6,13-bis(triisopropylsilylethynyl) Pentacene Field-Effect Transistor Arrays Fabricated by a Flow-Coating Method." *Jpn. J. Appl. Phys.* **2014**, 53, 02BE01.

[4.3] K. Bulgarevich, K. Sakamoto, T. Minari, T. Yasuda, and K. Miki. "Spatially Uniform Thin-Film Formation of Polymeric Organic Semiconductors on Lyophobic Gate Insulator Surfaces by Self-Assisted Flow-Coating." *ACS Appl. Mater. Interfaces* **2017**, 9, 6237.

[4.4] T. Umeda, D. Kumaki, and S. Tokito. "Surface-Energy-Dependent Field-Effect Mobilities up to 1 cm^2/Vs for Polymer Thin-Film Transistor." *J. Appl. Phys.* **2009**, 105, 024516.

Chapter 5 Alignment-induced mobility enhancement by hydrophobic nano-grooved gate dielectric surfaces

In this chapter, alignment-induced mobility enhancement for the polymer-based OFETs realized with very small DDV is reported.[5.1] Molecularly highly-aligned and uniform crystalline films of small-molecule semiconductors can be obtained by solution coating processes involving a directional movement of the contact line.[5.2] However, for polymeric semiconductors possessing inherent high charge carrier mobility, it is difficult to realize high degree of alignment by using only a solution coating method. It was shown in **Chapter 4** that SAF-coated pBTTT-C16 film exhibit extremely high uniformity and noticeable anisotropy in charge transport ($\mu_{//}$ / $\mu_{\perp}$ = 1.4). However, improvement of the charge carrier mobility ($\mu_{//}$ = 0.273 cm$^2 \cdot$V$^{-1} \cdot$s^{-1}) compared to *isotropic* spin coated OFETs (μ_{iso} = 0.262 cm$^2 \cdot$V$^{-1} \cdot$s^{-1}) could not be achieved.[5.3] This is probably because the alignment degree of polymer backbone structures was insufficient.

It was recently reported that nanostructures on substrate surfaces can guide the molecular arrangement of polymeric semiconductors.[5.4] In previous works, the nano-grooved surfaces were used to align PCDTPT, which is a well-designed D-A copolymer. An order of magnitude improvement in field-effect hole mobility was attained by casting the semiconductor solution onto hydrophobic nano-grooved surfaces under very slow solvent evaporation condition, which was realized in a tunnel-like configuration.[5.5] Further mobility enhancement was achieved by combining the capillary action.[5.6] However, in these methods, the long manufacturing time and large DDV coming from the concentration changes caused by slow solvent evaporation are inevitable. Thus, it is still a big challenge to develop a coating method for fabrication of aligned arrays of high-performance polymer-based OFETs with small DDV.

The alignment-induced mobility enhancement that was not obtained by the unidirectional SAF-coating was achieved by using highly hydrophobic nano-grooved surfaces as alignment-inducing surfaces. Here, spin-coating was used and the dewetting of the OSC solution on such a surface was suppressed by producing specially designed surface patterns. The method of producing highly aligned and uniform hydrophobic nano-grooves, the OSC film formation and the resulting film properties, and the characteristics of the fabricated OFETs are discussed.

5.1   Home-made scratching machine

For the purpose of this study, a home-made scratching machine was designed and fabricated. The scratching machine consists of a diamond lapping film which is fixed on a stationary stage and a movable holder that can unidirectionally sweep the sample against the lapping film under set pressure as shown in **Figure 5.1**. It is important to eliminate any vibrations caused by the movement of the holder as such can cause large variation in directions of the nano-grooves. **Figure 5.2**a is an AFM image of the scratched SiO$_2$ surface obtained by using our first scratching machine prototype (**Figure 5.2**b). The obtained nano-grooves were clearly not unidirectional. In the second prototype this problem was solved (the vibrations were reduced) by increasing the thickness of the stage, changing the shape of the rails that guide the holder during the movement
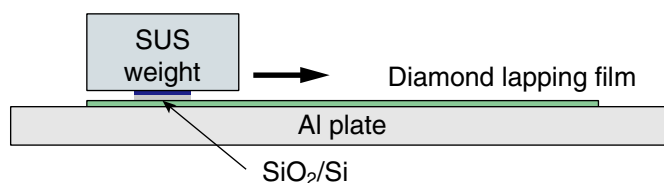

Figure 5.1   Schematic illustration of the scratching machine.

and by more careful design in general. The formation of uniform and unidirectional nanogrooves (**Figure 5.2**c) by the second prototype (**Figure 5.2**d) was confirmed.
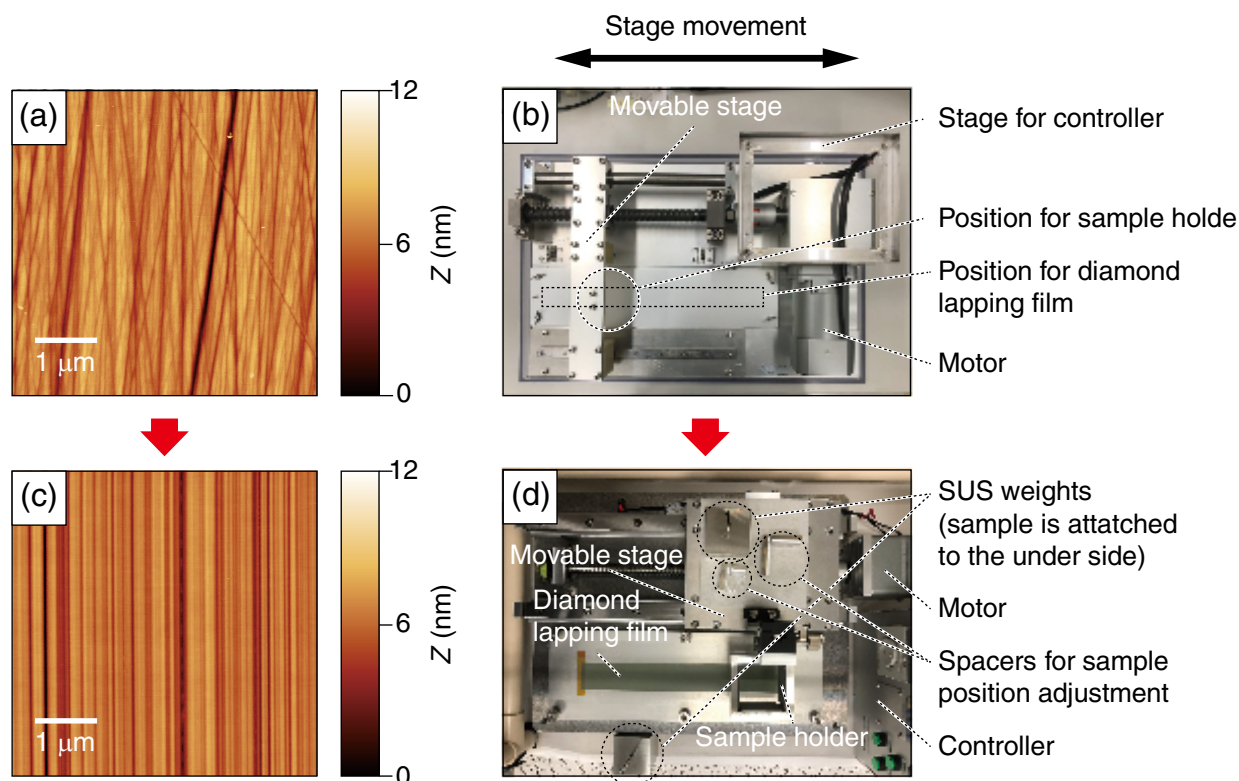
Figure 5.2   (a, c): AFM images of the SiO_2 surfaces that were scratched by using our (b): first and (d): second scratching machines, respectively.

5.2   Fabrication of the OFET arrays

5.2.1 Preparation of highly hydrophobic nano-grooves surfaces

As was described in **Chapter 3**, SiO_2/n^+-Si wafers (SiO_2 thickness: ~100 nm) were used as substrates. The substrates were cleaned by immersion for 10 min three times in a piranha solution, rinsed several times with deionized water. The clean substrates were kept in deionized water and dried with nitrogen gas blow immediately prior to the scratching process.

Highly aligned linear nano-grooves (**Figure 5.2**c) were formed on the cleaned SiO_2 gate dielectric by using a homebuilt scratching machine (**Figure 5.2**d). The SiO_2 surface was scratched under deionized water with diamond lapping film (3M 668X, 100 nm nanoparticle sizes) by moving it on 0.18 m in one direction. The scratching speed and pressure were 2 mm/s and 0.1 kgf/cm^2, respectively. To ensure the spatial uniformity and sufficiently high density of the nano-grooves, the scratching process was repeated 10 times. The substrate was rotated by 180° around the surface normal at every iteration. The total scratching distance was 1.8 m. Then, the substrate was cleaned again by sonication in acetone for 20 min five times followed by the piranha solution treatment described above.

The cleaned SiO_2/n^+-Si substrate with or without nano-grooves was treated with vapor of ODTS (Acros Organics) at 120°C for 3 h, which was performed along the recipe described in **Chapter 3**, except for rubbing. Before proceeding to the next step, it was confirmed that the ODTS-treated surface exhibited a water contact angle of at least 110°.

5.2.2 Active layer formation by spin-coating

The obtained nano-grooved surface exhibited a water contact angle of greater than 110°. On such highly hydrophobic surface, the thin film formation of pBTTT-C16 by spin-coating fails due to its repellant property for organic solvents (lyophobicity). To enable the thin film formation, a suitable hydrophobic/hydrophilic (lyophobic-lyophilic) surface pattern was produced by exposing the highly hydrophobic nano-grooved surface to VUV light through a photomask[5.3] as shown in **Figure 5.3**. After the VUV light treatment and cleaning by sonication in toluene and 2-propanol, the water contact angle in the VUV-light-exposed regions was reduced to 22°.
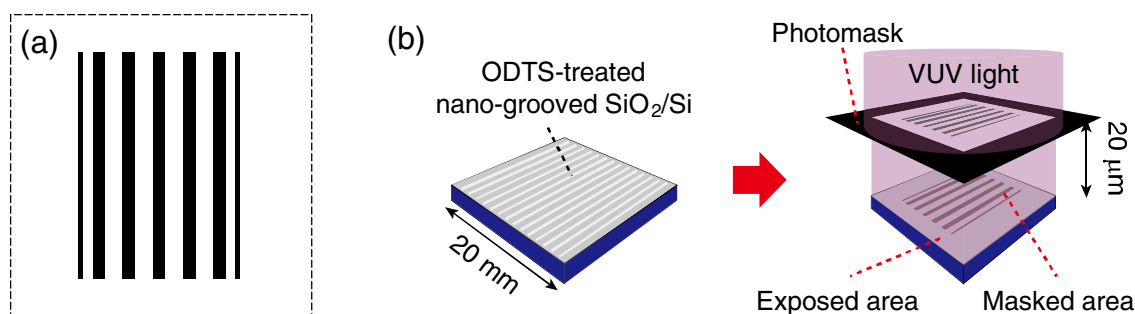

Figure 5.3   (a): Photomask pattern used to form an effective surface pattern for film formation on hydrophobic surfaces and (b): the photo-patterning process.

Then, ~24 nm-thick pBTTT-C16 films was formed by spin-coating from 0.5 wt.% solution of pBTTT-C16 in o-DCB. Prior to spin-coating, the substrate and a glass pipet were heated on hot plates to 110°C and 120°C, respectively, and the pBTTT-C16 solution was heated to 85°C using a hot bath. The heated substrate was fixed on a Teflon sample holder of a spin-coater (Mikasa), immediately covered with hot pBTTT-C16 solution using the heated pipet, and then it was spun-coated at 1000 rpm for 180 s. Next, the spin-coated film was dried on a hot plate at 90°C for 10 min. This spin-coating process was carried out in air. Finally, the film was annealed at 150°C for 15 min in a nitrogen atmosphere to obtain a terrace-phase pBTTT-C16 film.

5.2.3 OFET array fabrication

To fabricate a BG/TC-type OFET array, the S/D electrodes were deposited on the terrace-phase pBTTT-C16 film formed on the SiO_2/n^+-Si substrate by sequential thermal evaporation of MoO_x (25 nm-thick) and Au (63 nm-thick) through a shadow mask in vacuum (base pressure $< 5 \times 10^{-4}$ Pa). The S/D electrodes were placed in the hydrophobic surface regions. The n^+-Si substrate and ODTS-treated SiO_2 layer (~100 nm-thick) served as the common gate electrode and gate dielectric, respectively. The shadow mask produced an array of OFETs with L / W of 50 / 300 μm, in which the channel directions of neighboring OFETs were orthogonal to each other over an area of ~1 cm². For the nano-grooved gate dielectric, an array composed of *parallel* and *perpendicular* OFETs (30 pieces each) was fabricated. For the gate dielectric without nano-grooves, an array composed of 40 OFETs was fabricated. 20 OFETs were fabricated in the hydrophilic surface areas on the same substrate without nano-grooves. The optical microscope images of the OFET arrays with and without nano-grooves are shown in **Figure 5.4**a and **Figure 5.4**b, respectively.
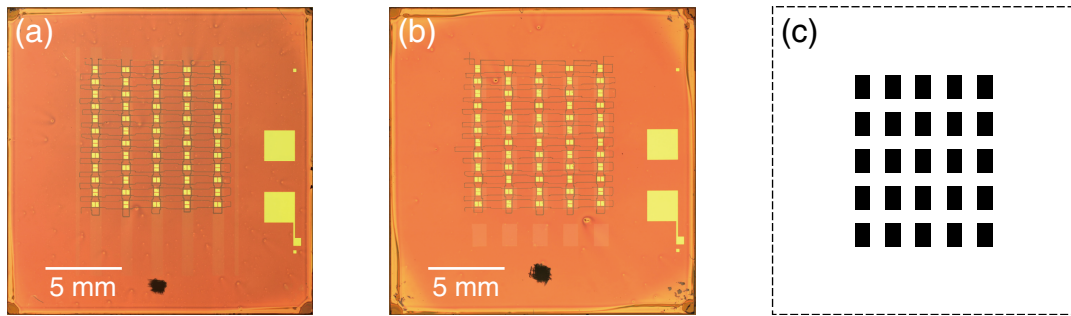
Figure 5.4   Optical microscope images of the pBTTT-C16 OFET arrays formed on SiO₂ surfaces (a): with and (b): without nano-grooves. A different photomask pattern was used for (b), which is shown in (c), and 20 out of 60 OFETs in were formed in the hydrophilic surface areas.

5.3   Results and discussion

5.3.1 Characterization of hydrophobic nano-grooved surfaces

a) AFM images

The formation of uniform, dense, and highly aligned linear nano-grooves was essential to realize the spatially uniform terrace-phase pBTTT-C16 films with a high degree of alignment. To confirm that, the AFM measurements were performed on the scratched SiO₂ surface. There was no substantial difference between AFM images taken in 5 different regions (see **Figure 5.5**a) indicating that spatial uniformity of the scratched surface was high. A typical AFM image of the scratched surface is shown in **Figure 5.5**b together with the height profile along the white broken line. It can be seen that dense nano-grooves were formed with a high degree of alignment parallel to the scratching direction. Mostly, their depths were below 2 nm and limited by 8 nm.
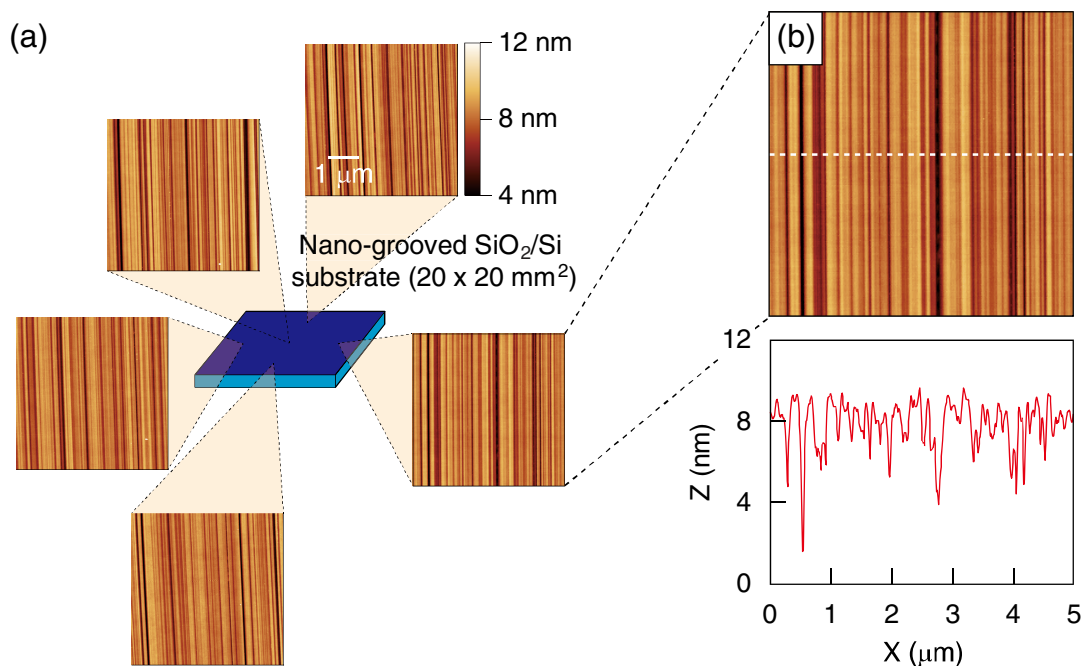
Figure 5.5   (a): AFM images (5 x 5 µm²) of a scratched SiO₂ surface taken at five areas. (b): The profile along the white broken line of one of the images. The color scale is identical for all the images (8 nm).

46

b) Cross-sectional SEM images

The shapes of the nano-grooves were examined with a scanning electron microscope (SEM). The cross-sectional SEM images of the nano-grooved surfaces are shown in **Figure 5.6**. The shapes of nano-grooves were found to be roughly characterized with a radius of curvature of 50 nm, which corresponds to the average size of the diamond particles of the lapping film.
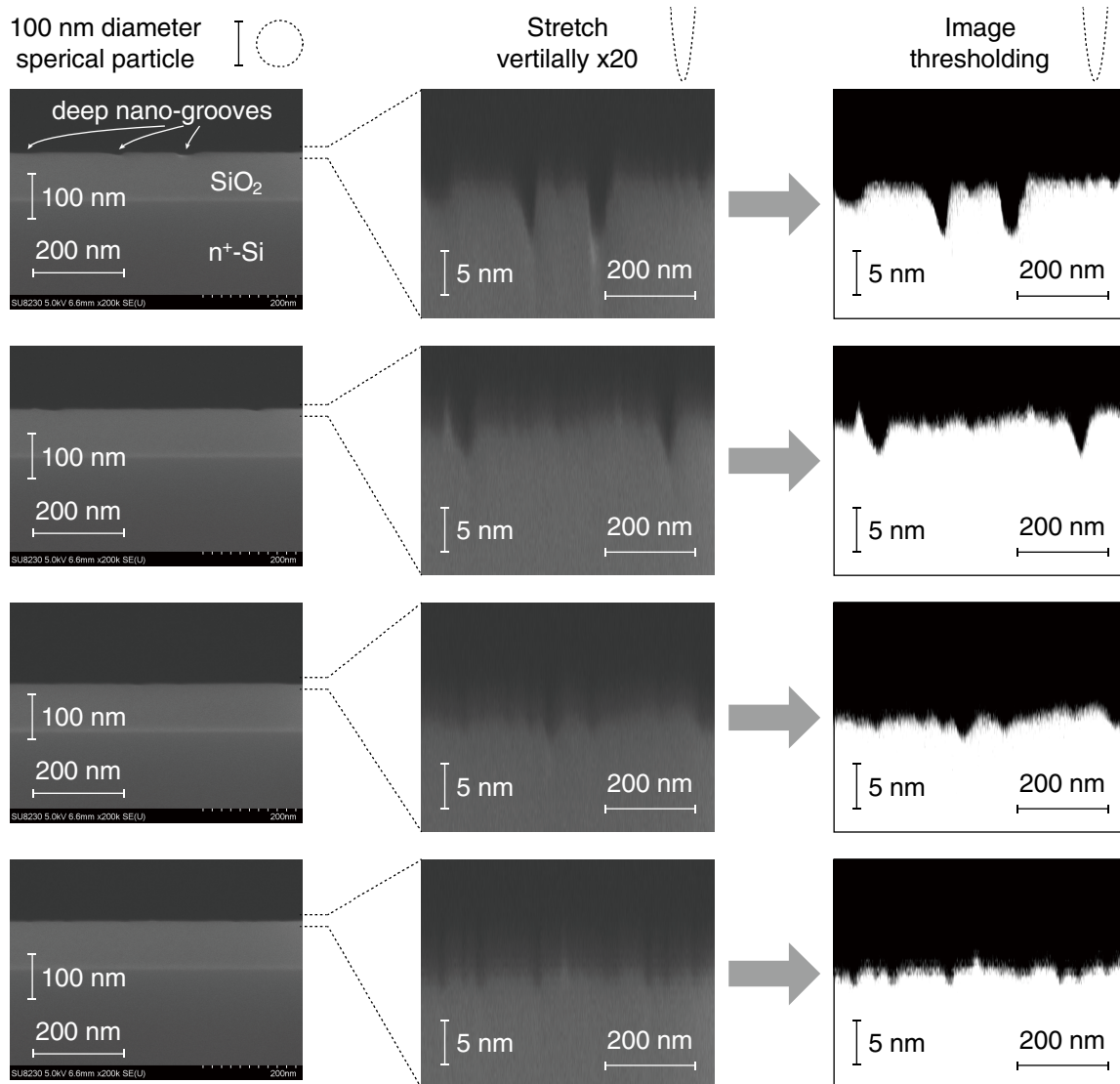
Figure 5.6 Cross-sectional SEM images (200k) of the scratched SiO_2/n^+-Si substrate captured at four areas (top to bottom). Left: as captured, middle: after stretching vertically by a factor of 20 and right: after applying image thresholding. 100 nm diameter spherical particles are drawn in the top part at the scale of the corresponding images.

c) Contact angles

The contact angles of water and *o*-DCB on the ODTS-treated nano-grooved surface were measured before and after VUV light irradiation. The contact angles of water (*o*-DCB) depended on the viewing direction (**Figure 5.7**) and were reduced from >110° (>50°) to ~11° (~11°) as shown in **Table 5.1** and **Figure 5.7**.

Table 5.1 Contact angles of water and of *o*-DCB on the highly hydrophobic nano-grooved SiO$_2$ surfaces measured before and after VUV-light exposure.

	Before VUV-light exposure		After VUV-light exposure	
	Parallel*	Perpendicular*	Parallel*	Perpendicular*
Water	113°	112°	14°	7°
o-DCB	53°	51°	9°	9°

* parallel and perpendicular denotes the measurement configurations shown in **Figure 5.7**.
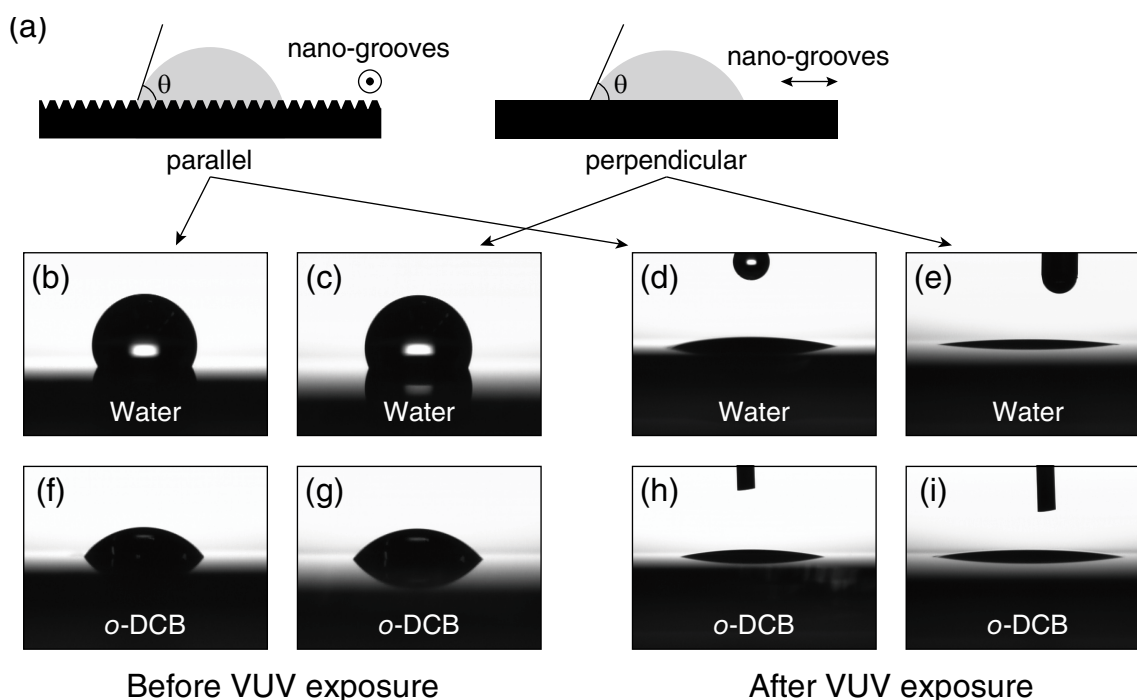
Figure 5.7 (a): Definitions of "parallel" and "perpendicular" configurations with respect to the direction of the nano-grooves in the contact angle measurement. Contact angles of (b, c, d, e): water and (f, g, h, i): *o*-DCB on the nano-grooved SiO$_2$ surface with (b, c, f, g): and without (d, e, h, i): ODTS SAM (before and after VUV-light exposure, respectively) for (b, d, f, h): "parallel" and (c, e, g, i): "perpendicular" configurations.

5.3.2 Characterization of the OSC film

The characterization of the pBTTT-C16 film was performed after the fabrication and all the electrical measurements of the OFET array (see **Section 5.3.3** and **Chapter 6**).

a) AFM images

Figure 5.8a and **Figure 5.8**b are AFM images (2 × 2 μm^2 and 5 × 5 μm^2, respectively) of the pBTTT-C16 active layer of the OFET array fabricated by spin-coating on the nano-grooved surface. The terrace structure with clear steps of ~2.2 nm was observed. The line profile along the broken line in **Figure 5.8**a is shown in **Figure 5.8**c. Interestingly, the terraced structure appeared to be continuous across the shallow

dent lines, which probably correspond to nano-grooves less than 2 nm deep, as judged from the density of the dent lines. Except for the unidirectional dent line features, no in-plane anisotropy was observed in the film morphology. This is presumably because of the rheological properties of the smectic mesophase of pBTTT-C16 that appears during annealing at 150°C. This mesophase consists of highly ordered layers of π-stacked backbone structures separated by melted alkyl side chains.[5.7] The melted side chains afford sufficient diffusivity to allow π-π stacking and in-plane alignment (see **Figure 5.10** and **Figure 5.11** below) of the backbone structures and the terraced morphology to improve considerably. However, the high viscosity of this mesophase[5.7] prevents the transfer of polymeric molecules over a long distance, resulting in the apparent continuity of the terraced structures across the shallow nano-grooves and in no production of morphologically anisotropic features.
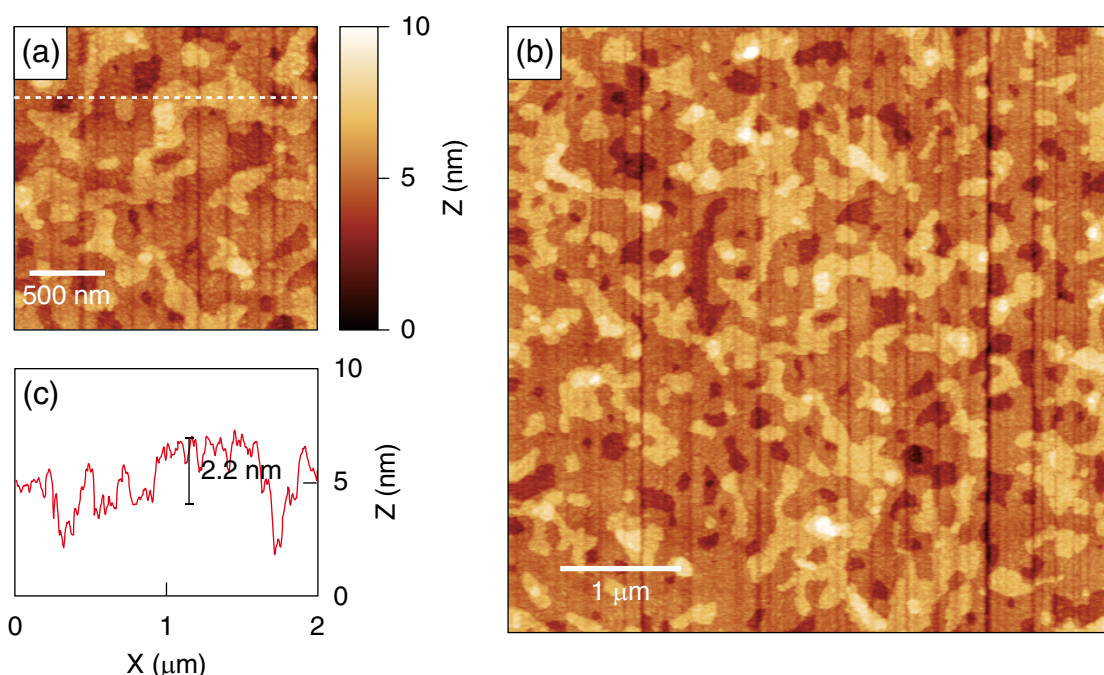
Figure 5.8   AFM images of the terrace-phase pBTTT-C16 film taken at the areas of (a): 2×2 μm² and (b): 5×5 μm², respectively together with the profile (c): along the white broken line in (a). The color scale in (b) is the same (10 nm) as in (a).

b) Film thickness

The thickness measurement of the pBTTT-C16 film spin coated on the nano-grooves was performed along 3 lines (72 positions) which are indicated in **Figure 5.9**a. **Figure 5.9**b and **Figure 5.9**c show the line profiles along the blue and black segments in **Figure 5.9**a, respectively. The dents used for the measurements are the lines on which pBTTT-C16 was removed by a probe for OFET isolation. The film thickness was found to be 24 ± 2 nm.
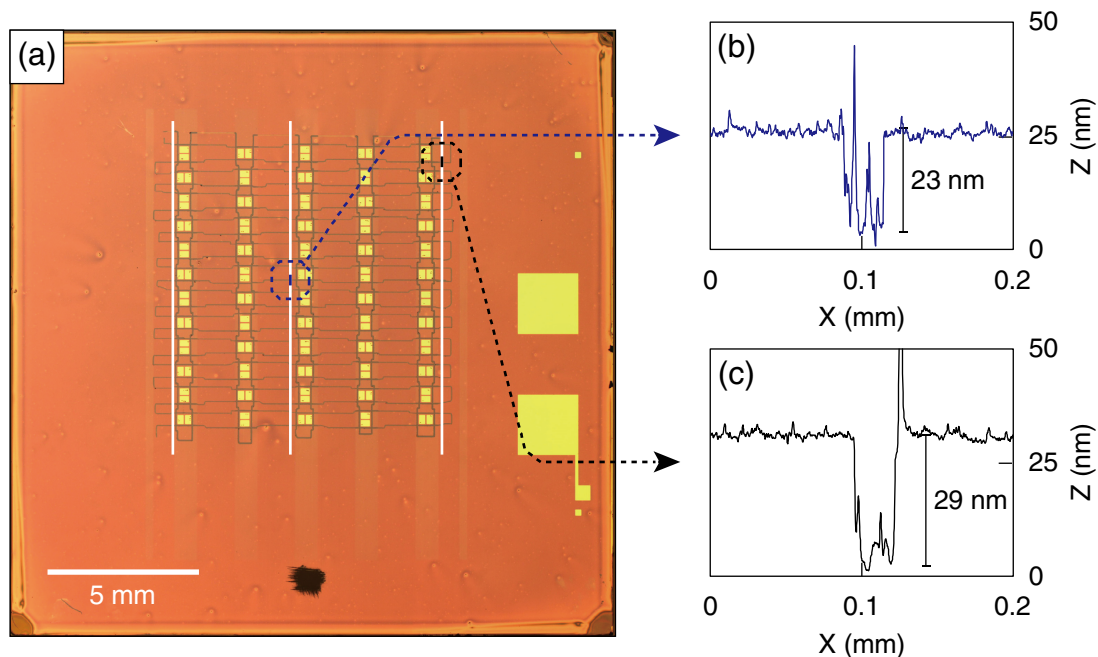
Figure 5.9 (a): Optical microscope image of the pBTTT-C16 OFET array fabricated on the nano-grooves. The pBTTT film thickness measurement was performed along the white lines. The extracted profiles along the segments highlighted in blue and black are shown in (b) and (c), respectively.

c) Polarized optical microscope images

The in-plane molecular orientation of the pBTTT active layer was examined by POM observation. **Figure 5.10**a and **Figure 5.10**b are the magnified POM images of the OFET array captured in the reflection geometry of crossed Nicols at sample rotation angles of 0 and 45°, respectively. When the nano-groove direction (thin double-sided arrow) was parallel with the transmission axis of the polarizer (thick double-sided arrow marked by "P"), the entire substrate surface was dark. This orientation is defined as sample rotation angle of 0°. After the sample was rotated by 45° around the surface normal, the hydrophobic regions became noticeably bright, whereas the brightness of the hydrophilic regions hardly changed, as seen in **Figure 5.10**b, even though the nano-grooves were uniformly formed over the entire substrate surface. The brightness oscillation occurred four times in 90° increments over a rotation range of 360°. These results indicate that the birefringence originating from the alignment of pBTTT backbone structures was much larger in the
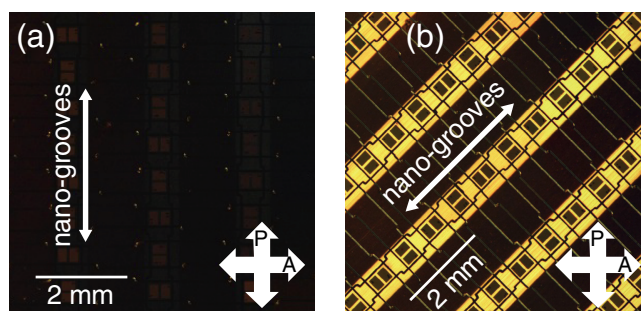
Figure 5.10 POM images of the pBTTT-C16 OFET arrays formed on nano-grooved SiO_2 surfaces at sample rotation angles of (a) 0 and (b) 45°.

hydrophobic regions than in the hydrophilic regions, and that the slow or fast axis was parallel to the direction of the nano-grooves.

d) Polarized Raman spectra

The alignment of the pBTTT backbone structures parallel to the nano-groove direction was confirmed with the help of the polarization dependence of Raman spectra (**Figure 5.11**). The measurement was performed as was described in **Chapter 3**. Three strong bands were observed at 1393, 1417, and 1491 cm^{-1}. The 1393 and 1491 cm^{-1} bands were assigned to the C-C and C=C stretching vibrations of the thiophene ring, respectively, and the 1417 cm^{-1} band was assigned to the C=C stretching bands of the thienothiophene ring.[5.8],[5.9] In the *hydrophobic* areas, these three bands showed the same polarization dependence: $I_{//}^{pho}/I_{\perp}^{pho} = 2.3$ (**Figure 5.11**a). This polarization dependence indicates that the pBTTT-C16 backbone structures align on average along the direction of the nano-grooves. The same Raman measurement was also performed on the terrace-phase pBTTT-C16 film formed on the *hydrophilic* nano-grooved surface, and the Raman spectra are shown in **Figure 5.11**b. As suggested by the POM observations, the polarization dependence for the *hydrophilic* surface area ($I_{//}^{phi}/I_{\perp}^{phi} = 1.07$) was much smaller than that for the highly *hydrophobic* surface area. This result reveals poor alignment ability of the *hydrophilic* nano-grooved surface, indicating that the hydrophobicity of nano-grooved surface is crucial for inducing high degree of alignment of the pBTTT backbone structure. The alignment degree obtained by the *hydrophobic* nano-grooves was much higher than that obtained by SAF-coating ($I_{//}^{SAF}/I_{\perp}^{SAF} = 1.08$, see p.32).[5.3]
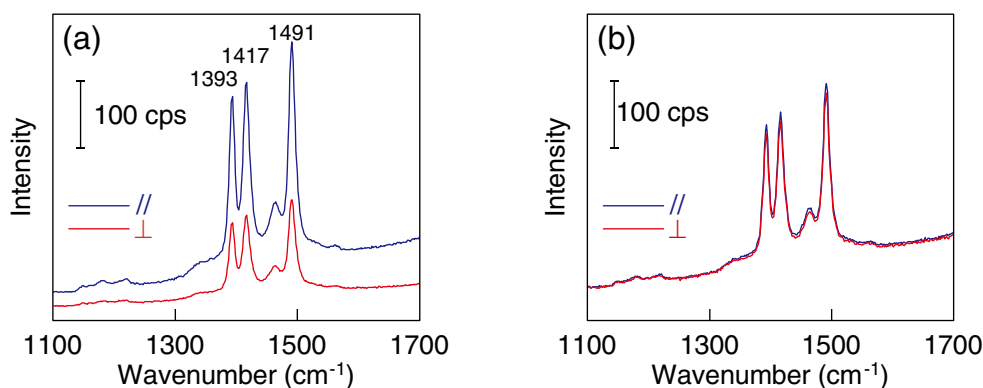
Figure 5.11 Polarized Raman spectra of the terrace-phase pBTTT-C16 film formed on (a) highly *hydrophobic* and (b) *hydrophilic* nano-grooved SiO$_2$ surfaces.

5.3.3 OFET device properties

To evaluate the in-plane anisotropy of the charge transport and the DDV, the transfer and output characteristics of all devices in the OFET array were measured in the saturation regime. For comparison, evaluation of an OFET array composed of 40 devices fabricated on an ODTS-treated SiO$_2$/n$^+$-Si substrate without nano-grooves was also performed (hereafter, these OFETs are denoted as *isotropic* OFETs. In the transfer (output) characteristic measurement, the gate-source voltage V_{GS} (drain-source voltage V_{DS}) was first varied from +5 (+1) to -30 (-30) V, which is the forward sweep; the reverse sweep was conducted immediately after. The typical output characteristics of the *parallel*, *perpendicular*, and *isotropic* OFETs are shown in **Figure 5.12**a, **Figure 5.12**b, and **Figure 5.12**c, respectively. The transfer characteristics of the three OFETs are presented in **Figure 5.12**d. For the three types of OFETs, good *p*-channel transistor behavior with sharp
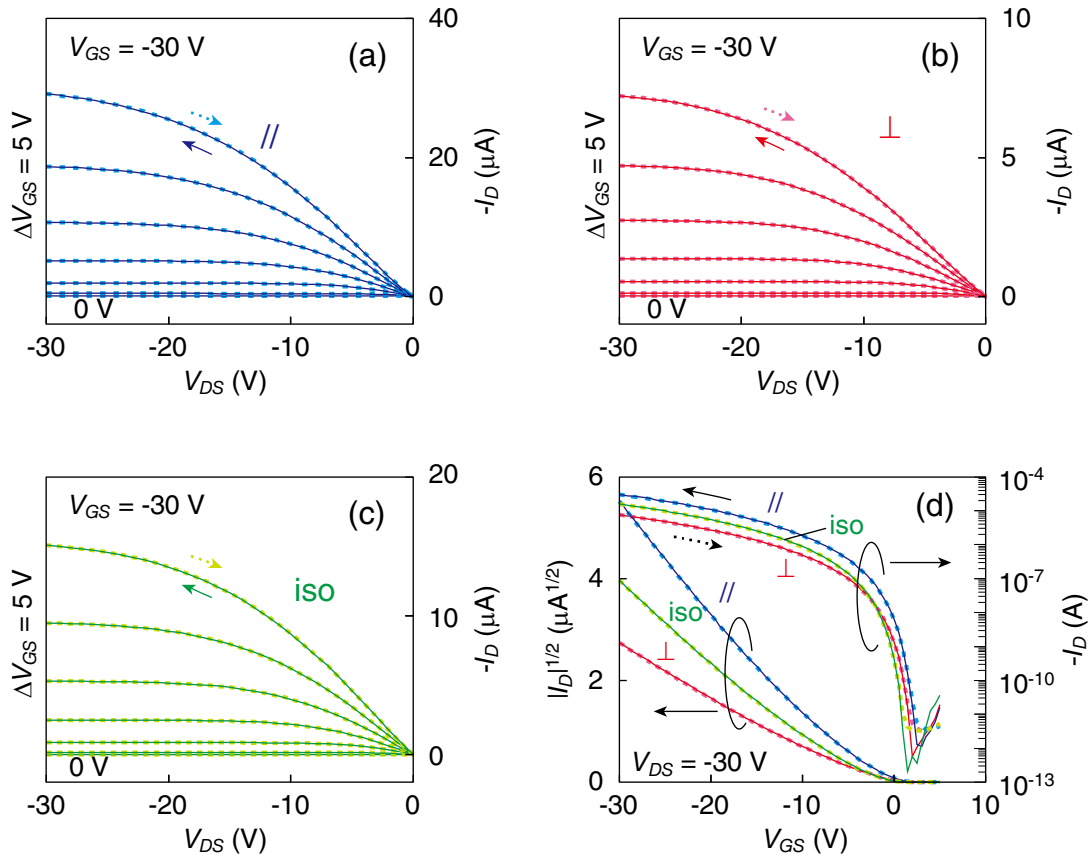
Figure 5.12 Typical output characteristics of (a) *parallel*, (b) *perpendicular* and (c) *isotropic* OFETs. The V_{GS} was varied in steps of 5 V. (d) Typical transfer characteristics in the saturation (V_{DS} = -30 V) regime of a *parallel*, *perpendicular* and *isotropic* OFETs all shown in a single chart.

turn on/off characteristics was observed without I_D hysteresis between the forward and reverse sweeps. The maximum current on/off ratio was greater than 10^7.

The field-effect hole mobility μ, threshold voltage V_{th}, and subthreshold swing *SS* were determined from the transfer characteristics in the forward V_{GS} sweep. The μ and V_{th} were derived using **Equation 2.9** and **Equation 2.11** (see p.7). The value of the gate dielectric capacitance C_i was 34.1 nF/cm^2 for the *parallel* and
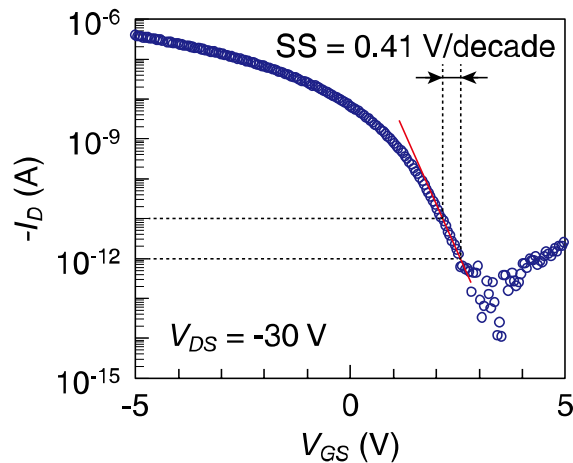
Figure 5.13 Typical partial transfer characteristics of one of the *parallel* OFETs measured to determine SS.

perpendicular OFETs and 33.6 nF/cm^2 for the *isotropic* OFETs. The carrier mobilities of the *parallel*, *perpendicular* and *isotropic* OFETs shown in **Figure 5.12** were 0.51, 0.12 and 0.28 cm$^2 \cdot$V$^{-1} \cdot$s^{-1}, respectively. For evaluation of *SS* with higher accuracy, the partial transfer characteristics (**Figure 5.13**) were separately measured by varying V_{GS} from 5 to -5 V at intervals of 0.05 V as opposed to 0.5 V interval in the measurement of **Figure 5.12**d.

The device characteristics were also measured for OFETs without nano-grooves fabricated in the *hydrophilic* areas. The typical output and transfer characteristics of such 'hydrophilic' OFET are shown in **Figure 5.14**. Although good *p*-channel transistor behavior was observed, the maximum $|I_D|$ was more than one order of magnitude lower resulting in carrier mobility of ~0.006 cm$^2 \cdot$V$^{-1} \cdot$s^{-1} (~50 times lower than that of an *isotropic* OFET).
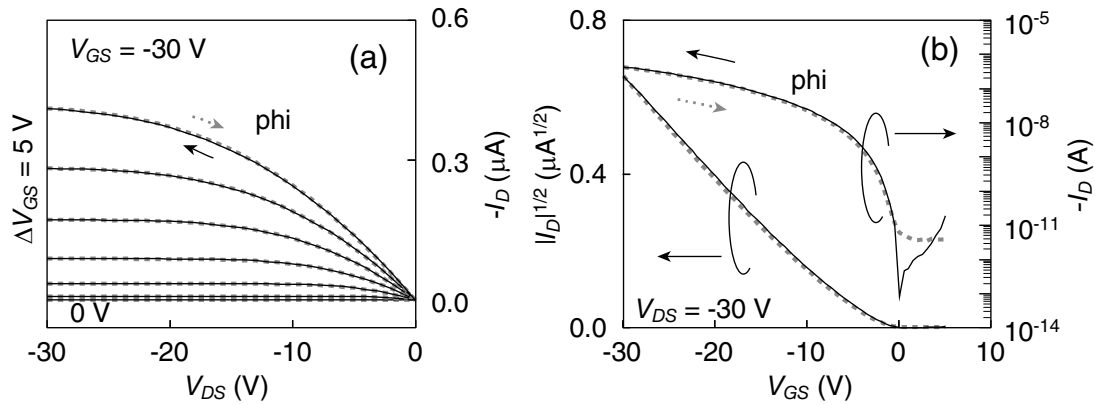
Figure 5.14   Typical (a): output and (b): transfer characteristics of a pBTTT-C16 OFET fabricated on the SiO$_2$ surface without nano-grooves in the *hydrophilic* area.

The histograms of μ, V_{th}, and *SS* are shown in **Figure 5.15**a, **Figure 5.15**b and **Figure 5.15**c, respectively. The solid, open, and hatched bars show the data for the *parallel*, *perpendicular*, and *isotropic* OFETs, respectively. Their average values (A_v), standard deviations (σ), and relative standard deviations (σ / A_v) are summarized in **Table 5.2**. The DDV of the electrical properties were very small for the *parallel* and *isotropic* OFETs and small for the *perpendicular* OFETs. The relative standard deviations of μ were less than 4, 10, and
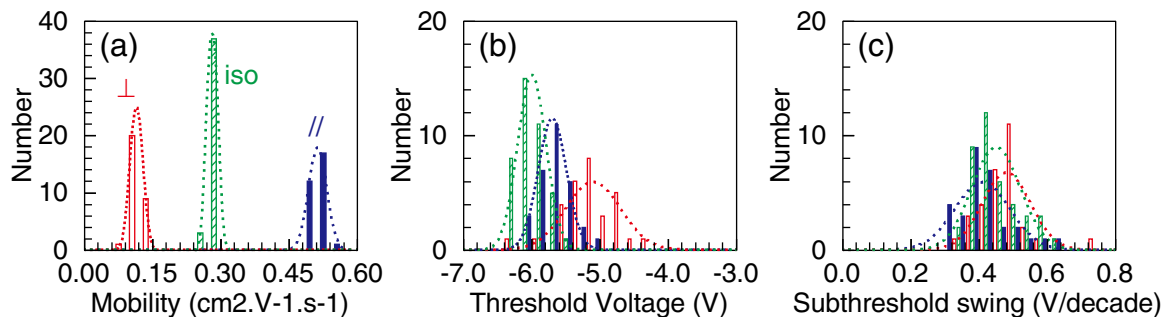
Figure 5.15   Histograms of a) field-effect hole mobility, b) threshold voltage, and c) subthreshold swing of 30 *parallel* (//), 30 *perpendicular* (⊥), and 40 *isotropic* (iso) pBTTT-C16 OFETs. The filled, open, and hatched bars show the results for the *parallel*, *perpendicular*, and *isotropic* OFETs, respectively. The bin widths of the histograms are a) 0.03 cm$^2 \cdot$V$^{-1} \cdot$s^{-1}, b) 0.2 V, and c) 0.04 V per decade. The broken curves represent the normal distributions defined by A$_v$ and σ in **Table 5.2**

3% for the *parallel*, *perpendicular*, and *isotropic* OFETs, respectively. This indicates that the spatial uniformity in the charge transport along the nano-groove direction was hardly degraded by forming nano-grooves on the gate dielectric surface, whereas that along the orthogonal direction was slightly degraded but was still high. In addition to μ, very narrow distributions of V_{th} and SS were observed for the three types of OFETs. **Figure 5.15**b shows that the average values of V_{th} were the largest (in positive direction) for *perpendicular* OFETs and the smallest for *isotropic* ones. The distribution of V_{th} was slightly wider for the *perpendicular* OFETs than for the *parallel* and *isotropic* OFETs. However, the difference in the average values was less than 1 V, and the standard deviation for the *perpendicular* OFETs remained small (0.4 V). Because such small differences are often observed between *isotropic* OFET arrays fabricated on different substrates, such small differences could not be associated with the presence of nano-grooves. **Figure 5.15**c shows that the average value of SS and its standard deviation were approximately 0.45 V/decade and less than 0.08 V/decade, respectively, for all three types of OFETs, which were hardly distinguishable. Thus, we can conclude that the nano-grooves on the gate dielectric surface had no significant influence on the turn on/off characteristics nor the spatial uniformity in the charge transport along the nano-groove direction.

To show visually the very small DDV of the transfer characteristics, the transfer curves of 30 *parallel*, 30 *perpendicular*, and 40 *isotropic* OFETs are plotted in **Figure 5.16**. To maintain the visibility, only the transfer curves in the forward sweep are plotted. The *parallel* and *isotropic* OFETs each showed excellent overlapping. For the *perpendicular* OFETs, the degree of overlapping was slightly degraded, which was attributed to the slightly wider distribution of $\mu_\perp$.
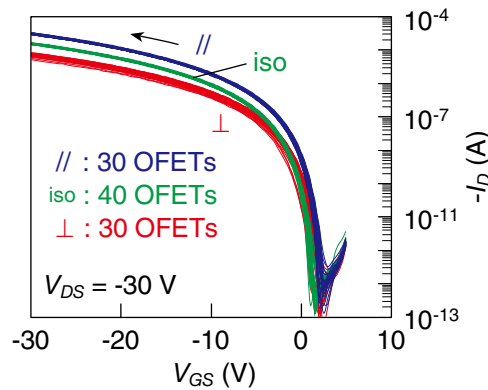
Figure 5.16   Overlaid transfer curves of all 30 *parallel*, 30 *perpendicular* and 40 *isotropic* OFETs

Table 5.2   Electrical properties (μ, V_{th} and SS) of the *parallel*, *perpendicular* OFETs fabricated on hydrophobic nano-grooved SiO_2 surface, and *isotropic* pBTTT-C16 OFETs (without nano-grooves) measured in the saturation regime.

	Parallel OFETs			*Perpendicular* OFETs			Isotropic OFETs		
	A_v	σ	σ/A_v	A_v	σ	σ/A_v	A_v	σ	σ/A_v
μ [cm²·V⁻¹·s⁻¹]	0.513	0.018	3.5%	0.114	0.011	9.6%	0.281	0.008	2.8%
V_{th} [V]	-5.7	0.2		-5.1	0.4		-6.0	0.2	
SS [V per decade]	0.41	0.08		0.48	0.07		0.45	0.07	

5.3.4 Discussion

The field-effect mobilities of the *parallel*, *perpendicular*, and *isotropic* OFETs ($\mu_{//}$, $\mu_{\perp}$, and μ_{iso}) were 0.513 $\pm$ 0.018, 0.114 $\pm$ 0.011, and 0.273 $\pm$ 0.007 cm$^2 \cdot$V$^{-1} \cdot$s^{-1}, respectively. Because of the small DDV, the distributions of $\mu_{//}$, $\mu_{\perp}$, and μ_{iso} were completely separated from each other, as seen in **Figure 5.15**a. The in-plane charge transport anisotropy ($\mu_{//}$ / $\mu_{\perp}$) was 4.5, and $\mu_{//}$ was approximately twice μ_{iso}. These results clearly indicate that the mobility was enhanced by the unidirectional alignment of pBTTT backbone structures.[5.1]

As listed up in **Table 5.3**, the alignment methods capable of achieving alignment-induced mobility enhancement of terrace-phase pBTTT films were reported for pBTTT by other groups. However, for instance for the strain alignment method, mobility enhancement was achieved only for short-channel (< 10 μm) OFETs.[5.10] For longer channel OFETs, the field-effect mobility of the 50 % strained film was degraded and its in-plane anisotropy was decreased. This could be explained by the appearance of voids in the pBTTT-C14 film. The voids were created because of the film dewetting during the strain-alignment process. By the use of other alignment methods such as FTM method[5.11] and compression on ILs,[5.12] the alignment-induced mobility enhancement was also achieved but the corresponding DDVs (σ / A_v) were very large: namely > 60 % and > 40 %, respectively. The dependence of the field-effect mobility on the channel length and the large DDVs imply the poor spatial uniformity of the pBTTT active layers. Various other alignment techniques including the use of photo-aligned polyvinylcinnamate (PVCN) gate dielectric,[5.13] high temperature rubbing,[5.14] and capillary action[5.15] are capable of achieving anisotropic charge transport of terrace-phase pBTTT-Cn films although the mobility itself was degraded. This is probably due to deterioration of the π-π stacking caused by intermolecular interaction between PVCN and pBTTT-C14, mechanical force, and poor hydrophobicity of substrates, respectively. Therefore, to our knowledge, the present results are the first to report on the formation of terrace-phase pBTTT active layers exhibiting alignment-induced field-effect mobility enhancement with high spatial uniformity, which is supported by the very small DDV of *parallel* OFETs (< 4%). Furthermore, we want to emphasize here that the alignment technique used in this study is very simple compared to the strain-alignment, FTM, and compression on ILs.

Table 5.3   Summary of the alignment-induced mobility enhancement ($\mu_{//}$ / μ_{iso}) of terrace-phase pBTTT films achieved by various alignment methods. $\mu_{//}$ and σ / A_v are the field-effect hole mobility along the alignment direction of pBTTT backbone structures and its device-to-device variation (relative standard deviation), respectively. μ_{iso} is the field-effect hole mobility of the non-aligned pBTTT film. L is the channel lengths of the OFETs used for the evaluation of $\mu_{//}$ and μ_{iso}.

Alignment method	L [μm]	$\mu_{//}$ [cm$^2 \cdot$V$^{-1} \cdot$s^{-1}]	σ / A_v	Enhancement [$\mu_{//}$ / μ_{iso}]	Ref.
Strain (50 %)	5	1.5	13 %	1.8	[5.10]
Strain (50 %)	50	0.12	4 %	0.5 (degraded)	[5.10]
FTM	20	0.4	63 %	5	[5.11]
Compression on ILs	Unspecified	0.4	43 %	4	[5.12]

5.4   Summary

In this study, we fabricated an array composed of *parallel* and *perpendicular* OFETs of 30 each with terrace-phase pBTTT-C16 active layers aligned by a highly hydrophobic nano-grooved gate dielectric surface. The surface exhibited a water contact angle of greater than 110°. The repellent nature of such a surface makes thin pBTTT-C16 film formation impossible by spin-coating. This problem was solved by producing a suitable hydrophobic/hydrophilic pattern by VUV-light exposure through a photomask. For comparison, an additional array composed of 40 *isotropic* OFETs was fabricated on a highly hydrophobic gate dielectric surface without nano-grooves. The in-plane anisotropy and spatial uniformity in the charge transport of the aligned pBTTT-C16 active layer were assessed by measuring the electrical properties of all the OFETs. The field-effect hole mobilities of the *parallel*, *perpendicular*, and *isotropic* OFETs in the saturation regime were 0.513 ± 0.018, 0.114 ± 0.011, and 0.273 ± 0.007 cm^2·V^{-1}·s^{-1}, respectively. The in-plane anisotropy ($\mu_{//} / \mu_{\perp}$) of ~5 and the alignment-induced mobility enhancement ($\mu_{//} / \mu_{iso}$) of a factor of ~2 were successfully achieved using the highly hydrophobic nano-grooved surface. The DDV of the *parallel* OFETs was slightly greater than that (3%) of the *isotropic* OFETs but was still less than 4%. The very small DDV indicates that the spatial uniformity in the charge transport along the nano-groove direction (average orientation direction of pBTTT backbone structure) was very high. To our knowledge, this study[5.1] is the first to report the formation of an array of OFETs with terrace-phase pBTTT active layers exhibiting alignment-induced field-effect mobility enhancement and small DDV.

References

[5.1] K. Bulgarevich, K. Sakamoto, T. Minari, T. Yasuda, K. Miki, and M. Takeuchi. "Polymer-Based Organic Field-Effect Transistors with Active Layers Aligned by Highly Hydrophobic Nanogrooved Surfaces." *Adv. Funct. Mater.* **2019**, 29, 1905365.

[5.2] K. Sakamoto, J. Ueno, K. Bulgarevich, and K. Miki. "Anisotropic Charge Transport and Contact Resistance of 6,13-bis(triisopropylsilylethynyl) Pentacene Field-Effect Transistors Fabricated by a Modified Flow-Coating Method." *Appl. Phys. Lett*. **2012**, 100, 123301.

[5.3] K. Bulgarevich, K. Sakamoto, T. Minari, T. Yasuda, and K. Miki. "Spatially Uniform Thin-Film Formation of Polymeric Organic Semiconductors on Lyophobic Gate Insulator Surfaces by Self-Assisted Flow-Coating." *ACS Appl. Mater. Interfaces* **2017**, 9, 6237.

[5.4] D. E. Johnston, K. G. Yager, H. Hlaing, X. Lu, B. M. Ocko, and C. T. Black. "Nanostructured Surfaces Frustrate Polymer Semiconductor Molecular Orientation." *ACS Nano* **2014**, 8, 243.

[5.5] H.-R. Tseng, H. Phan, C. Luo, M. Wang, L. A. Perez, S. N. Patel, L. Ying, E. J. Kramer, T.-Q. Nguyen, G. C. Bazan, and A. J. Heeger. "High-Mobility Field-Effect Transistors Fabricated with Macroscopic Aligned Semiconducting Polymers." *Adv. Mater.* **2014**, 26, 2993.

[5.6] C. Luo, A. K. K. Kyaw, L. A. Perez, S. Patel, M. Wang, B. Grimm, G. C. Bazan, E. J. Kramer, and A. J. Heeger. "General Strategy for Self-Assembly of Highly Oriented Nanocrystalline Semiconducting Polymers with High Mobility." *Nano Lett.* **2014**, 14, 2764.

[5.7] D. M. DeLongchamp, R. J. Kline, Y. Jung, E. K. Lin, D. A. Fischer, D. J. Gundlach, S. K. Cotts, A. J. Moad, L. J. Richter, M. F. Toney, M. Heeney, and I. McCulloch. "Molecular Basis of Mesophase Ordering in a Thiophene-Based Copolymer." *Macromolecules* **2008**, 41, 5709.

[5.8] J. Gao, A. K. Thomas, R. Johnson, H. Guo, and J. K. Grey. "Spatially Resolving Ordered and Disordered Conformers and Photocurrent Generation in Intercalated Conjugated Polymer/Fullerene Blend Solar Cells." *Chem. Mater.* **2014**, 26, 4395.

[5.9] Y. Furukawa, K. Akiyama, I. Enokida, and J. Yamamoto. "Raman Spectra of Carriers in Ionic-Liquid-Gated Transistors Fabricated with. Poly(2,5-bis(3-tetradecylthiophen-2-yl)thieno[3,2-b]thiophene)." *Vib. Spectro.* **2016**, 85, 29.

[5.10] X. Xue, G. Chandler, X. Zhang, R. J. Kline, Z. Fei, M. Heeney, P. J. Diemer, O. D. Jurchescu, and B. T. O'Connor. "Oriented Liquid Crystalline Polymer Semiconductor Films with Large Ordered Domains." *ACS Appl. Mater. Interfaces* **2015**, 7, 26726.

[5.11] M. Pandey, A. Gowda, S. Nagamatsu, S. Kumar, W. Takashima, S. Hayase, and S. S. Pandey. "Rapid Formation and Macroscopic Self-Assembly of Liquid-Crystalline, High-Mobility, Semiconducting Thienothiophene." *Adv. Mater. Interfaces* **2018**, 5, 1700875.

[5.12] J. Soeda, H. Matsui, T. Okamoto, I. Osaka, K. Takimiya, and J. Takeya. "Highly Oriented Polymer Semiconductor Films Compressed at the Surface of Ionic Liquids for High-Performance Polymeric Organic Field-Effect Transistors." *Adv. Mater*. **2014**, 26, 6430.

[5.13] J. W. Bae, and K. Song. "Anisotropic Charge-Carrier Mobilities of Liquid Crystalline Conjugated Polymers on Photo-Aligned PVCN Dielectric Insulators." *Org. Electron*. **2016**, 30, 143.

[5.14] L. Biniek, N. Leclerc, T. Heiser, R. Bechara, and M. Brinkmann. "Large Scale Alignment and Charge Transport Anisotropy of pBTTT Films Oriented by High Temperature Rubbing." *Macromolecules* **2013**, 46, 4014.

[5.15] T. Higashi, N. Yamasaki, H. Utsumi, H. Yoshida, A. Fujii, and M. Ozaki. "Anisotropic Properties of Aligned π-Conjugated Polymer Films Fabricated by Capillary Action and Their Post-Annealing Effects." *Appl. Phys. Express* **2011**, 4, 091602.

Chapter 6 Bias-stress effect in OFETs

High operational stability is a prerequisite for commercialization of OFETs along with high carrier mobility and small DDV. In this chapter, the operational stability of pBTTT-C16 OFETs was evaluated along the widely used procedure of measurement of the threshold voltage shift under constant prolonged gate bias-stress. The effect of the nano-grooved gate dielectric surface on the operational stability was investigated. The bias stress effect was also measured for OFETs with active layers of one of the high-mobility D-A copolymer, PCDTPT. It was found that the operational stability of pBTTT-C16 OFETs is comparable to that of a-Si FETs and is much higher than that of PCDTPT OFETs. The semicrystalline polymers such as pBTTT are still attractive despite the relatively low carrier mobility compared to D-A copolymers. The adverse effect of the nano-grooves on the operational stability was confirmed to be small.

6.1 Evaluation of operational stability

The long-term stability against bias stress during continuous operation of the OFETs is important for their commercial application. The gradual shift of the threshold voltage, at which the transistors switch on, with time toward the applied gate bias voltage is an undesirable operational instability known as the "bias-stress effect". The first study of the bias-stress effect in OFETs was conducted by Matters et al. in 1999.[6.1] In their study on polythienylene vinylene OFETs, they observed a reversible V_{th} shift under a constant negative V_{GS}.

The commonly used model for quantitative analysis of the V_{th} shift is the one that describes that in a-Si FETs. The V_{th} shift simply depends on the density of trapped charges N_{tr}:

$$\Delta V_{th} = eN_{tr}/C_i,$$ (6.1)

where C_i is the capacitance of the gate dielectric per unit area. The charge-trapping rate is assumed to be related on the free-carrier density N_f according to the diffusion theory:

$$\frac{dN_{tr}}{dt} = N_f \frac{t^{\beta-1}}{\tau^\beta}.$$ (6.2)

In **Equation 6.2**, τ is the characteristic time or the trapping time constant of carriers to fill trap levels, and β is the dispersion parameter. Solving this equation gives a stretched exponential function for $\Delta V_{th}(t)$:

$$\Delta V_{th}(t) = \left(V_{GS} - V_{th}(0)\right) \cdot \left\{1 - exp\left[-\left(\frac{t}{\tau}\right)^\beta\right]\right\}.$$ (6.3)

A small value of the stretching factor of the exponential function β ($0 \leq \beta \leq 1$), which represents the distribution of time constants, correspond to a wide trapping barrier height distribution.[6.2]

The effect of the characteristic time τ and the stretching factor β on the V_{th} shift is visualized in **Figure 6.1**. One can see that the changes in τ result in the shifting of the stretched exponential function and the changes β in result in that's stretching. Obviously, after application of bias-stress for time τ, the V_{th} shift is (1 - 1/e) of the effective applied bias $V_{GS} - V_{th}(0)$ regardless of the value of β. This means that the time variation of the stretched exponential function is faster than the exponential function until τ and slower thereafter. Also, smaller β results in faster V_{th} shift at the initial stage of bias-stress application as a small value of β correspond to a wide trapping barrier height distribution.

$w_4 < w_5 < w_6$

0

$V_{th} - V_{th}(0)$

$\dfrac{V_{GS}-V_{th}(0)}{e}$

log(Stress time)

$V_{GS} - V_{th}(0)$

$w_4 < w_5 < w_6$
Change in w: shifting
Larger w: better stability

- - - : e = 1 —— : e = 0.4 —— : e = 0.2
Change in e: stretching
Larger e: better stability while
Stress time < w

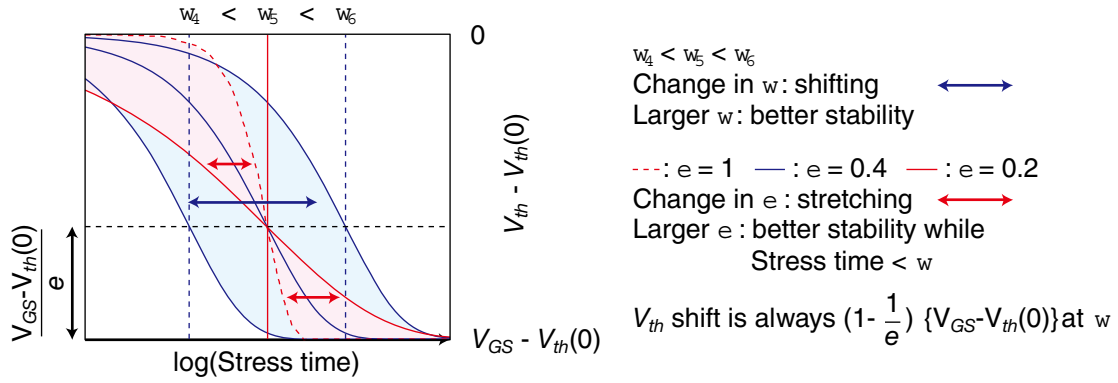V_{th} shift is always $(1-\dfrac{1}{e})$ {$V_{GS}-V_{th}(0)$} at w

Figure 6.1   Stretched exponential function.

The stability of OFETs against bias strass is generally measured as the variation of their transfer characteristics over time. Specifically, by repeating cycles of constant prolonged gate-bias application and transfer characteristic measurements. Alternatively, the drain current in linear regime ($|V_{DS}| \ll |V_{GS}|$) can be measured as a function of time under constant continuous V_{GS}. The second method is applicable, only when the field-effect mobility does not change during gate-bias stress application. When μ^{lin} is constant during bias-stress application, $\Delta V_{th}^{lin}/(V_{GS} - V_{th}^{lin}(0))$ is simply related to $I_D(t)$ in linear regime by:

$$\frac{\Delta V_{th}^{lin}(t)}{V_{GS} - V_{th}^{lin}(0)} = -\frac{I_D(t) - I_D(0)}{I_D(0)} = -\frac{\Delta I_D(t)}{I_D(0)}, \tag{6.4}$$

where $\Delta I_D(t)$ is defined as $I_D(t) - I_D(0)$.

Since parts of trapped charges are released during the transfer characteristic measurement and may affect the time dependence of bias-stress effects, the second method can be useful for analysis of devices with very high stability and/or high recovery rate. By applying **Equation 6.4**, **Equation 6.3** becomes:

$$I_D(t) = I_D(0) \cdot exp\left[-\left(\frac{t}{\tau}\right)^{\beta}\right]. \tag{6.5}$$

6.2   Fabrication of OFET arrays

6.2.1 pBTTT-C16 OFETs

In order to evaluate the operational stability of the pBTTT-C16 OFETs and check the effect of the nano-grooves on the operational stability, the bias-stress effect of the OFETs fabricated in **Chapter 5** was measured. The fabrication (**Section 5.2**, see p.44) and the initial electrical properties (**Section 5.3.3**, see p.51) of these OFETs were already discussed. The selected devices of the same OFET array were used for the bias-stress measurements.

6.2.2 PCDTPT OFETs

The PCDTPT OFETs with and without nano-grooves were also fabricated to compare the operational stability of D-A copolymer OFETs with semicrystalline ones. The structure of PCDTPT is shown in **Figure 6.2**a. The SiO_2/n$^+$-Si wafers were used which were cleaned, scratched, ODTS-treated and patterned with identical conditions as for the pBTTT-C16 OFETs. The PCDTPT films were formed by spin-coating from 0.25 wt.% solution of PCDTPT in chlorobenzene. The spin-coating (1000 rpm for 180 s) was performed in air
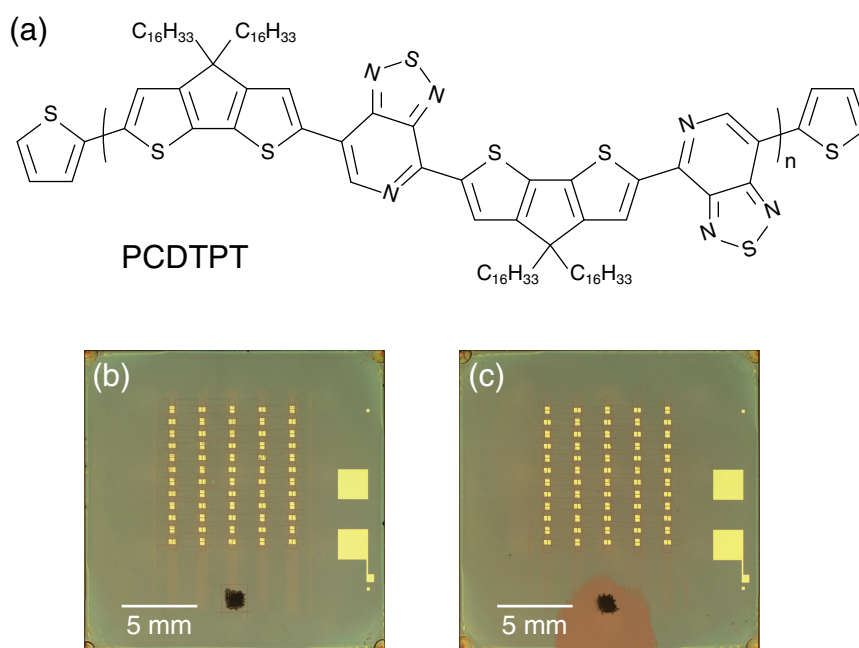
Figure 6.2 (a): Structure of PCDTPT. (b, c): Optical microscope images of the PCDTPT OFET arrays formed on SiO$_2$ surfaces (a): with and (b): without nano-grooves.

at RT. Finally, the films were annealed at 200°C for 15 min in a nitrogen atmosphere. The S/D electrodes were deposited in vacuum in the hydrophobic surface areas through the same shadow mask as pBTTT-C16 OFETs. The resulting OFET arrays with and without nano-grooves are shown in **Figure 6.2**b and **Figure 6.2**c, respectively.

Figure 6.3a and **Figure 6.3**b are the magnified POM images of the PCDTPT film formed on the nano-grooved SiO$_2$ surface which were captured in the reflection geometry of crossed Nicols at sample rotation angles of 0 and 45°, respectively. Similarly to the pBTTT film, (**Figure 5.10**, see p.50) the entire substrate surface was dark at 0°. After the substrate was rotated by 45° around the surface normal, the film on the hydrophobic areas become noticeably bright. The brightness oscillation occurred four times in 90° increments over a rotation range of 360°. These results indicate that the hydrophobic nano-grooves were effective for aligning the PCDTPT backbone structures.

Figure 6.3 POM images of the PCDTPT OFET arrays formed on SiO$_2$ surfaces at sample rotation angles of (a): 0° and (b): 45°.

6.2.3 Preparation of OSC films for X-Ray diffraction measurements

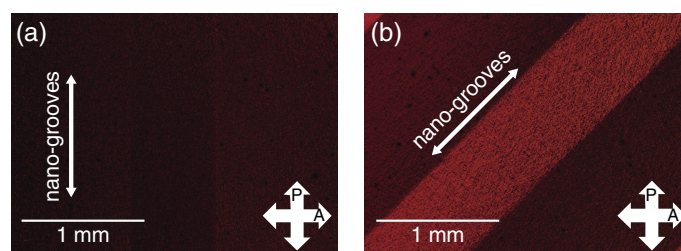The molecular packing and crystallinity of the pBTTT-C16 and PCDTPT films was investigated using X-Ray diffractometer (SmartLab, Rigaku). The Cu *Kα* radiation was used. Since the films of interest were the ones on the hydrophobic ODTS-treated surface, the hydrophobic/hydrophilic pattern of narrow (0.7 mm-wide) hydrophobic lines (**Figure 5.3**, see p.45) could not be used due to beam divergence. The hydrophobic/ hydrophilic patterns used to enable film formation of pBTTT-C16 and PCDTPT films for X-Ray diffraction (XRD) measurement are shown in **Figure 6.4**a and **Figure 6.4**b, respectively. As was shown in **Figure 3.16** (see p.33), the pattern of **Figure 6.4**b was not suitable for pBTTT. Unfortunately, these limitations restricted us from performing in-plane grazing incidence XRD measurements which for instance could reveal the degree of in-plane orientation. The film formation of pBTTT and PCDTPT was performed using the same conditions as explained in **Section 5.2.2** (see p.45) and **Section 6.2.2**, respectively.
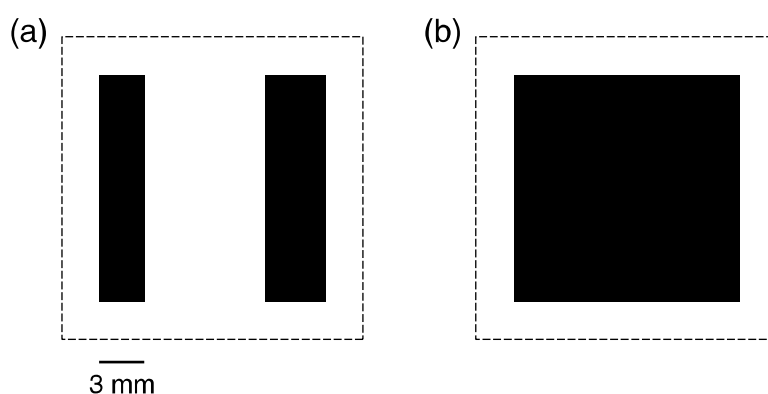

Figure 6.4   Photomask patterns that enable formation of (a): pBTTT-C16 and (b): PCDTPT films suitable for XRD measurements

6.3   Results and discussion

6.3.1 Operational stability of pBTTT-C16 OFETs

Because the operational stability is affected by the atmospheric oxygen and moisture, in this study, all the measurements were performed in vacuum after annealing in vacuum. This was done to distinguish the intrinsic operational stability from environmental stability because the latter can be improved by passivation and/or encapsulation. The bias-stress effect of the *parallel*, *perpendicular*, and *isotropic* pBTTT-C16 OFETs against an on-state gate bias was examined by repeating cycles of the application of a constant prolonged gate-bias (V_{GS}) stress and the measurement of transfer characteristics in the *linear* regime. Specifically, the initial transfer characteristics were measured by sequentially sweeping V_{GS} between 0 and -30 V in the forward and reverse directions at V_{DS} = -1 V, and a constant prolonged on-state bias-stress (V_{GS} = -30 V at V_{DS} = -1 V) was applied 1 h after completing the initial transfer characteristic measurement. At total bias stressing times of 5×10^2, 5×10, and 2.5×10^4 s, the on-state bias application was removed, and the linear transfer characteristics were measured immediately after.

Figure 6.5a shows the transfer characteristics of the *parallel*, *perpendicular*, and *isotropic* pBTTT-C16 OFETs at stress times of 0, 5×10^2, 5×10^3, 2.5×10^4 s. The threshold voltage shift was apparently observed for all the OFETs. The threshold voltage ($V_{th}{}^{lin}$) and the field-effect mobility (μ^{lin}) in the *linear* regime were derived using the following equation:

$$I_D = \frac{\mu^{lin} W C_i}{L} V_{DS} \left(V_{GS} - V_{th}^{lin} - \frac{V_{DS}}{2} \right). \tag{6.6}$$

The initial values of V_{th}^{lin} and μ^{lin} were -2.9 V and 0.252 cm²·V⁻¹·s⁻¹ for the *parallel* OFET, -3.0 V and 0.074 cm²·V⁻¹·s⁻¹ for the *perpendicular* OFET, and -4.9 V and 0.174 cm²·V⁻¹·s⁻¹ for the *isotropic* OFET, respectively. The bias-stress time dependence of V_{th}^{lin} shift ($\Delta V_{th}^{lin} = V_{th}^{lin}(t) - V_{th}^{lin}(0)$) and the normalized mobility ($\mu^{lin}/\mu^{lin}(0)$) are shown in **Figure 6.5**b. The μ^{lin} showed practically no change throughout the whole bias-stressing period for the three OFETs. The absolute values of ΔV_{th}^{lin} for the *parallel*, *perpendicular*, and *isotropic* OFETs were 3.4 V, 4.5 V, and 2.2 V, respectively, after bias stressing of 2.5×10^4 s. These results revealed that the formation of nano-grooves on the gate dielectric surface slightly reduced the resistance against the on-state gate-bias stress for both *parallel* and *perpendicular* OFETs. This may be related to the slight degradation of the overlap of the interchain π-π stacking due to the introduction of surface undulation (nano-grooves). The degree of reduction for the *perpendicular* OFET was greater than that for the *parallel* OFET. This directional dependence could be related to the difference in the number of interchain hoppings required for the charge transport between the S and D electrodes because the number depends on the channel current direction with respect to the alignment direction of the backbone structures.

The operational stability was quantitatively evaluated by fitting with a stretched exponential function of **Equation 6.3**. The broken curves in **Figure 6.5**b show the best fit results: $\tau = 1.0 \times 10^7$ s and $\beta = 0.334$ for the *parallel* OFET, $\tau = 8.6 \times 10^6$ s and $\beta = 0.292$ for the *perpendicular* OFET, and $\tau = 6.4 \times 10^8$ s and $\beta = 0.234$ for the *isotropic* OFET.[6.3] Although we cannot directly compare the values of τ among the three OFETs because of different β, the fitting result shows that forming nano-grooves on the gate dielectric surface reduced the operational stability by ~one order of magnitude.
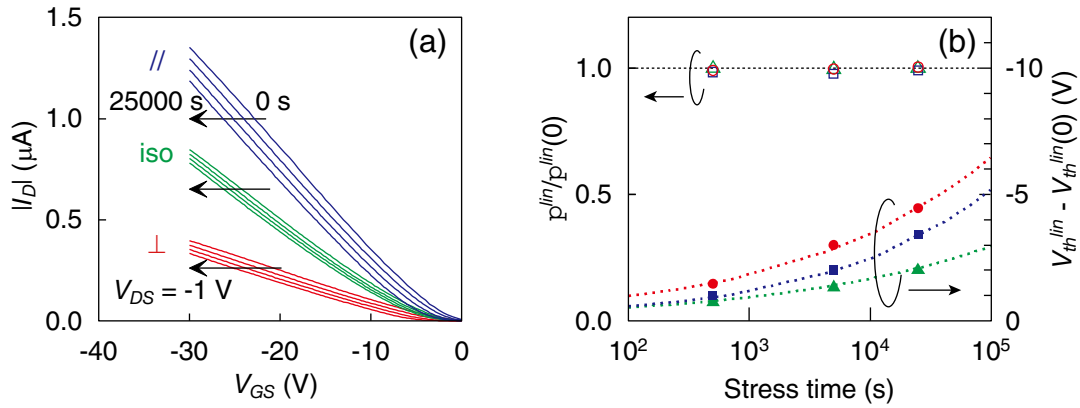
Figure 6.5   (a) Transfer characteristics of the *parallel*, *perpendicular* and *isotropic* (iso) pBTTT OFETs measured in the linear regime at bias stress times of 0, 5×10^2, 5×10^3, 2.5×10^4 s. (b) Bias-stress time dependence of the V_{th}^{lin} shifts (filled symbols) and of the normalized mobility (open symbols) of the OFETs. The circles, squares and triangles are the data points of *perpendicular*, *parallel* and *isotropic* OFETs, respectively. The broken curves in (b) represent the fitting results of the V_{th}^{lin} shifts with the stretched exponential functions.

6.3.2 PCDTPT OFET device properties

The transfer and output characteristics in the saturation regime of all devices in the PCDTPT OFET array with and without nano-grooves were measured. The maximum $|V_{GS}|$ and $|V_{DS}|$ were set to lower values than those for pBTTT OFETs (-30 V) to avoid the electron injection to the active layer at high positive (V_{GS} –
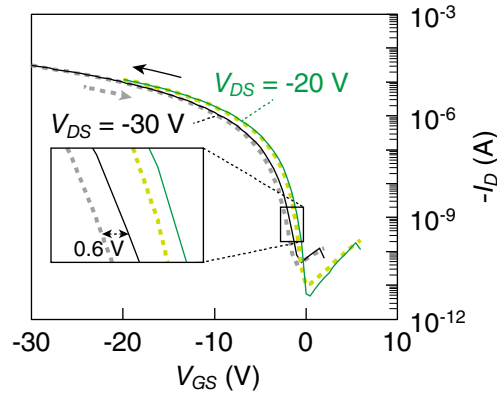
Figure 6.6 Transfer characteristics (first measurement) of one of the *isotropic* PCDTPT OFETs measured at V_{DS} of (V_{GS} up to) -20 (green) and -30 V (black). The solid and broken lines represent the forward and the backward sweeps, respectively.

V_{DS}) in the off region.[6.4] The electron injection resulted in the poor on/off ration of PCDTPT OFETs when measured at V_{DS} = -30 V as can be seen in **Figure 6.6**. To reduce this effect, the maximum V_{GS} and V_{DS} were set to -20 V. Also, from **Figure 6.6** we can already see that the stability against bias stress of the PCDTPT OFETs is probably lower compared to pBTTT-C16 OFETs, judging from the noticeable drain current hysteresis. The measurement of the transfer characteristics was repeated six times similarly to the pBTTT-C16
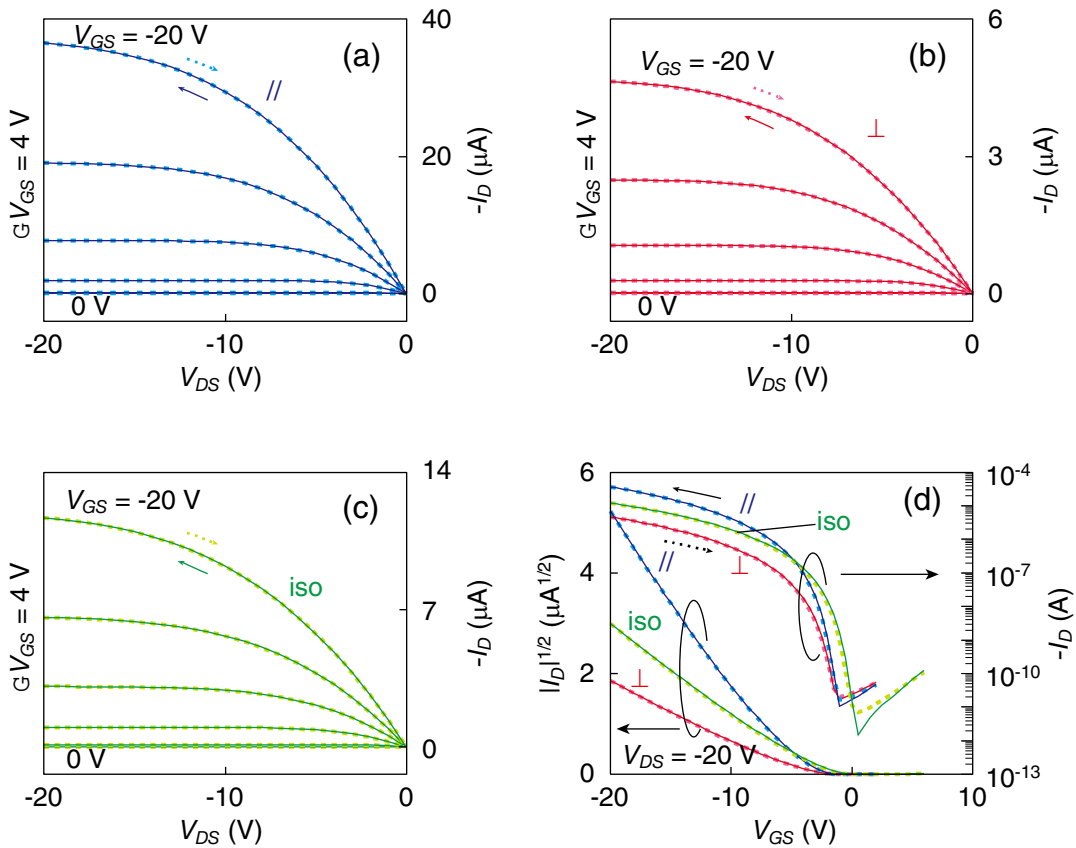
Figure 6.7 Typical output characteristics of (a) *parallel*, (b) *perpendicular* and (c) *isotropic* PCDTPT OFETs. The V_{GS} was varied in steps of 4 V. (d) Typical transfer characteristics in the saturation (V_{DS} = -20 V) regime of a *parallel*, *perpendicular* and *isotropic* OFETs all shown in a single chart.

OFETs and the data of the sixth measurement is presented if not specified otherwise. The typical output characteristics of the *parallel*, *perpendicular*, and *isotropic* OFETs are shown in **Figure 6.7a**, **Figure 6.7**b, and **Figure 6.7**c, respectively. The transfer characteristics of the three OFETs are presented in **Figure 6.7**d. The partial transfer characteristics (not shown) were separately measured by varying V_{GS} from 2 to -5 V at intervals of 0.05 V to determine *SS*. For these conditions, good *p*-channel transistor behavior with sharp turn on/off characteristics was observed with slight I_D hysteresis (~0.5 V) for the three types of OFETs. The maximum current on/off ratio was greater than 10^5 for *perpendicular* OFETs and greater than 10^6 for *parallel* and *isotropic* OFETs.
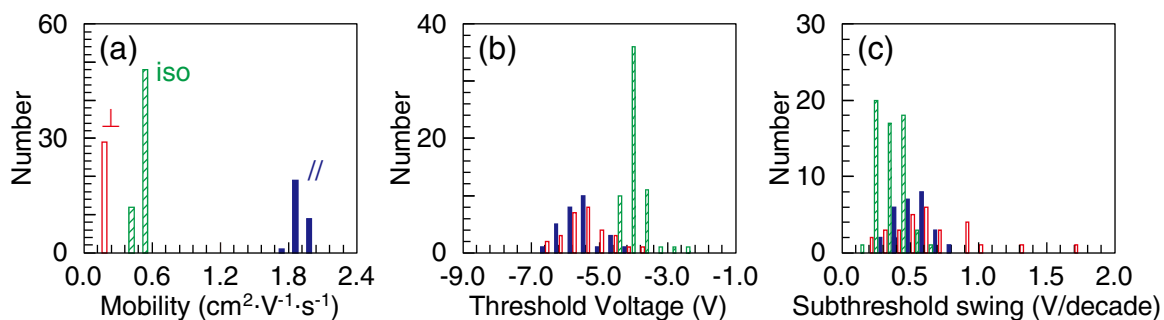

Figure 6.8   Histograms of a) field-effect hole mobility, b) threshold voltage, and c) subthreshold swing of 30 *parallel* (//), 30 *perpendicular* (⊥), and 40 *isotropic* (iso) PCDTPT OFETs. The filled, open, and hatched bars show the results for the *parallel*, *perpendicular*, and *isotropic* OFETs, respectively. The bin widths of the histograms are a) 0.12 cm²·V⁻¹·s⁻¹, b) 0.4 V, and c) 0.1 V per decade.

The histograms of μ, V_{th}, and *SS* are shown in **Figure 6.8a**, **Figure 6.8**b, and **Figure 6.8**c, respectively. Unfortunately, one of the *parallel* and one of the *perpendicular* OFETs were defected due to gate leakage. These two OFETs are excluded from statistical analysis. The solid, open, and hatched bars in **Figure 6.8** show the data for the *parallel*, *perpendicular*, and *isotropic* OFETs, respectively. Their average values (A_v), standard deviations (σ), and relative standard deviations (σ / A_v) are summarized in **Table 6.1**. The alignment-induced mobility enhancement ($\mu_{//}$ / μ_{iso} = 3.9) was achieved with high spatial uniformity for PCDTPT OFETs. Interestingly, the DDV of PCDTPT OFETs was suppressed by formation of the nano-grooves for both *parallel* and *perpendicular* OFETs compared to *isotropic* OFETs (3%, 4% and 6%, respectively for carrier mobility). Although the DDV in V_{th} was larger than that of pBTTT-C16 OFETs, it was still small. These results confirm the universality of the highly hydrophobic nano-grooved surfaces as alignment-inducing layers.

Table 6.1   Electrical properties (μ, V_{th} and *SS*) of the *parallel*, *perpendicular* PCDTPT OFETs fabricated on hydrophobic nano-grooved SiO₂ surface, and of *isotropic* PCDTPT OFETs (without nano-grooves) measured in the saturation regime.

	Parallel OFETs			*Perpendicular* OFETs			*Isotropic* OFETs		
	A_v	σ	σ / A_v	A_v	σ	σ / A_v	A_v	σ	σ / A_v
μ [cm²·V⁻¹·s⁻¹]	1.881	0.051	2.7%	0.210	0.008	3.7%	0.501	0.030	6.0%
V_{th} [V]	-5.8	0.6		-5.2	0.7		-3.9	0.3	
SS [V per decade]	0.51	0.17		0.68	0.33		0.36	0.11	

6.3.3 Operational stability of PCDTPT OFETs

Figure 6.9a shows the transfer characteristics of the *parallel*, *perpendicular*, and *isotropic* PCDTPT OFETs at stress times of 0, 5×10^2, 5×10^3, 2.5×10^4 s. The measurement conditions were the same as for pBTTT OFETs and are given in **Section 6.3.1**. The same measurement conditions could be used because in the linear regime, the small negative V_{DS} (= -1 V) does not cause the electron injection. Much larger threshold voltage shift was observed compared to pBTTT OFETs. The initial values of V_{th}^{lin} and μ^{lin} were -12.6 V and 2.30 $cm^2 \cdot V^{-1} \cdot s^{-1}$ for the *parallel* OFET, -12.0 V and 0.269 $cm^2 \cdot V^{-1} \cdot s^{-1}$ for the *perpendicular* OFET, and -11.4 V and 0.720 $cm^2 \cdot V^{-1} \cdot s^{-1}$ for the *isotropic* OFET, respectively. The bias-stress time dependence of V_{th}^{lin} shift ($\Delta V_{th}^{lin} = V_{th}^{lin}(t) - V_{th}^{lin}(0)$) of PCDTPT OFETs (**Figure 6.9b**) was compared to that of pBTTT OFETs (**Figure 6.9c**, which is the data already presented in **Figure 6.5b**). The values of ΔV_{th}^{lin} for the *parallel*, *perpendicular*, and *isotropic* OFETs were -5.5 V, -6.7 V, and -4.9 V, respectively, after total bias stressing of 2.5×10^4 s. Although the absolute values of V_{th}^{lin} shift were noticeably larger for the OFETs with nano-grooves similarly to the pBTTT OFETs, the difference among the fitting results with the stretched exponential function were relatively small as shown in **Figure 6.9b**. The best fit results were: $\tau = 4.1 \times 10^5$ s and $\beta = 0.346$ for the *parallel* OFET, $\tau = 2.0 \times 10^5$ s and $\beta = 0.362$ for the *perpendicular* OFET, and $\tau = 6.8 \times 10^5$ s and $\beta = 0.354$ for the *isotropic* PCDTPT OFET. These results indicate that although the impact of the nano-grooves on the operational stability PCDTPT OFETs is small, the pBTTT OFETs are much more stable against bias stress overall.
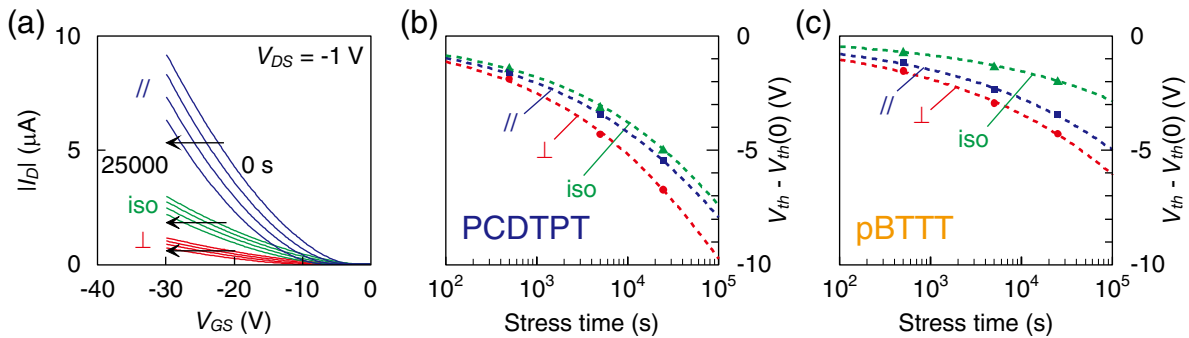
Figure 6.9 (a) Transfer characteristics of the *parallel*, *perpendicular* and *isotropic* (iso) PCDTPT OFETs measured in the linear regime at bias stress times of 0, 5×10^2, 5×10^3, 2.5×10^4 s. (b, c): Bias-stress time dependence of the V_{th}^{lin} shifts (filled symbols) and of the normalized mobility (open symbols) of the (b): PCDTPT and (c): pBTTT-C16 OFETs. The circles, squares and triangles are the data points of *perpendicular*, *parallel* and *isotropic* OFETs, respectively. The broken curves in (b) represent the fitting results of the V_{th}^{lin} shifts with the stretched exponential functions.

6.3.4 Discussion

XRD and AFM measurements of the OSC films were performed to understand the origin of the difference in operational stability of pBTTT and PCDTPT OFETs. Also, the operational stability described in this chapter was compared to the results obtained by other groups.

a) Characterization of the OSC films with XRD and AFM

Figure 6.10a shows the out-of-plane XRD profiles of the spin coated pBTTT-C16 and PCDTPT films in the hydrophobic areas. The data for the films formed using the same conditions as ones explained in **Section**

Figure 6.10 Out-of-plane XRD profiles of the spin-coated (a, b) pBTTT-C16 and PCDTPT films formed from same solutions as the OFETs of this chapter and (c, d): PCDTPT films formed from solutions of various concentrations as indicated in the legend. The measurements were performed in the hydrophobic areas. (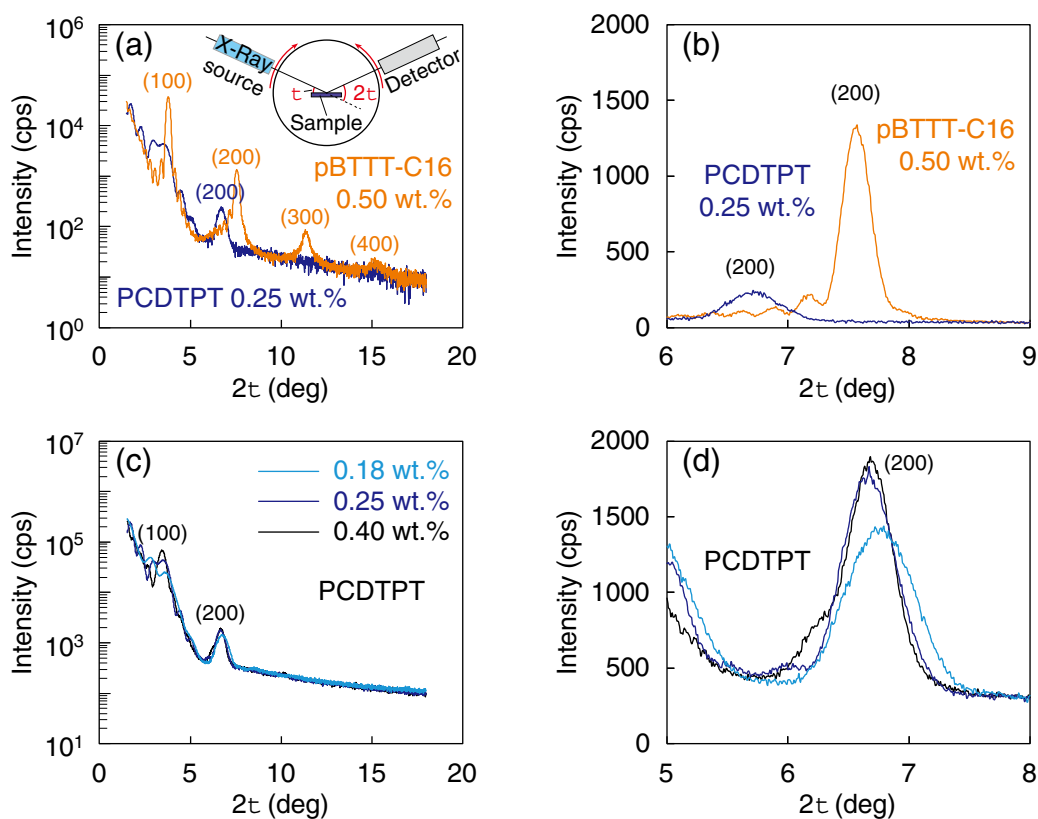b) and (d) are magnified profiles of the (200) Bragg peaks in (a) and (c), respectively. The geometry of the measurement is shown as the inset in (a). The measurement conditions were different for (a, b) and (c, d) as summarized in **Table 6.2**.

5.2.2 (see p.45) and **Section 6.2.2** (see p.59) are plotted; that is, spin coated from 0.5 wt.% solution in *o*-DCB heated in 85°C bath for pBTTT-C16, and from 0.25 wt.% solution in chlorobenzene at RT for PCDTPT. Up to (400) Bragg peaks were visible for pBTTT-C16, corresponding to lamellar spacing (d-spacing) of 2.34 nm. This distance is consistent with the molecular step of terrace-phase pBTTT-C16 and with reported XRD profiles.[6.5],[6.6] Unfortunately, (100) peak for PCDTPT was distorted probably due to interference effect related to the film thickness. From the (200) peak, the d-spacing of PCDTPT was found to be 2.63 nm. The peaks also indicate that the OSCs are indeed aligned predominantly in an edge-on orientation. The magnified profiles around (200) peaks of the pBTTT and PCDTPT films are shown in **Figure 6.10**b. The volume of the crystalline part of the films is proportional to the area of the Bragg's peaks. The peak intensity for the PCDTPT film was much smaller than that of the pBTTT film although the direct comparison could not be performed due to the possible difference in diffraction efficiency for different materials.

The out-of-plane XRD profiles of the PCDTPT films formed from solutions of different concentrations were also obtained and are shown in **Figure 6.10**c. The thickness of the films formed from 0.18 wt.%, 0.25 wt.%, and 0.40 wt.% solutions (referred hereafter as *film A*, *film B*, and *film C*, respectively) measured by AFM were 7.9, 12.9 and 19.6 nm, respectively. The clear (100) Bragg's peak was visible for *film C*. The measurement conditions were changed from those used to obtain data in **Figure 6.10**a in order to improve the signal to noise ratio and are summarized in **Table 6.2**. Interestingly, the intensity of the (200) peak for PCDTPT was almost identical regardless of the film thickness and was only slightly lower for *film A*. These results

indicate that only the bottom layers of PCDTPT film slightly thicker than 8 nm exhibit crystalline structure. The crystallite size (height of the crystalline grains for the out-of-plane measurement) is inversely proportional to the full width at half maximum (FWHM) of the peaks according to the Scherrer's equation:

$$B = \frac{K\lambda}{L\cos\theta},$$ (6.7)

where B is the FWHM of the Bragg's peaks (in radians), λ is the wavelength of the X-Ray beam, L is crystallite size, and θ is the Bragg's angle. K is a constant depending on the shape and orientation of the crystalline grains. If we assume that L for *film A* is limited by and almost equal to the film thickness, from **Equation 6.7** we can estimate L for *film B* and *film C* to be 10.2 and 11.4 nm, respectively. Thus, we can speculate that the film is structured as illustrated in **Figure 6.11**a. The crystalline grains are present in mostly disordered PCDTPT only near the substrate surface. On the other hand, the crystalline grains in the pBTTT film are expected to be present throughout the whole film as illustrated in **Figure 6.11**b because the LC nature of pBTTT results in its high crystallinity.

Table 6.2   Measurement conditions used to obtain data in **Figure 6.10**.

	Figure 6.10a, b	**Figure 6.10**c, d
Scanning speed [deg/min]	0.3	0.3
X-Ray wavelength [Å]	1.5406 (Cu $K\alpha$1) 1.5444 (Cu $K\alpha$2)	1.5406 (Cu $K\alpha$1) 1.5444 (Cu $K\alpha$2)
Incident soller slit aperture angle [deg]	0.5	1.0
Incident slit width [mm]	0.4	0.4
Incident length limiting slit [mm]	2	10
Receiving slit 1	Open	Open
Parallel slit analyzer [deg]	0.114	0.114
Receiving soller slit aperture angle [deg]	None	None
Receiving slit 2	Open	Open
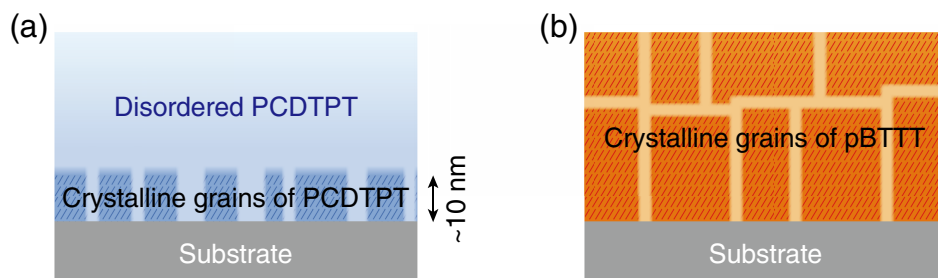
Figure 6.11   Estimated structures of (a): PCDTPT and (b): pBTTT films.

The spread of crystal plane orientations in the films was examined by performing rocking curve measurements in which the detector orientations with respect to the incident X-Ray beam direction are fixed at 2θ corresponding to (200) Bragg peak positions: $2\theta = 7.56°$, 6.757°, 6.674°, and 6.682° for the pBTTT-C16, PCDTPT *film A*, *film B*, and *film C*, respectively (**Figure 6.12**). The sample was tilted in the range of 0.5° (± 0.25°), taking origin of tilt angle ω at the corresponding θ values. The FWHM of a rocking curve positively
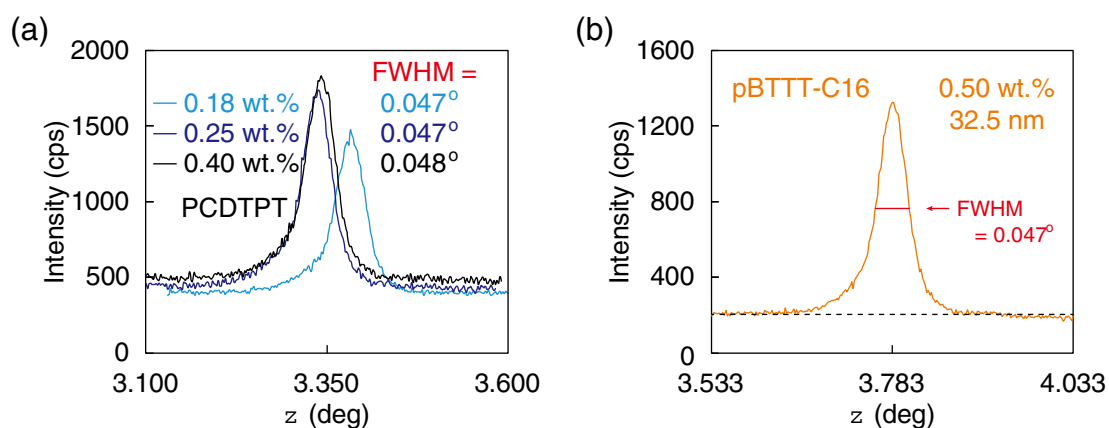
Figure 6.12 Rocking curves taken at 2θ fixed at values corresponding to (200) Bragg peaks for the spin-coated (a) PCDTPT and (b): pBTTT films in the hydrophobic areas.

correlates with the orientation distribution of (200) crystal plane. It is necessary to note that the obtained curves were noticeably asymmetrical. The asymmetry did not depend on the film thickness or material and was probably related to the asymmetry of (200) peaks in **Figure 6.10**. The peaks in **Figure 6.12** showed no noticeable difference in FWHM (= ~0.05°). Although this result shows that the alignment degree of crystalline parts of pBTTT and PCDTPT films is quite high, it could not be compared between the films because the obtained FWHM values were on the verge of resolution of the used apparatus (the FWHM of the rocking curve for single crystal Si was ~0.04°).

The morphology of the *film A*, *film B*, *film C* and the pBTTT film was studied by performing the AFM measurements. The surface of *film A* (**Figure 6.13**a) has clear molecular steps indicating that the crystalline grains cover the whole film thickness. The molecular steps become more obscure in the order of *film B* and *film C* (**Figure 6.13**b and **Figure 6.13**c, respectively) which is explained by the presence of disordered
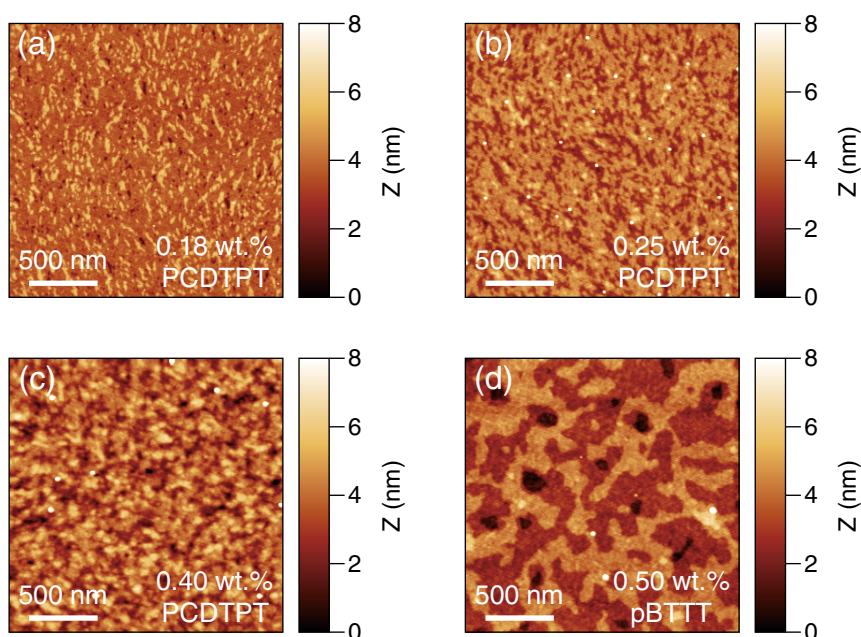

Figure 6.13 AFM images of (a, b, c): PCDTPT films formed by spin-coating from 0.18 wt.%, 0.25wt.%, and 0.40 wt.% solutions, respectively and (d): pBTTT film formed by spin-coating from 0.50 wt.% solution.

68

PCDTPT on top of the crystalline part. For the pBTTT film (**Figure 6.13**d), clear molecular steps and large terrace structures are visible. These results support the estimated structures of the films shown in **Figure 6.11**. From the AFM images we can also see that in contrast to the terrace-phase pBTTT film, the visible structures of the PCDTPT films are very small. Thus, we can speculate that the lateral size of crystalline grains is also smaller for PCDTPT resulting in larger density of crystalline/disordered boundaries. Such boundaries contribute to the trap site formation and may explain the low operational stability of PCDTPT.

b) Comparison of operational stability with other reports

The fitting analysis using **Equation 6.3** is commonly performed on both organic and inorganic transistors. Thus, the estimated τ and β can be compared with those of organic and inorganic FETs reported by other groups. The values of β and τ that were previously reported for polymer-based OFETs[6.7] and a-Si FETs[6.8] are summarized in **Table 6.3** together with the results of this study. We show only β and τ of polymer-based OFETs determined in vacuum, which can be compared with those determined in this study. The trapping time constant τ of the *isotropic* pBTTT-OFET was approximately an order of magnitude larger than those of OFETs with polytriarylamine (PTAA) and poly(3-hexylthiophene-2.5-diyl) (P3HT) active layers formed on hexamethyldisilazane (HMDS)-treated SiO_2 gate dielectrics. Because the V_{th} shift in OFETs is related to residual water,[6.6],[6.9] this operational stability improvement may be attributed to the high water-repellent nature of our ODTS-treated SiO_2 surfaces, whose water contact angle was greater than 110°. Although the τ was lowered by one order of magnitude through the fabrication of nano-grooves, it was still comparable to that of a-Si FETs. The τ was indeed lower by more than one order of magnitude for D-A copolymer PCDTPT OFETs compared to the semicrystalline OSC OFETs. These results indicate that the *intrinsic* operational stability of pBTTT OFETs with a highly hydrophobic nano-grooved SiO_2 gate dielectric surface is equivalent to the operational stability of a-Si FETs and that semicrystalline polymers are still attractive in terms of the operational stability.

Table 6.3   Trapping time constant (τ) and stretching factor (β) at room temperature for polymer-based OFETs evaluated in vacuum and for a-Si FETs.

Semiconductor	Gate-dielectric	τ [s]	β	Atmosphere	Ref.
pBTTT-C16	Nano-grooved ODTS-SiO_2	1×10^7 (//) 9×10^6 ($\perp$)	0.33 (//) 0.29 ($\perp$)	in vac.	this work [6.3]
pBTTT-C16	ODTS-SiO_2	6×10^8	0.23	in vac.	this work [6.3]
PCDTPT	Nano-grooved ODTS-SiO_2	4×10^5 (//) 2×10^5 ($\perp$)	0.35 (//) 0.36 ($\perp$)	in vac.	this work
PCDTPT	ODTS-SiO_2	7×10^5	0.35	in vac.	this work
PTAA	HMDS-SiO_2	4×10^7	0.30	in vac.	[6.7]
P3HT	HMDS-SiO_2	2×10^6	—	in vac.	[6.7]
a-Si	—	1×10^7	0.39	—	[6.8],[6.10]

6.4   Summary

The operational stability of OFETs with active layers of semicrystalline polymer pBTTT-C16 and D-A copolymer PCDTPT was evaluated. Also, the impact of the nano-grooved gate dielectric surface on the operational stability (on-state bias-stress effect) was investigated. The bias-stress effect measurements were performed in vacuum to eliminate the extrinsic instability caused by the atmospheric oxygen and moisture. The hole trapping time constant τ of pBTTT OFETs was reduced from 10^8 to 10^7 s by producing the nano-grooves on the gate dielectric surface. Nevertheless, it was still comparable to that of a-Si FETs. Thus, the pBTTT OFETs with active layers aligned by highly hydrophobic nano-grooved surfaces were found to have high operational stability. Although the carrier mobility of pBTTT OFETs ($\mu_{//}^{pBTTT} = 0.513 \pm 0.018$ cm^2·V^{-1}·s^{-1}) was lower than that of PCDTPT OFETs ($\mu_{//}^{PCDTPT} = 1.88 \pm 0.05$ cm^2·V^{-1}·s^{-1}), the trapping time constant was more than one order of magnitude larger ($\tau_{//}^{pBTTT} = 1 \times 10^7$ s against $\tau_{//}^{PCDTPT} = 4 \times 10^5$ s). This was presumably due to larger density of crystalline/disordered boundaries of PCDTPT near the OSC/gate dielectric interface, which was suggested by the XRD and AFM measurements. Very high operational stability of pBTTT OFETs was achieved considering that 10^7 s is ~4 months. These findings suggest the high potential for highly hydrophobic nano-grooved surfaces as alignment-inducing surfaces that can be incorporated into OFET structures as well as that semicrystalline polymers such as pBTTT are still attractive in terms of operational stability. Our alignment technique using highly hydrophobic nano-grooved surfaces, spin-coating, and pattering of hydrophobic/hydrophilic surface regions should be promising to achieve the high field-effect mobility, small DDV, and high operational stability simultaneously.

References

[6.1] M. Matters, D. M. de Leeuw, P. T. Herwig, and A. R. Brown. "Bias-Stress Induced Instability of Organic Thin Film Transistors." *Synthetic Met.* **1999**, 102, 998.

[6.2] H. Lee, H. H. Choi, D. H. Kim, and K. Cho. "25th Anniversary Article: Microstructure Dependent Bias Stability of Organic Transistors." *Adv. Mater.* **2014**, 26, 1660.

[6.3] K. Bulgarevich, K. Sakamoto, T. Minari, T. Yasuda, K. Miki, and M. Takeuchi. "Polymer-Based Organic Field-Effect Transistors with Active Layers Aligned by Highly Hydrophobic Nanogrooved Surfaces." *Adv. Funct. Mater.* **2019**, 29, 1905365.

[6.4] H. Phan, M. Wang, G. C. Bazan, and T.-Q. Nguyen. "Electrical Instability Induced by Electron Trapping in Low-Bandgap Donor–Acceptor Polymer Field-Effect Transistors." *Adv. Mater.* **2015**, 27, 7004.

[6.5] T. Umeda, S. Tokito, and D. Kumaki. "High-Mobility and Air-Stable Organic Thin-Film Transistors with Highly Ordered Semiconducting Polymer Films." *J. Appl. Phys.* **2007**, 101, 054517.

[6.6] K. Ueji, M. Ohno, J. Takeya, and S. Watanabe. "Correlation Between Coherent Charge Transport and Crystallinity in Doped π-conjugated Polymers." *Appl. Phys. Express.* **2019**, 12, 011004.

[6.7] S. G. J. Mathijssen, M. Cölle, H. Gomes, E. C. P. Smits, B. de Boer, I. McCulloch, P. A. Bobbert, and D. M. de Leeuw. "Dynamics of Threshold Voltage Shifts in Organic and Amorphous Silicon Field-Effect Transistor." *Adv. Mater.* **2007**, 19, 2785.

[6.8] S. C. Deane, R. B. Wehrspohn, M. J. Powell. "Unification of the Time and Temperature Dependence of Dangling-Bond-Defect Creation and Removal in Amorphous-Silicon Thin-Film Transistors." *Phys. Rev. B* **1998**, 58, 12625.

[6.9] A. Sharma, S. G. J. Mathijssen, E. C. P. Smits, M. Kemerink, D. M. de Leeuw, and P. A. Bobbert. "Proton Migration Mechanism for Operational Instabilities in Organic Field-Effect Transistors." *Phys. Rev. B* **2010**, 82, 075322.

[6.10] This value is calculated using $\tau = \nu_0^{-1}\exp(E_a/k_B T)$ with $E_a = 0.975$ eV, $\nu_0 = 10^{10}$ Hz, and $T = 300$ K, where E_a and k_B are the activation energy and Boltzmann constant, respectively.

Chapter 7 Operational stability enhancement by perfluoropolymer coating

In this chapter, the considerable enhancement of operational stability for the pBTTT-C16 OFETs by coating the gate dielectric surface with an amorphous perfluoropolymer[7.1] is reported. A serious problem in depositing the active layer on the highly hydrophobic perfluoropolymer-coated gate dielectric by solution processes was solved by producing suitable hydrophobic/hydrophilic patterns. A simple photo-patterning method was developed for CYTOP™ (CTL-809M, AGC) which is terminated with amidosilyl functional groups. This method is composed of a self-limited thinning process of CYTOP layers, exposure to VUV light through a photomask, and development. The stability against bias-stress of the OFETs with CYTOP-coated gate dielectric was significantly higher than that of OFETs with ODTS-treated gate dielectrics while the initial characteristics were almost the same. Here, the novel photo-patterning process for CYTOP, the device properties of the OFETs with CYTOP-coated gate dielectric and their bias-stress effect is discussed.

7.1   Effects of gate dielectric modifications on operational stability

The alkyl SAMs are commonly used as a gate dielectric modification in OFETs to induce edge-on orientation of OSC molecules and to reduce adsorption of water at the interface between OSC and the gate dielectric. The water repellent nature of alkyl SAMs is beneficial for improvement of the operational stability of OFETs. The values of the trapping time constant and the stretching factor obtained in **Chapter 6** ($\tau = 1.0 \times 10^7$ s and $\beta = 0.334$ for the *parallel* OFET)[7.2] were consistent with (and slightly higher than) those of previously reported polymer-based OFETs with SiO_2 gate dielectrics covered with SAMs under vacuum conditions. These trapping time constants are comparable to those of *a*-Si FETs, meaning that the operational stability of these OFETs in air can be potentially improved up to that of *a*-Si FETs by blocking atmospheric oxygen and moisture. However, the crystalline nature of the alkyl SAMs means the inevitable formation of grain boundaries which may contribute to trap site formation. In fact, the hydrocarbon-based self-assembled monolayers were reported not to be the optimal surfaces for charge trap reduction.[7.3] Thus, although promising results were obtained, there is still a potential for operational stability improvement.

A hydroxyl-free amorphous fluoropolymer, poly(perfluorobutenylvinylether), CYTOP™ (**Figure 7.1**) is a promising candidate for gate dielectric coating materials with successful reports of improved operational stability of OFETs.[7.4] CYTOP is an excellent hydroxyl-free insulator and is highly hydro- and lyophobic (water contact angle of ~115°). It is also a good homeotropic surface alignment layer for smectic LCs. However, the high lyophobicity of CYTOP causes the dewetting of common organic solvents which prevents stable OSC film formation by solution processes.[7.5],[7.6] Thus, for the BG structures in which the active layers are deposited on the gate dielectrics, the deposition process of active layers was restricted to thermal evaporation in most
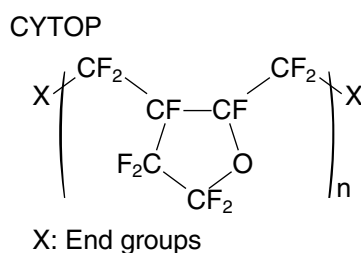

Figure 7.1   Chemical structure of CYTOP

cases.[7.4],[7.7],[7.8] To utilize solution processing techniques except for push coating,[7.9] it is necessary to adopt TG structures, in which the CYTOP gate dielectrics are placed onto the active layers.[7.6],[7.10],[7.11] Since CYTOP has excellent chemical stability and dissolves in fluorinated solvents that are orthogonal to most organic semiconductor materials, the active layers underneath are not damaged in most cases.[7.5],[7.6],[7.10] However, in our preliminary experiments on TG-type OFETs with CYTOP gate dielectric and an active layer of pBTTT-C16, the deterioration of the current on/off ratio was observed. This result suggests that the fluorinated solvent of CYTOP affects the active layer more or less. In addition, BG-type OFETs offer a relatively simple fabrication process and are desirable in some applications. Thus, the development of a simple solution coating method to fabricate BG-type OFETs with CYTOP-coated gate dielectrics would considerably expand the application area of OFETs.

7.2   Realization of spin-coating onto CYTOP

Similar to ODTS-treated SiO_2 surfaces, the formation of pBTTT-C16 films on uniformly CYTOP-coated SiO_2 surface failed due to dewetting of OSC solution because the hydrophobicity (lyophobicity) of CYTOP is even higher than that of ODTS. This coating issue can be overcome by producing hydrophobic/hydrophilic patterns as was reported in **Chapter 3**. In contrast to ODTS which can easily be removed by VUV-light exposure, CYTOP-coated SiO_2 surfaces cannot be hydrophilized sufficiently by VUV light-exposure alone, because a residue produced by VUV-light exposure remains. To obtain sufficient hydrophilicity, the residue must be removed by additional processing and/or reduced by utilizing a thin CYTOP film. Therefore, a method to produce hydrophobic/hydrophilic patterns with sufficient contrast on CYTOP-coated SiO_2 surfaces without lowering the smoothness of CYTOP surfaces was established first.

The residue produced by VUV-light exposure can be reduced by utilizing a very thin CYTOP coating layer. Thus, the first step to fabricate BG-type OFETs with CYTOP-coated gate dielectrics was to form thin and smooth CYTOP films on SiO_2 surfaces. **Figure 7.2**a-**Figure 7.2**e are the AFM images of the CYTOP (CTL-809M) films obtained by spin-coating of solution with various concentrations. The solutions of CYTOP
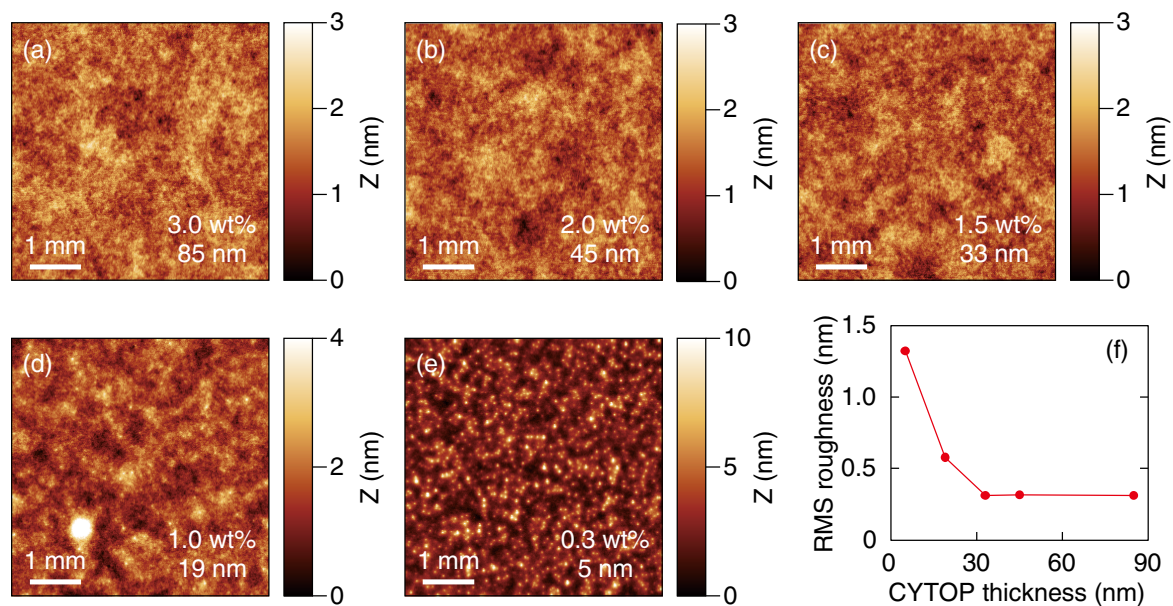

Figure 7.2   (a-e): AFM images of CYTOP films formed by spin-coating with different concentrations of solutions. (f): relationship between the root mean square (rms) surface roughness and the film thickness.

were prepared by diluting the original solution with a fluorinated solvent (CT-solv.180™, AGC). The films were obtained by spin-coating at 3000 rpm for 60 s, and then drying on a hot plate in nitrogen atmosphere in the following three steps: at 50°C for 10 min, at 80°C for 10 min, and at 180°C for 1 h. For the spin coated CYTOP films, spin-coating from solution of relatively high concentration can produce smooth films with small root mean square (rms) surface roughness as can be seen in **Figure 7.2**a. The thin films can be obtained by lowering the concentration, but the roughness becomes high. **Figure 7.2**f indicate that smooth films can be obtained only for films thicker than 30 nm. Thus, the very thin CYTOP layers formed directly by spin-coating could not be used.

In this study, a self-limited thinning process of CYTOP layers, which can be realized by using CYTOP terminated with amidosilyl functional groups (CTL-809M shown in **Figure 7.3**a) was developed. A relatively thick (85 nm-thick) CYTOP layer was first formed on a hydrophilized SiO_2 surface by spin-coating and then baking at 180°C. During baking, the CYTOP polymers with amidosilyl functional groups that contacted the SiO_2 surface were chemically anchored to it. Unreacted CYTOP polymers were removed by subsequent sonication in CT-solv.180. **Figure 7.3**a is the sonication time dependence of the CYTOP layer thickness measured with a stylus profiler, clearly indicating that the film thickness rapidly decreases down to ~5 nm and then become constant. By performing sonication for 60 min, ~5 nm-thick smooth CYTOP coating layer with a rms roughness of 0.24 nm was obtained and exhibited a water contact angle of 116°. The AFM image is shown in **Figure 7.3**b. The CYTOP thickness was measured by removing the CYTOP film with a W needle and measuring the profile with a stylus type step profiler (Kosaka ET200). The results of such measurements are presented in **Figure 7.3**c and **Figure 7.3**d. The thinned CYTOP coating layer is composed of
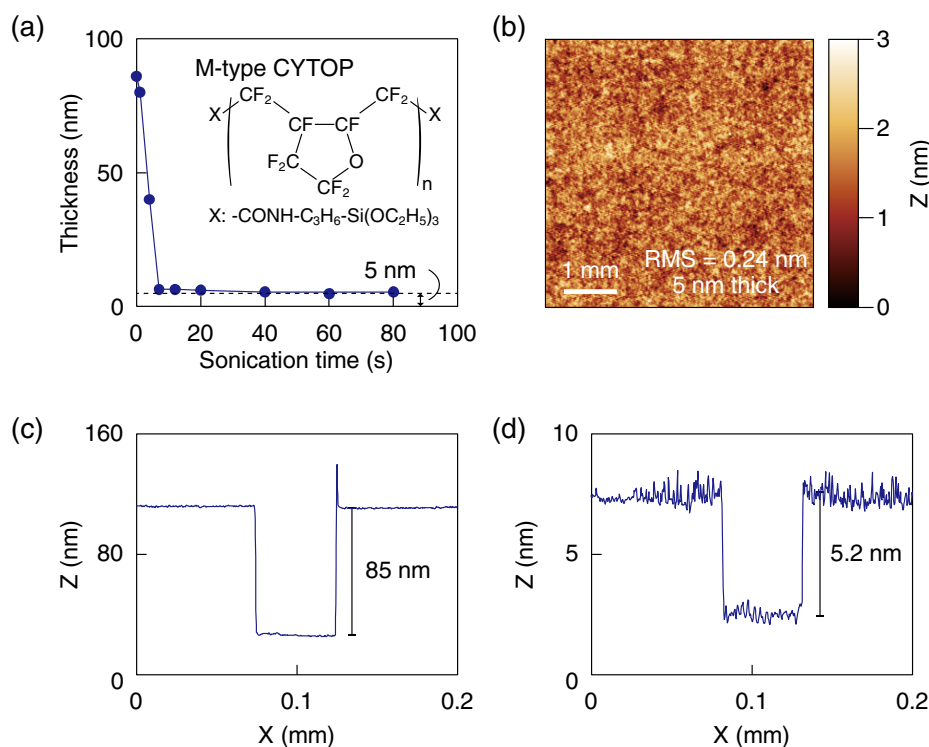

Figure 7.3 (a): Sonication (in CT-solv.180) time dependence of the CYTOP film thickness. The chemical structure of M-type CYTOP (CTL-809M) is shown as an inset. (b): AFM image of the CYTOP film after the self-limited thinning process. (c, d): Profiles of the scratches produced by a W needle on the CYTOP film before (c) and after (d) self-limited thinning process.
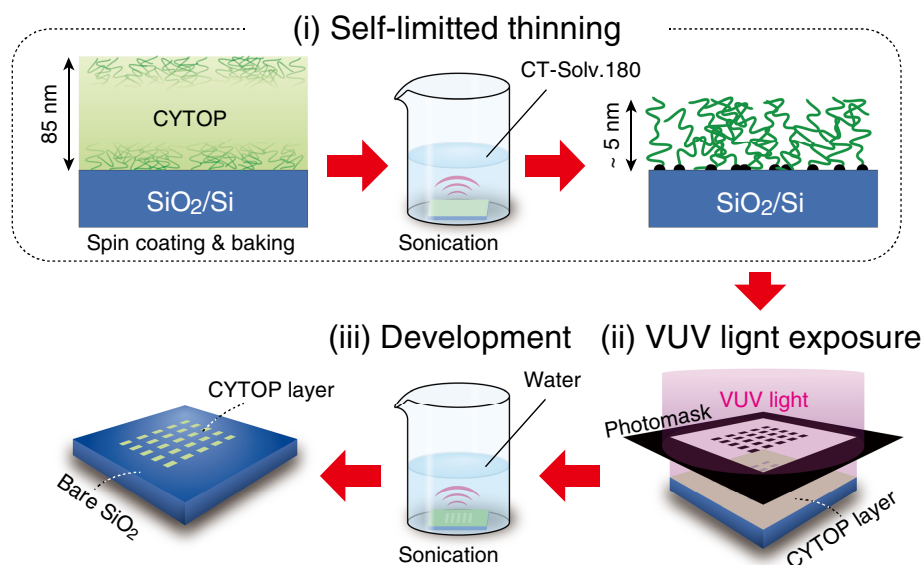
Figure 7.4   Method to produce hydrophobic/hydrophilic patterns with sufficient contrast on CYTOP-coated SiO$_2$/n$^+$-Si substrates.

perfluoropolymers covalently bonded to the SiO$_2$ surface, providing strongly adherent thin polymeric layers with high uniformity, like "polymer brush". This coating layers are expected to have high resistance against delamination or cracking during development following VUV-light exposure and during spin-coating of organic semiconductor solutions.

Now, the patterning of the thinned CYTOP layer could be performed. The pattering method established in this study is shown in **Figure 7.4**. The hydrophobic/hydrophilic patterns of CYTOP-coated SiO$_2$ surfaces are formed by the following three steps: (i) formation of ~5 nm-thick CYTOP coating layers using a self-limited thinning process, which was already described, (ii) exposure of the thinned CYTOP coating layers to VUV light (wavelength 172 nm) through a photomask, and (iii) development by sonication in deionized water (removal of a residue produced by the VUV-light exposure).

A hydrophobic/hydrophilic pattern had to be redesigned from the pattern used in **Chapter 3** to enable film formation on CYTOP whose hydrophobicity is much higher than that of ODTS. To produce a hydrophobic/hydrophilic pattern, the CYTOP-coated SiO$_2$ surface was exposed to VUV light for 30 min
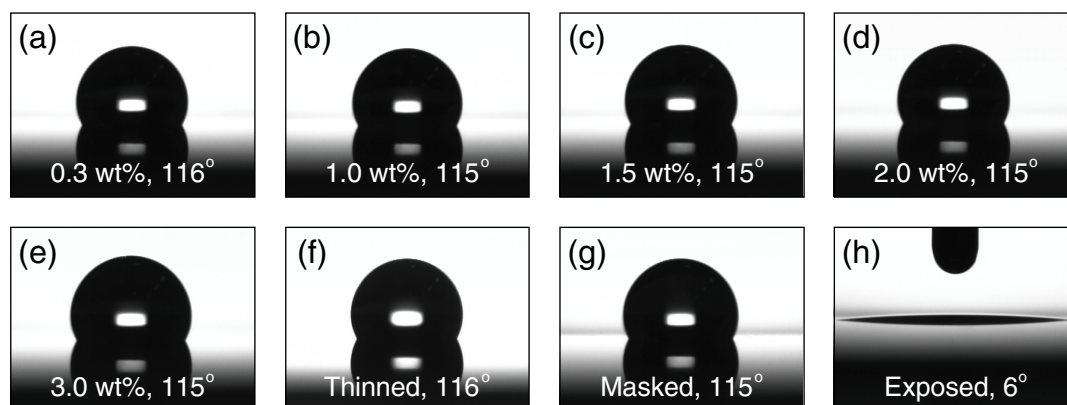

Figure 7.5   Contact angle measurements of water on CYTOP film formed by spin-coating from (a): 0.3, (b): 1.0, (c): 1.5, (d): 2.0, (e): 3.0 wt.% solutions and (f): 3.0 wt.% solution followed by self-limited thinning process.

through a photomask. Then, the residue produced by VUV-light exposure was removed by sonication in deionized water for 10 min three times. The exposed area exhibited a water contact angle of 6°. Thus, the sufficient contrast between hydrophobic and hydrophilic areas was successfully obtained.

Figure 7.5a-**Figure 7.5**e show the images of the water droplets on the CYTOP film formed by spin-coating from solution of various concentrations after baking. Highly hydrophobic films showing water contact angles of ~116° were obtained regardless of the solution concentration (film thickness). **Figure 7.5**f is the image of the water droplet on the thinned (~5 nm) CYTOP film obtained by the self-limited method described above. We can see that the hydrophobicity is not degraded by the self-limited thinning. Finally, **Figure 7.5**g and **Figure 7.5**h show the water droplets on the substrate covered with thinned CYTOP film after the VUV-light exposure and sonication in water in the masked and exposed areas, respectively. High contrast between hydrophobic (masked) and hydrophilic (exposed) areas can be seen.

Successful achievement of sufficient contrast between hydrophobic and hydrophilic areas enabled the film formation of pBTTT-C16 by spin-coating. The pBTTT-C16 was formed on the CYTOP-coated SiO_2/n^+-Si surfaces using the conditions described in **Chapter 5**. The effective surface pattern that enables pBTTT-C16 film formation on CYTOP is shown in **Figure 7.6**a. Prior to spin-coating, the substrate and a glass pipet were heated on hot plates at 110°C and 120°C, respectively, and the 0.5 wt.% solution of pBTTT-C16 in *o*-DCB was heated to 85°C using a hot bath. The heated substrate was fixed on a Teflon sample holder of a spin-coater (Active ACT-220D II), immediately covered with hot pBTTT-C16 solution using the heated pipet, and then it was rotated at 1000 rpm for 180 s. Next, the spin-coated film was dried on a hot plate at 90°C for 10 min. This spin-coating process was carried out in air. Finally, the film was annealed at 150°C for 15 min in a nitrogen atmosphere to obtain a terrace-phase pBTTT-C16 film. The resulting film is shown in **Figure 7.6**b.
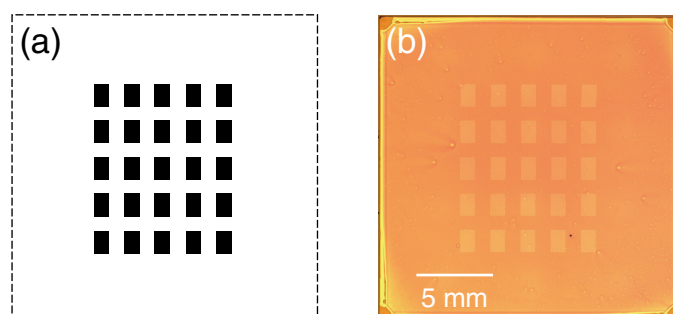

Figure 7.6   (a): Effective photomask pattern for pBTTT-C16 film formation on CYTOP and (b): pBTTT-C16 film spin-coated onto CYTOP-coated SiO_2 surface.

7.3 Results and discussion

7.3.1 pBTTT-C16 film characterization

The characterization was performed after the fabrication and all the electrical measurements of the OFET array.

a) AFM images

Figure 7.7a and **Figure 7.7**b are AFM images ($2 \times 2 \ \mu m^2$) of the pBTTT-C16 active layer of the OFET array fabricated by spin-coating on ODTS-treated and on the thinned CYTOP-coated SiO$_2$ surface, respectively. Although the terrace structure with molecular steps of ~2.2 nm was observed, steps for the CYTOP-coated surface were slightly more obscure than those for the ODTS-treated SiO$_2$ surface. This is probably attributed to the difference in the surface morphology between the CYTOP-coated and ODTS-treated SiO$_2$ surfaces. As shown in **Figure 7.7**c, the ODTS-treated surface is extremely flat except for some particles (probably polymerized particles). Meanwhile, as shown in **Figure 7.7**d, the CYTOP-coated layer has 1 nm-height and ~50 nm-lateral scale structures which come from the amorphous nature of CYTOP polymers with a distributed molecular weight.
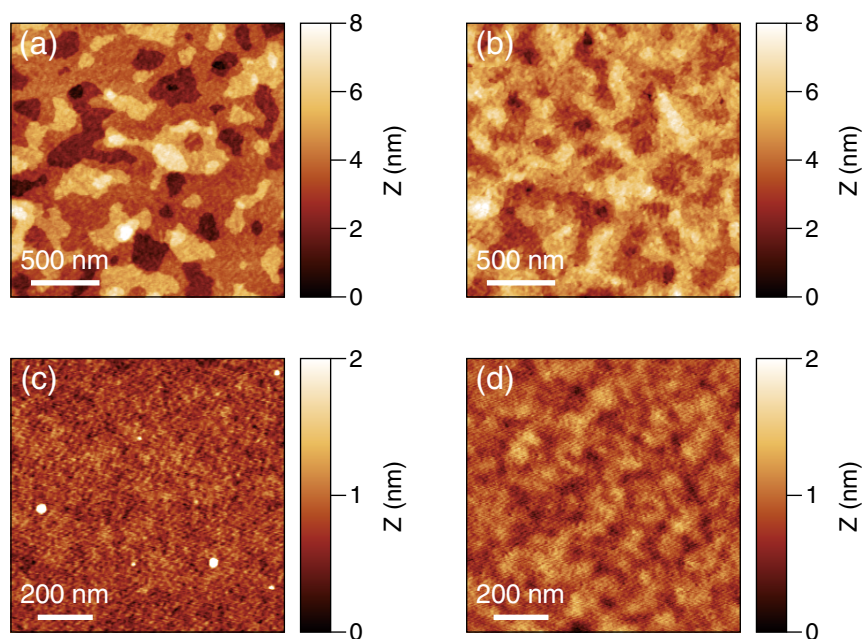
Figure 7.7   AFM images of pBTTT-C16 active layer formed on (a): ODTS-treated and (b): thinned CYTOP-coated SiO$_2$ surfaces. (c) and (d) are AFM images of the ODTS-treated and thinned CYTOP-coated SiO$_2$ surfaces, respectively.

b) Film thickness

The thickness measurement of the pBTTT-C16 film spin coated on CYTOP-coated SiO$_2$ surface was performed along 15 lines (30 positions) which are indicated in **Figure 7.8**a. **Figure 7.8**b shows the line profile along the blue segment in **Figure 7.8**a. The dents are the lines on which pBTTT-C16 is removed by a probe for OFET isolation. The film thickness was found to be 26 ± 1 nm.

Figure 7.8 (a): Optical microscope image of the pBTTT-C16 OFET array fabricated on the thinned CYTOP-coated SiO$_2$ surface. The pBTTT film thickness measurement was performed along the white lines. The extracted profiles along the segments highlighted in blue and black are shown in (b) and (c), respectively.

7.3.2 Initial OFET device properties

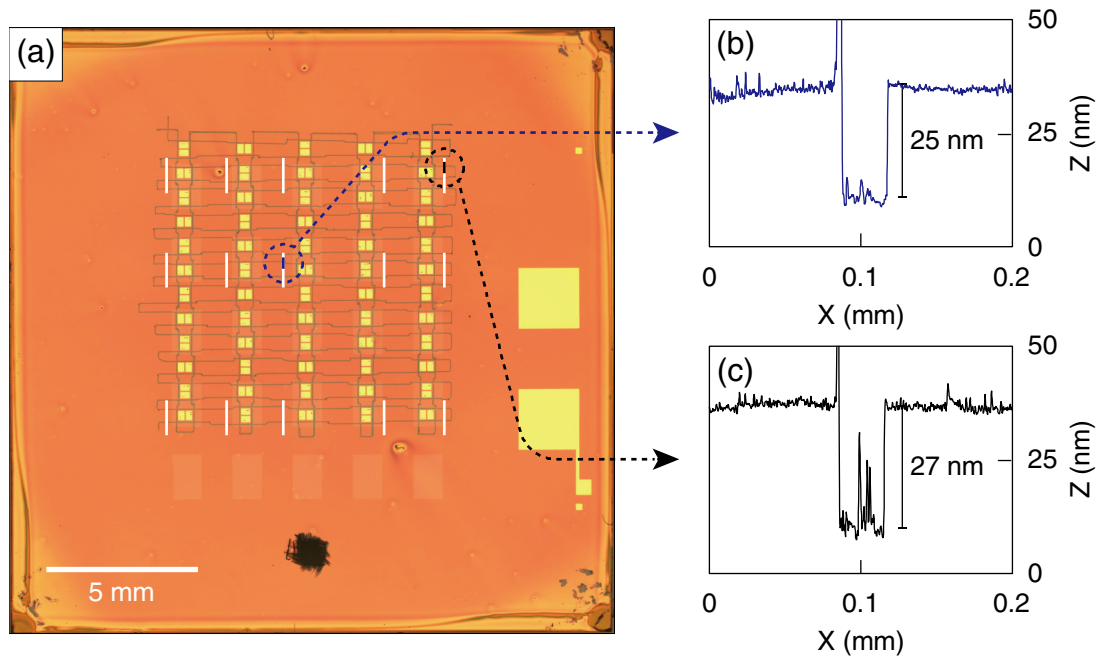To check the spatial uniformity of the pBTTT-C16 active layer and the CYTOP coating layer from the viewpoint of device performance, a BG/TC-type OFET array was fabricated. The S/D electrodes were deposited on the terrace-phase pBTTT-C16 film formed on the CYTOP-coated SiO$_2$/n$^+$-Si(100) substrate by sequential thermal evaporation of MoO$_x$ (25 nm-thick) and Au (63 nm-thick) through a shadow mask in vacuum (base pressure $< 5 \times 10^{-4}$ Pa). The S/D electrodes were placed in the hydrophobic surface regions. The shadow mask produced an array of 40 OFETs with L / W of 50 / 300 μm over an area of ~1 cm^2. The channel directions of neighboring OFETs were orthogonal to each other although no difference in their device performance was expected. The output and transfer characteristics of all OFETs were measured in saturation
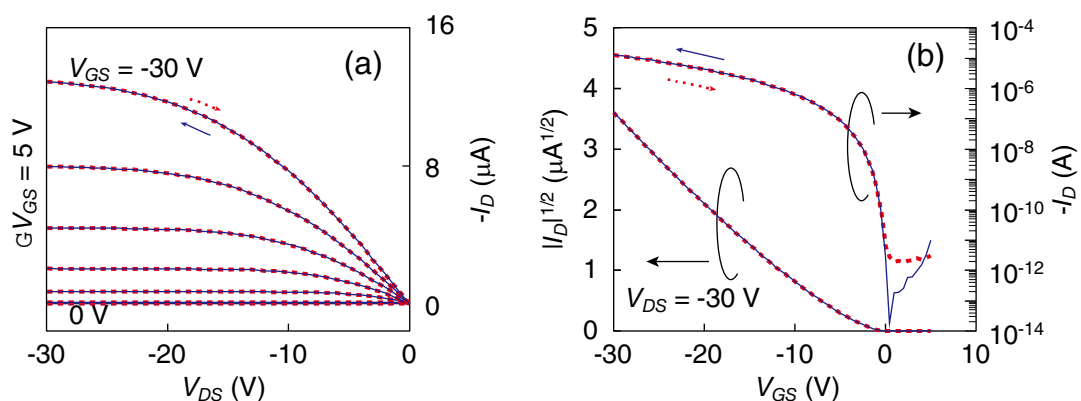

Figure 7.9 Typical (a): output and (b): transfer characteristics of a pBTTT-C16 OFET fabricated on thinned CYTOP-coated SiO$_2$ surface.

regime in vacuum. After being loaded into a vacuum probe station, the device substrate was annealed at 150°C for 15 min in vacuum to remove residual oxygen and moisture from the OFETs. The typical output and transfer characteristics of the CYTOP-OFETs are shown in **Figure 7.9**a and **Figure 7.9**b, respectively. In both characteristics, good *p*-channel transistor behavior was observed with almost no I_D hysteresis between the forward (negative direction) and reverse (positive direction) voltage sweeps. The maximum current on/off ratio was greater than 10^7. The gate capacitance per unit area C_i for the CYTOP-coated dielectric was 28.3 nF/cm^2.
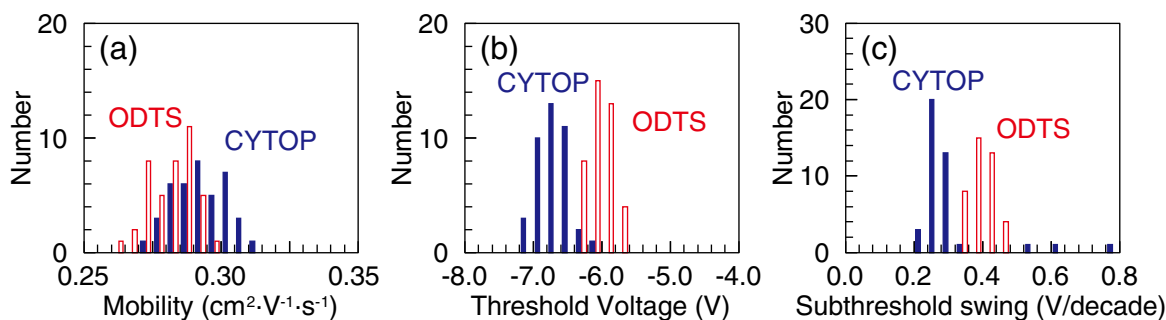

Figure 7.10　Histograms of a) field-effect hole mobility, b) threshold voltage, and c) subthreshold swing of pBTTT-C16 OFETs fabricated on thinned CYTOP-coated and ODTS-treated SiO$_2$ surface (60 each). The filled and open bars show the results for the CYTOP-coated and ODTS-treated OFETs, respectively. The bin widths of the histograms are a) 0.005 cm^2·V^{-1}·s^{-1}, b) 0.2 V, and c) 0.04 V per decade.

From the transfer characteristics shown in **Figure 7.9**b, we obtained: $\mu = 0.289$ cm^2·V^{-1}·s^{-1} and $V_{th} = -7.0$ V. The *SS* was determined to be 0.27 V per decade from the partial transfer characteristics that were separately measured by varying V_{GS} from 5 V to -5 V at intervals of 0.05 V. **Figure 7.10**a, **Figure 7.10**b, and **Figure 7.10**c show the histograms of μ, V_{th}, and *SS*, respectively. Their average values (A_v), standard deviations (σ), and relative standard deviations (σ / A_v) are listed in **Table 7.1**. The μ was 0.291 ± 0.009 cm^2·V^{-1}·s^{-1}, and its relative variation (σ / A_v) was less than 4 %. In addition to μ, the DDVs of V_{th} (= -6.7 ± 0.2 V) and *SS* (= 0.30 ± 0.11 V per decade), were also small. These small DDVs indicate the high spatial uniformity of the pBTTT active layers as well as of the underlying CYTOP coating layers.

Table 7.1　Electrical properties (μ, V_{th} and *SS*) of pBTTT-C16 OFETs fabricated on CYTOP-coated and ODTS-treated SiO$_2$ surfaces. The measurements were performed in the saturation regime.

	CYTOP-OFETs			ODTS-OFETs		
	A_v	σ	σ / A_v	A_v	σ	σ / A_v
μ [cm^2·V^{-1}·s^{-1}]	0.292	0.010	3.3%	0.281	0.008	2.8%
V_{th} [V]	-6.7	0.2		-6.0	0.2	
SS [V per decade]	0.30	0.11		0.45	0.07	

As the hydrophobicity of CYTOP is higher than that of ODTS, a considerable improvement in the OFET properties was expected by treating the gate dielectric surfaces with CYTOP instead of ODTS. However, the initial electrical properties of the CYTOP-OFETs were very close to those of the ODTS-OFETs described in **Chapter 5** as "*isotropic* OFETs".[7.2] These OFETs were fabricated on the pattered ODTS-treated
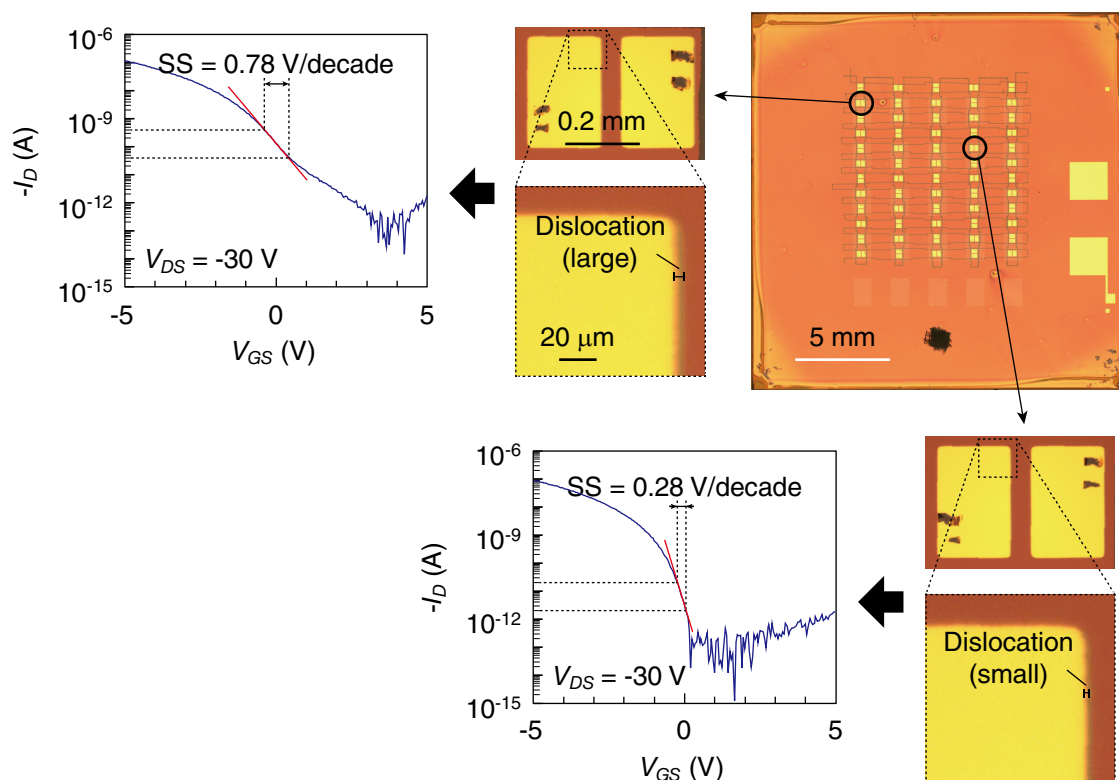
Figure 7.11 Optical microscope image of the pBTTT-C16 OFET array fabricated on the thinned CYTOP-coated SiO₂ surface (top-right) with the magnified images of two representative sets of electrodes. The partial transfer characteristics and *SS* values of the two OFETs is also provided.

SiO$_2$/n$^+$-Si(100) substrates with the same fabrication procedure, except for the patterning of ODTS. For comparison, those data are plotted by open bars in **Figure 7.10**a, **Figure 7.10**b, and **Figure 7.10**c and are presented in **Table 7.1**. The relatively large difference was observed only in *SS*; the average value of *SS* was 0.30 V per decade for the CYTOP-OFETs and 0.45 V per decade for the ODTS-OFETs. Because the *SS* is related to the trap density in the active layer and at the interface between the active layer and the gate dielectric, this result may indicate that the CYTOP-OFETs have a higher quality of the interface and the active layer near the interface than the ODTS-OFETs. However, at present we suspect that the *SS* may be degraded by the dislocation in overlapping of the MoO$_x$ and Au layers of the bilayer S/D electrodes. In depositing the electrodes, a 20 μm-thick nickel shadow mask was used and was magnetically fixed on the active layer surface. The dislocation might be caused by the distortion of the shadow mask and/or by unexpected slight slide of the shadow mask during thermal evaporation due to its residual magnetization. The former leads to the degradation of *SS* of specific devices, and the latter results in the degradation of all OFETs on the same substrate. All four CYTOP-OFETs with *SS*'s exceeding 0.3 V/decade were in the upper left corner. Indeed, larger dislocation of the electrode was observed for OFETs in the upper left corner compared to the others as shown in **Figure 7.11**. This degradation in *SS* in these devices is probably related to the local distortion of the shadow mask. Since we have not been able to completely eliminate this dislocation to date, origin of the difference in *SS* between the CYTOP- and ODTS-OFETs will not be discussed in detail here.

Before proceeding, it is worth referring to the extremely small I_D hysteresis of the CYTOP-OFETs. In the scale of **Figure 7.9**a, no hysteresis in I_D can be seen. Similarly, no I_D hysteresis can be recognized in the transfer characteristics of the ODTS-OFETs, which were shown in **Figure 5.12**d (see p.52). To demonstrate

the smaller I_D hysteresis of the CYTOP-OFETs, the magnified transfer curves of the CYTOP- and ODTS-OFETs are shown in **Figure 7.12**. The smaller I_D hysteresis of the CYTOP-OFET suggests the higher resistivity against gate-bias stress.
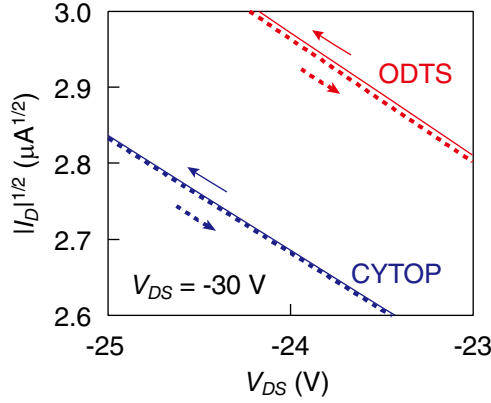

Figure 7.12 Magnified transfer characteristics of CYTOP- and ODTS-OFETs. The transfer curves were taken from **Figure 7.9**a and **Figure 5.12**d (*isotropic* OFET), respectively.

7.3.3 Operational stability

The measurements of bias-stress effects were also performed under vacuum condition to remove the instability induced by atmospheric oxygen and moisture. Since this instability is extrinsic and can be removed or considerably reduced by passivation, the bias-stress effect originating from extrinsic and intrinsic factors must be examined separately. Here, we focused only on the intrinsic bias-stress effect. The bias-stress effect of CYTOP-OFETs against an on-state bias was evaluated similarly to the procedure described in the previous chapter: by repeating cycles of constant prolonged gate-bias application and transfer characteristic measurement in linear regime ($|V_{DS}| \ll |V_{GS}|$). In this measurement, $V_{GS} = -30$ V and $V_{DS} = -1$ V were applied to OFETs as an on-state bias up to 2.0×10^5 s, and the temperature of the OFETs was controlled at 30°C. This bias stress condition was the same as that for the ODTS-OFETs, except for the total bias stress time and the temperature of OFETs: 2.5×10^4 s and room temperature (RT) (no temperature control), respectively, for ODTS-OFETs. Since the ΔV_{th}^{lin} of CYTOP-OFETs was an order of magnitude smaller than that of
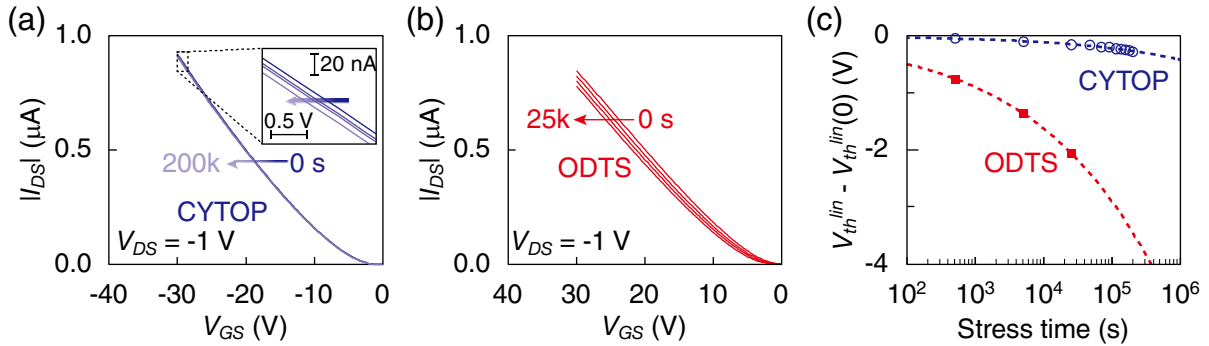
Figure 7.13 Transfer characteristics of a) CYTOP- and b) ODTS-OFETs that were measured in the linear regime at different bias-stress times: 0, 5×10^3, 2.5×10^4, and 2×10^5 s for the CYTOP-OFET and 0, 5×10^2, 5×10^3, and 2.5×10^4 s for the ODTS-OFET. c) Bias-stress time dependence of the V_{th}^{lin} shifts for the CYTOP-OFET (open circles) and the ODTS-OFET (filled squares). The broken curves in c) represent the fitting results of the V_{th}^{lin} shifts with the stretched exponential functions.

81

ODTS-OFETs as can be seen below, slight variation in μ caused by fluctuation of RT has a non-negligible influence on the evaluation of ΔV_{th}^{lin}. Thus, we controlled the device temperature and extended the total bias stress time for CYTOP-OFETs. Although the temperature was controlled, the procedure of measuring the I_D decay over bias-stress time explained in **Section 6.1** (see p.59) could not be used because the variation in μ could not be eliminated completely and **Equation 6.4** was not applicable. Thus, the stability of CYTOP-OFETs was evaluated only using the same measurement procedure as the ODTS-OFETs. The bias stress effect for the ODTS-OFETs was already discussed in **Chapter 6**.[7.2] For comparison, these data will be presented together with the data for CYTOP-OFETs.

  Figure 7.13a shows the transfer characteristics of the CYTOP-OFET measured at total stress times of 0, 5×10^3, 2.5×10^4 and 2×10^5 s, with only the forward sweep characteristics plotted. As the shift of the threshold voltage in linear regime (V_{th}^{lin}) was very small even after applying the on-state bias for 2×10^5 s, the four transfer curves are almost overlapped. The inset shows the enlarged transfer curves around -30 V, indicating the transfer curve parallelly shifts in the negative voltage direction with increasing bias stress time. This parallel shift with respect to the initial transfer curve correspond to the V_{th}^{lin} shift ($\Delta V_{th}^{lin} = V_{th}^{lin}$ (t) - V_{th}^{lin} (0)). The ΔV_{th}^{lin} at 5×10^3, 2.5×10^4 and 2×10^5 s were -0.11, -0.16 and -0.28 V, respectively. **Figure 7.13**b shows the transfer characteristics of the ODTS-OFET measured at total stress times of 0, 5×10^2, 5×10^3, 2.5×10^4 s. Although the operational stability of the ODTS-OFET is comparable to that of a-Si field-effect transistors, we see that the ΔV_{th} is much larger than that of the CYTOP-OFET at the same bias stress time: for instance, ΔV_{th}^{lin} = -2.0 V at 2.5×10^4 s for the ODTS-OFET. **Figure 7.13**c shows the bias stress time dependence of ΔV_{th}^{lin} for both the CYTOP- and ODTS-OFETs. The much smaller variation in ΔV_{th}^{lin} was observed for the CYTOP-OFET than for the ODTS-OFET, indicating that the operational stability can be considerably improved by changing the coating material of gate dielectric surfaces from ODTS to CYTOP.

  To quantitatively discuss the operational stability, the bias stress time dependence of ΔV_{th}^{lin} was fitted with a stretched exponential function. The broken curves in **Figure 7.13**c show the best fit results: $\tau = 1 \times 10^{12}$ s and $\beta = 0.28$ for the CYTOP-OFET, and $\tau = 3 \times 10^8$ s and $\beta = 0.26$ for the ODTS-OFET. From these fitting results, we found that the operational stability of the CYTOP-OFET was more than three orders of magnitude higher than that of the ODTS-OFET. These β and τ values can be compared with those of a-Si FETs: $\beta = 0.39$ and $\tau = 2 \times 10^6$ s.[7.12],[7.13] The comparison of these τ values suggests that OFETs that far exceed the operational stability of a-Si FETs can be potentially realized by using CYTOP-coated gate dielectrics and pBTTT-C16 as an active layer material, with the aid of passivation technique. Therefore, the simple spin-coating method established in this study is a promising technique to realize the extremely high operational stability of OFETs.[7.1]

7.3.4 Discussion

  We succeeded in achieving unprecedented operational stability of OFETs by combining pBTTT-C16 active layers and CYTOP-coated gate dielectrics in a BG/TC device structure. The trapping time constant of the CYTOP-OFETs was at least 3 orders of magnitudes larger than that of the ODTS-OFETs. However, unlike expectations, the initial electrical properties of both the OFETs were almost the same, as seen in **Figure 7.10**. From the AFM images of the pBTTT layers on the ODTS-coated and CYTOP-treated SiO$_2$ surfaces presented in **Figure 7.7**c and **Figure 7.7**d, respectively, we can see that the terrace-phase structures characterizing the pBTTT layers on the CYTOP-coated surface were slightly more obscure than those on the ODTS-treated SiO$_2$ surface. This is probably due to the difference in the surface morphology between the CYTOP-coated and ODTS-treated SiO$_2$ surfaces. The relatively long scale surface undulation of the CYTOP-coated layer shown in **Figure 7.7**e may slightly reduce the charge carrier mobility. As a result, the initial electrical properties may

not have improved by replacing the coating materials from ODTS to CYTOP.

Next, the possible origins of the extremely high operational stability of CYTOP-OFETs is discussed. We believe that the extremely high operational stability is due to the preferred microstructure of the pBTTT/CYTOP interface. The difference in the microstructure might come from that in the crystallinity of the coating layers. From the infrared (IR) absorption spectrum shown in **Figure 7.14**, we found that the absorption maxima for the methylene symmetric and antisymmetric C-H stretching vibrations were located between wavenumbers that characterize the liquid-like (disordered) and crystalline layers. However, since the disordered surface of ODTS with a low molecular density leads to the lowering of water contact angles,[7.14] the water contact angle of > 110° suggests that at least the topmost parts have a crystalline order uniformly in the lateral direction. According to the report by Steinrück et al.,[7.15] the upper parts of the alkyl chains of ODTS self-assembled monolayers (SAMs) formed on SiO_2/Si(100) by standard solution procedures are vertically aligned in all trans-form configuration and hexagonally packed in lateral direction. On the other hand, the bottom parts (~11 CH_2 units) near the SiO_2 surface are disordered due to mismatch between a cross-sectional diameter of all-*trans* alkyl chains (4.9 Å)[7.14],[7.16] and lateral cross-linking Si-O-Si bond length (< 3.2 Å).[7.17] Although the preparation procedure was different, the structure of the ODTS SAMs prepared by vapor treatment in this study is believed to be similar. Therefore, the upper parts of the ODTS SAMs prepared in this study are considered to have crystalline order of all-trans alkyl chains. The mismatch mentioned above was also reported to limit the lateral crystal domain size to about 6 nm, suggesting that domain boundaries should be present at a very high surface density on the ODTS-treated surfaces. These domain boundaries may contribute to trap site formation. In contrast to ODTS, the CYTOP layer anchored to the gate dielectric is amorphous. This amorphous nature prevents the formation of such trap sites at the active layer/gate dielectric interface. Therefore, the trap density at the interface and/or in the active layer is expected to be lower for CYTOP-OFETs, resulting in higher operational stability.

In addition, the preferred microstructure of the pBTTT/CYTOP interface might arise from the fact that the CYTOP films work as more stable homeotropic (vertical) alignment-inducing layers for smectic liquid crystals than long alkyl chain silane SAMs.[7.18] pBTTT-C16 is a liquid crystalline polymer showing a smectic phase at a high temperature. The self-organization of individual polymer in the liquid crystalline phase was used to improve the microstructure of the active layers in the fabrication process of OFETs. Therefore, one can imagine that the trap density related to the microstructure of active layer should be lower for the CYTOP-OFETs, resulting in higher bias-stress stability. We believe that both the amorphous nature and better homeotropic alignment capability of the CYTOP layers contribute to the extremely high operational stability.
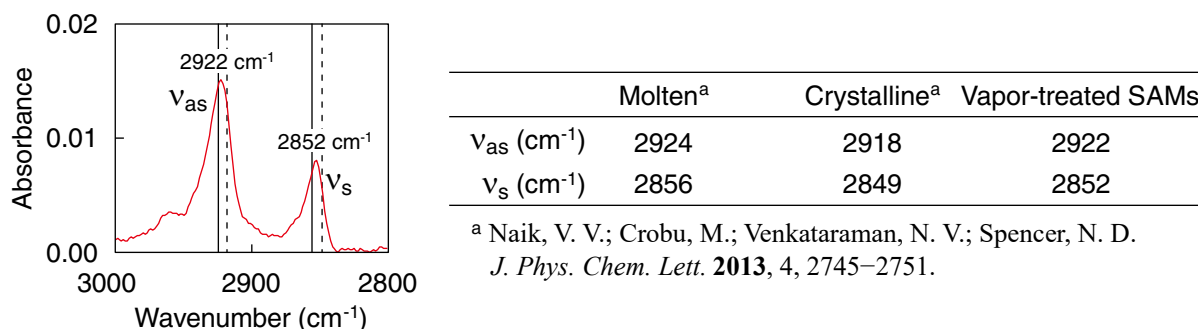

	Molten[a]	Crystalline[a]	Vapor-treated SAMs
ν_{as} (cm^{-1})	2924	2918	2922
ν_s (cm^{-1})	2856	2849	2852

[a] Naik, V. V.; Crobu, M.; Venkataraman, N. V.; Spencer, N. D. *J. Phys. Chem. Lett.* **2013**, 4, 2745−2751.

Figure 7.14 IR absorption spectrum of the ODTS-SAM prepared by vapor treatment used in this study. The adsorption maxima for molten and crystalline alkanes are shown by the solid and broken vertical lines, respectively.

7.4　Summary

We have reported extremely high operational stability of BG/TC-type OFETs with CYTOP-coated gate dielectrics. To fabricate such OFETs, we first developed a simple spin-coating method of pBTTT-C16 on CYTOP-coated gate dielectric surfaces, because the highly hydrophobic (lyophobic) nature of CYTOP prevents thin film formation of pBTTT-C16 by solution processing. This coating problem was solved by patterning the CYTOP coating layer with a suitable design, which allowed organic thin film formation by spin-coating. The patterning of the CYTOP-coated layer was a key process, which was developed in this study. The pattering process was composed of a self-limited thinning process of the CYTOP coating layer, exposure to VUV light through a photomask, and development by sonication in deionized water. After spin-coating of pBTTT-C16 followed by annealing at 150°C, BG/TC-type OFET arrays were fabricated by depositing S/D electrodes in the unexposed areas. Very small DDVs of not only the field-effect mobility but also the threshold voltage and subthreshold swing were observed for the CYTOP-OFET array, indicating high spatial uniformity of the CYTOP coating layers and pBTTT-C16 active layers. Under vacuum condition, the unprecedented bias-stress stability was observed for CYTOP-OFETs. The trapping time constant τ was the order of 10^{12} s, while that of ODTS-OFETs was the order of 10^8 s, where the latter is comparable to or surpasses that of a-Si FETs. The extremely large trapping time constant suggests that OFETs that far exceed the operational stability of a-Si FETs can be potentially realized with the aid of passivation technique. We believe that the amorphous nature of CYTOP polymers and the good alignment capability of CYTOP layers for smectic liquid crystals play an important role in achieving the unpreceded high bias-stress stability. The simple spin-coating method established in this study is a promising technique to realize the extremely high operational stability of the OFETs.

References

[7.1] K. Bulgarevich, K. Sakamoto, T. Yasuda, T. Minari, and M. Takeuchi. "Operational Stability Enhancement of Polymeric Organic Field-Effect Transistors by Amorphous Perfluoropolymers Chemically Anchored to Gate Dielectric Surfaces." Submitted to *Adv. Electron. Mater.*

[7.2] K. Bulgarevich, K. Sakamoto, T. Minari, T. Yasuda, K. Miki, and M. Takeuchi. "Polymer-Based Organic Field-Effect Transistors with Active Layers Aligned by Highly Hydrophobic Nanogrooved Surfaces." *Adv. Funct. Mater.* **2019**, 29, 1905365.

[7.3] K. Suemori, S. Uemura, M. Yoshida, S. Hoshino, N. Takada, T. Kodzasa, and T. Kamata. "Threshold Voltage Stability of Organic Field-Effect Transistors for Various Chemical Species in the Insulator Surface." *Appl. Phys. Lett.* **2007**, 91, 192112.

[7.4] T. Umeda, D. Kumaki, and S. Tokito. "High Air Stability of Threshold Voltage on Gate Bias Stress in Pentacene TFTs with a Hydroxyl-Free and Amorphous Fluoropolymer as Gate Insulators." *Org. Electron.* **2008**, 9, 545.

[7.5] J. Kim, S. H. Kim, T. K. An, S. Park, and C. E. Park. "Highly Stable Fluorine-Rich Polymer Treated Dielectric Surface for the Preparation of Solution-Processed Organic Field-Effect Transistors." *J. Mater. Chem. C* **2013**, 1, 1272.

[7.6] R. Hamilton, J. Smith, S. Ogier, M. Heeney, J. E. Anthony, I. McCulloch, J. Veres, D. D. C. Bradley, and T. D. Anthopoulos. "High-Performance Polymer-Small Molecule Blend Organic Transistors." *Adv. Mater.* **2009**, 21, 1166.

[7.7] S. H. Kim, S. Nam, J. Jang, K. Hong, C. Yang, D. S. Chung, C. E. Park, and W.-S. Choi. "Effect of the Hydrophobicity and Thickness of Polymer Gate Dielectrics on the Hysteresis Behavior of Pentacene-Based Field-Effect Transistors." *J. Appl. Phys.* **2009**, 105, 104509.

[7.8] M. P. Walser, W. L. Kalb, T. Mathis, T. J. Brenner, and B. Batlogg. "Stable Complementary Inverters with Organic Field-Effect Transistors on Cytop Fluoropolymer Gate Dielectric." *Appl. Phys. Lett.* **2009**, 94, 053303.

[7.9] M. Ikawa, T. Yamada, H. Matsui, H. Minemawari, J. Tsutsumi, Y. Horii, M. Chikamatsu, R. Azumi, R. Kumai, and T. Hasegawa. "Simple Push Coating of Polymer Thin-Film Transistors." *Nat. Commun.* **2012**, 3, 1176.

[7.10] D. K. Hwang, C. Fuentes-Hernandez, J. Kim, W. J. Potscavage Jr., S.-J. Kim, and B. Kippelen "Top-Gate Organic Field-Effect Transistors with High Environmental and Operational Stability." *Adv. Mater.* **2011**, 23, 1293.

[7.11] W.-T. Park, G. Kim, C. Yang, C. Liu, and Y.-Y. Noh. "Effect of Donor Molecular Structure and Gate Dielectric on Charge-Transporting Characteristics for Isoindigo-Based Donor-Acceptor Conjugated Polymers." *Adv. Funct. Mater.* **2016**, 26, 4695.

[7.12] S. C. Deane, R. B. Wehrspohn, M. J. Powell. "Unification of the Time and Temperature Dependence of Dangling-Bond-Defect Creation and Removal in Amorphous-Silicon Thin-Film Transistors." *Phys. Rev. B* **1998**, 58, 12625.

[7.13] This value is calculated using $\tau = \nu_0^{-1}\exp(E_a/k_BT)$ with $E_a =0.975$ eV, $\nu_0 = 10^{10}$ Hz, and $T = 300$ K, where E_a and k_B are the activation energy and Boltzmann constant, respectively.

[7.14] V. V. Naik, M. Crobu, N. V. Venkataraman, and N. D. Spencer. "Multiple Transmission-Reflection IR Spectroscopy Shows that Surface Hydroxyls Play Only a Minor Role in Alkylsilane Monolayer Formation on Silica." *J. Phys. Chem. Lett.* **2013**, 4, 2745.

[7.15] H.-G. Steinrück, J. Will, A. Magerl, and B. M. Ocko. "Structure of n-alkyltrichlorosilane Monolayers on Si(100)/SiO$_2$." *Langmuir* **2015**, 31, 11774.

[7.16] K. Okuyama, Y. Soboi, N. Iijima, K. Hirabayashi, T. Kunitake, and T. Kajiyama. "Molecular and Crystal Structure of the Lipid-Model Amphiphile, Dioctadecyldimethylammonium Bromide Monohydrate." *Bull. Chem. Sco. Jpn.* **1988**, 61, 1485.

[7.17] D. R. Lide. *CRC Handbook of Chemistry and Physics*, 85th ed.; CRC Press: New York, **2004**. Chapter 9.

[7.18] S. M. Jeong, J. K. Kim, Y. Shimbo, F. Araoka, S. Dhara, N. Y. Ha, K. Ishikawa, and H. Takezoe.

"Perfluoropolymer Surface for Shock-Free Homeotropic Alignment of Smectic Liquid Crystals." *Adv. Mater.* **2010**, 22, 34.

Chapter 8   Summary

8.1   Conclusion

In this thesis study, we have successfully developed a coating method for film formation on highly hydrophobic surfaces previously considered unusable as substrates. By surrounding the hydrophobic areas with hydrophilic ones under appropriate design using VUV exposure through a photomask, the continuous OSC film formation was enabled on the entire substrate surface. The useful pattern for flow-coating was a lyophobic/lyophilic line-and-space pattern connected to the top lyophilic rectangular region. The film formation mechanism was understood by performing a simple surface energy calculation. The film formation on the lyophobic surface areas was possible because of the pinning of the contact line to the film growth front with the help of the own formed (forming) film. Thus, this coating method was named '*self-assisted flow-coating*' (SAF-coating). The resulting film was found to be show anisotropy in pBTTT backbone direction (backbones were found to be aligned on average parallel to the flow-coating direction) and was very uniform in thickness (22.6 ± 1.8 nm). The useful lyophobic/lyophilic pattern for film formation on the lyophilic areas by spin-coating was also designed.

In order to measure the electrical properties of the self-assisted flow-coated film, and to confirm its spatial uniformity, the BG/TC type OFET array (60 OFETs) using pBTTT-C16 film as the active layer was fabricated. The pBTTT-C16 film was annealed at an LC temperature to form a terrace phase and increase the carrier mobility. Since the flow-coating is a unidirectional process, anisotropy in charge transport was expected. To evaluate that, the fabricated OFET array consisted of OFETs whose channel current direction was parallel or *perpendicular* with respect to the coating direction (30 OFETs each). The device properties of each OFET were measured and the DDV and the anisotropy were evaluated. The pBTTT-C16 film was also examined with a POM, AFM, and polarized Raman spectroscopy. POM observations and polarized Raman measurements confirmed the in-plane anisotropy of the flow-coated pBTTT-C16 film (the polymer backbones aligned parallel to the coating direction on average). From the AFM images, the formation of terrace-phase pBTTT-C16 by the LC temperature annealing was confirmed. The OFET measurements showed that the DDV of the OFET array was extremely small. The average field-effect hole mobility of the *parallel* and *perpendicular* OFET sets were 0.273 and 0.221 cm$^2 \cdot$V$^{-1} \cdot$s^{-1}, respectively and the DDV of mobility was less than 3% for each set. The DDV of other device properties (drain current, threshold voltage, and subthreshold swing) was also very small which resulted in nearly identical transfer characteristics of all the OFETs within each OFET set. Thus, the relatively high carrier mobility and very small DDV were achieved by the use of the SAF-coating method.

The carrier mobility of pBTTT-C16 OFETs was further improved by aligning pBTTT-C16 active layers aligned by a highly hydrophobic nano-grooved gate dielectric surface, which exhibited a water contact angle of greater than 110°. An array composed of *parallel* and *perpendicular* OFETs of 30 each was fabricated to evaluate the in-plane anisotropy and spatial uniformity in the charge transport of the aligned pBTTT-C16 active layer. The carrier mobilities of the *parallel* OFETs with respect to the nano-grooves direction was 0.513 $\pm$ 0.018 cm$^2 \cdot$V$^{-1} \cdot$s^{-1} resulting in alignment-induced mobility enhancement ($\mu_{//} / \mu_{iso}$) of a factor of ~2. The DDV was also suppressed and was only slightly greater (< 4%) than that (< 3%) of the *isotropic* OFETs without nano-grooves. To our knowledge, this study is the first to report the formation of an array of OFETs with terrace-phase pBTTT active layers exhibiting alignment-induced field-effect mobility enhancement and small DDV.

It was confirmed that the operational stability of the pBTTT-C16 OFETs exhibiting alignment-induced mobility enhancement was high. The bias-stress effect measurements were performed in vacuum to eliminate the extrinsic instability caused by the atmospheric oxygen and moisture. Although the hole trapping time

constant τ was reduced from 10^8 to 10^7 s by producing the nano-grooves on the gate dielectric surface, it was still comparable to that of a-Si FETs. Although the carrier mobility of pBTTT OFETs was lower than that of PCDTPT OFETs, the trapping time constant was more than one order of magnitude larger. The operational stability of pBTTT OFETs was very high considering that 10^7 s is 4 months indicating that the semicrystalline polymers are still attractive in terms of the operational stability. These findings suggest the high potential for highly hydrophobic nano-grooved surfaces as alignment-inducing surfaces that can be incorporated into OFET structures. Our alignment technique using highly hydrophobic nano-grooved surfaces, spin-coating, and pattering of hydrophobic/hydrophilic surface regions were shown to be promising to achieve the high field-effect mobility, small DDV, and high operational stability simultaneously.

The operational stability of BG/TC-type OFETs was drastically improved by using CYTOP-coated gate dielectrics instead of ODTS-treated ones. To fabricate such OFETs, a simple spin-coating method of pBTTT-C16 on highly hydrophobic CYTOP-coated gate dielectric surfaces was developed. The patterning of the CYTOP-coated layer was a key process, which was developed in this study. The pattering process was composed of a self-limited thinning process of the CYTOP coating layer, exposure to VUV light through a photomask, and development by sonication in deionized water. After spin-coating of pBTTT-C16 followed by annealing at 150°C, BG/TC-type OFET arrays were fabricated by depositing S/D electrodes in the unexposed areas. Very small DDV of not only the field-effect mobility but also for the threshold voltage and subthreshold swing were observed for the CYTOP-OFET array, indicating high spatial uniformity of the CYTOP coating layers and pBTTT-C16 active layers. Under vacuum condition, the unprecedented bias-stress stability was observed for CYTOP-OFETs. The trapping time constant τ was the order of 10^{12} s, which is more than 3 orders of magnitude larger than that of ODTS-OFETs. The extremely large trapping time constant suggests that OFETs that far exceed the operational stability of a-Si FETs can be potentially realized with the aid of passivation technique. We believe that the amorphous nature of CYTOP polymers and the good alignment capability of CYTOP layers for smectic liquid crystals play an important role in achieving the unpreceded high bias-stress stability. The simple spin-coating method established in this study is a promising technique to realize the extremely high operational stability of OFETs.

The film formation and alignment techniques developed in this thesis enable fabrication of high performance OFETs exhibiting high carrier mobility, extremely small DDV and unprecedented operational stability and are expected to be applicable to fabrication processes for commercial OFETs.

8.2   Future works

For the future perspective, the carrier mobility achieved in this thesis was not among the highest values reported. However, as already said, it was comparable to amorphous silicon FETs which is considered to be enough for applications in displays and sensors. More importantly, the DDV was extremely small. Also, the unprecedented high operational stability was achieved which are all important for practical applications. However, the relevant challenges still remain. First, the alignment-induced mobility enhancement was not achieved simultaneously with operational stability improvement. This is because the combination of nano-grooves and the CYTOP-coated surfaces is nontrivial. Also, the higher degree of carrier mobility enhancement is expected if the directional self-assisted coating method is combined with nano-grooves alignment layer. From our preliminary experiments, it was found that at least 1.2 times improvement is possible. Finally, for practical applications, these coating and alignment methods should be applied to the flexible substrates such as polyethylene terephthalate (PET), polylactide (PLA) and others.

Acknowledgements

Achievements

List of publications

[1] K. Sakamoto, J. Ueno, <u>K. Bulgarevich</u>, and K. Miki. "Anisotropic Charge Transport and Contact Resistance of 6,13-bis(triisopropylsilylethynyl) Pentacene Field-Effect Transistors Fabricated by a Modified Flow-Coating Method." *Appl. Phys. Lett*. **2012**, 100, 123301.

[2] K. Sakamoto, <u>K. Bulgarevich</u>, and K. Miki. "Small Device-to-Device Variation of 6,13-bis(triisopropylsilylethynyl) Pentacene Field-Effect Transistor Arrays Fabricated by a Flow-Coating Method." *Jpn. J. Appl. Phys.* **2014**, 53, 02BE01.

[3] <u>K. Bulgarevich</u>, K. Sakamoto, T. Minari, T. Yasuda, and K. Miki. "Spatially Uniform Thin-Film Formation of Polymeric Organic Semiconductors on Lyophobic Gate Insulator Surfaces by Self-Assisted Flow-Coating." *ACS Appl. Mater. Interfaces* **2017**, 9, 6237.

[4] <u>K. Bulgarevich</u>, K. Sakamoto, T. Minari, T. Yasuda, K. Miki, and M. Takeuchi. "Polymer-Based Organic Field-Effect Transistors with Active Layers Aligned by Highly Hydrophobic Nanogrooved Surfaces." *Adv. Funct. Mater.* **2019**, 29, 1905365.

[5] <u>K. Bulgarevich</u>, K. Sakamoto, T. Yasuda, T. Minari, and M. Takeuchi. "Operational Stability Enhancement of Polymeric Organic Field-Effect Transistors by Amorphous Perfluoropolymers Chemically Anchored to Gate Dielectric Surfaces." Submitted to *Adv. Electron. Mater.*

Presentations at international conferences

[1] ○K. Sakamoto, <u>K. Bulgarevich</u>, and K. Miki. "6,13-bis(triisopropylsilylethynyl) Pentacene Field-Effect Transistors Fabricated by a Flow-Coating Method." NIMS Conference **2013** (Tsukuba International Congress Center, Ibaraki, Japan) [Oral].

[2] ○<u>K. Bulgarevich</u>, K. Sakamoto, T. Minari, T. Yasuda, and K. Miki. "Polymer-Based Organic Filed-Effect Transistor Arrays Fabricated on Highly Hydrophobic Gate Insulator Surfaces by Flow-Coating." *12th International Conference on Nano-Molecular Electronics* **2016** (Kobe International Conference Center, Hyogo, Japan), S4-O-1 [Oral].

[3] ○<u>K. Bulgarevich</u>, K. Sakamoto, T. Minari, T. Yasuda, K. Miki, and M. Takeuchi. "Alignment-Induced Hole Mobility Enhancement pf pBTTT Organic Field-Effect Transistors by Hydrophobic Nano-Grooved Gate Dielectric Surfaces." *10th International Conference on Molecular Electronics & BioElectronics* **2019** (Nara Kasugano International Forum, Nara, Japan), CO-06 [Oral].

Presentations at domestic conferences in Japan

[1] ○<u>K. Bulgarevich</u>, K. Sakamoto, T. Minari, and K. Miki. "Device-to-Device Variation of pBTTT-C16 Field-Effect Transistor Arrays." *76th Japan Society of Applied Physics Autumn Meeting* **2015** (Nagoya Congress Center, Aichi, Japan), 13p-PA4-20 [Poster].

[2] ○<u>K. Bulgarevich</u>, K. Sakamoto, T. Minari, T. Yasuda, and K. Miki. "Spatial Uniformity of Charge Transport of Flow-Coated pBTTT-C16 Films." *77th Japan Society of Applied Physics Autumn Meeting* **2016** (TOKI MESSE, Niigata, Japan), 16a-B5-12 [Oral].

[3] ○<u>K. Bulgarevich</u>, K. Sakamoto, T. Minari, T. Yasuda, and K. Miki. "Very Small Device-to-Device Variation of pBTTT-C16 Field-Effect Transistor Arrays Fabricated by Flow-Coating." *Tsukuba Global Science Week* **2016** (Tsukuba International Congress Center, Ibaraki, Japan), P-41 [Poster].

[4] ○<u>K. Bulgarevich</u>, K. Sakamoto, T. Minari, and K. Miki. "Formation of Polymeric Organic Semiconductor Films on Lyophobic Gate Insulator Surfaces by Self-Assisted Flow-Coating." *64th Japan Society of Applied Physics Spring Meeting* **2017** (PACIFICO YOKOHAMA, Kanagawa, Japan), 15a-P8-10 [Poster].

[5] ○K. Bulgarevich, K. Sakamoto, T. Minari, T. Yasuda, K. Miki, and M. Takeuchi. "Very High Electrical Stability of Bottom-Gate/Top-Contact Type Polymer-Based Organic Field-Effect Transistors with Perfluoropolymer-Coated Gate Dielectrics." *79th Japan Society of Applied Physics Autumn Meeting* **2018** (Nagoya Congress Center, Aichi, Japan), 19p-145-4 [Oral].

[6] ○K. Bulgarevich, K. Sakamoto, T. Minari, T. Yasuda, K. Miki, and M. Takeuchi. "Alignment-Induced Mobility Enhancement and Small Device-to-Device Variation of Polymer-Based Organic Field-Effect Transistors with Highly Hydrophobic Nano-Grooved Gate Dielectric Surfaces." *80th Japan Society of Applied Physics Autumn Meeting* **2019** (Hokkaido University Sapporo Campus, Hokkaido, Japan), 21a-B32-1 [Oral].

Patents

[1] K. Sakamoto and K. Bulgarevich. "Method for Producing Large Area Domain Organic Semiconductor Crystal Film and Large Area Domain Organic Semiconductor Crystal Film." **2017**, JP6229924B2 [Granted].

Awards

[1] Tsukuba Global Science Week, Student Poster Session on Materials Research, Best Poster Award (**2016**).

[2] University of Tsukuba, Graduate School of Pure and Applied Sciences Dean Award (**2017**).